

## **INFORMATION TO USERS**

**This manuscript has been reproduced from the microfilm master. UMI films the text directly from the original or copy submitted. Thus, some thesis and dissertation copies are in typewriter face, while others may be from any type of computer printer.**

**The quality of this reproduction is dependent upon the quality of the copy submitted. Broken or indistinct print, colored or poor quality illustrations and photographs, print bleedthrough, substandard margins, and improper alignment can adversely affect reproduction.**

**In the unlikely event that the author did not send UMI a complete manuscript and there are missing pages, these will be noted. Also, if unauthorized copyright material had to be removed, a note will indicate the deletion.**

**Oversize materials (e.g., maps, drawings, charts) are reproduced by sectioning the original, beginning at the upper left-hand corner and continuing from left to right in equal sections with small overlaps.**

**Photographs included in the original manuscript have been reproduced xerographically in this copy. Higher quality 6" x 9" black and white photographic prints are available for any photographs or illustrations appearing in this copy for an additional charge. Contact UMI directly to order.**

**Bell & Howell Information and Learning  
300 North Zeeb Road, Ann Arbor, MI 48106-1346 USA  
800-521-0600**

**UMI<sup>®</sup>**



# Elliptic flow in Au+Au collisions at 11.5 A·GeV/c

by

Kirill Filimonov

A thesis submitted  
to the Faculty of Graduate Studies and Research  
in partial fulfillment of the requirements  
of the degree of

Doctor of Philosophy  
in Physics

Department of Physics  
McGill University, Montréal, Canada.  
©Kirill Filimonov, December 1998



**National Library  
of Canada**

**Acquisitions and  
Bibliographic Services**

**395 Wellington Street  
Ottawa ON K1A 0N4  
Canada**

**Bibliothèque nationale  
du Canada**

**Acquisitions et  
services bibliographiques**

**395, rue Wellington  
Ottawa ON K1A 0N4  
Canada**

*Your file* *Votre référence*

*Our file* *Notre référence*

**The author has granted a non-exclusive licence allowing the National Library of Canada to reproduce, loan, distribute or sell copies of this thesis in microform, paper or electronic formats.**

**The author retains ownership of the copyright in this thesis. Neither the thesis nor substantial extracts from it may be printed or otherwise reproduced without the author's permission.**

**L'auteur a accordé une licence non exclusive permettant à la Bibliothèque nationale du Canada de reproduire, prêter, distribuer ou vendre des copies de cette thèse sous la forme de microfiche/film, de reproduction sur papier ou sur format électronique.**

**L'auteur conserve la propriété du droit d'auteur qui protège cette thèse. Ni la thèse ni des extraits substantiels de celle-ci ne doivent être imprimés ou autrement reproduits sans son autorisation.**

**0-612-50159-0**

**Canada**



To my loving wife and daughter...



# Abstract

The azimuthal distributions of charged particles produced in Au+Au collisions at 11.5 A· GeV/c have been analyzed relative to the reaction plane orientation using the E877 experimental setup at the AGS. Details of the calibration procedures, data reduction and analysis methods are presented. With the event-by-event reconstruction of the reaction plane, a Fourier expansion is used to describe the anisotropy in particle distribution. Directed and elliptic flows are quantified by the dipole and quadrupole Fourier coefficients. A method allowing the decoupling of these two effects is introduced. Elliptic flow signals of protons, deuterons,  $\pi^+$ ,  $\pi^-$ ,  $K^+$ ,  $K^-$  have been studied as a function of particle rapidity and transverse momentum for different centralities of the collision. Transition from in-plane to out-of-plane flow as a function of particle rapidity is observed for protons and deuterons. The dependence of elliptic flow on rapidity is suggested to be a good probe for the study of the transient pressure in the collision. The first and second order azimuthal anisotropies of charged pions and kaons have been measured. A weak in-plane elliptic flow of charged pions is detected for the first time at the AGS. The experimental results have been compared with the predictions of the RQMD event generator run in cascade and mean field modes.



# Résumé

Les distributions angulaires des particules chargées par rapport au plan de réaction ont été analysées pour des collisions Au+Au à 11.5 A·GeV/c par l'expérience E877 à l'AGS. Les détails de la calibration, de la réduction et de l'analyse des données sont présentés. Une série de Fourier a été utilisée pour décrire l'anisotropie de la distribution angulaire par rapport au plan de réaction. Les flots elliptiques et dirigés ont été quantifiés en utilisant les coefficients quadrupolaires et dipolaires de la série. La méthode qui a permis le découplage de ces deux effets est aussi présentée. Le flot elliptique des protons, deutons,  $\pi^+$ ,  $\pi^-$ ,  $K^+$ ,  $K^-$  a été étudié en fonction du moment transverse pour différentes centralités de la réaction et pour différentes rapidités des particules. Une transition du flot des protons et des deutons en fonction de la rapidité a été observée. La dépendance du flot elliptique sur la rapidité est suggérée comme une bonne méthode d'analyse de la pression nucléaire transitoire. L'influence de l'expansion radiale sur le flot elliptique des protons a été étudiée. Les premier et deuxième moments des distributions angulaires de pions et de kaons sont mesurés. Un faible flot elliptique des pions chargés dans le plan de la réaction a été détecté pour la première fois à l'AGS. Les résultats expérimentaux sont comparés aux prédictions du modèle RQMD dans le mode "cascade" et aussi dans le mode où l'on tient compte de l'effet du champ nucléaire moyen.



# Statement of Originality

In this thesis, the systematic study of the anisotropies in the azimuthal distributions of identified particles with respect to the reaction plane has been performed as a function of particle rapidity, particle transverse momentum and collision centrality in Au+Au collisions at 11.5 A·GeV/c.

I have developed a robust procedure required to determine the measured reaction plane distribution. I have proposed a new development of the Fourier expansion method used to quantify the anisotropy in particle production relative to the reaction plane. Using a new technique for decoupling the elliptic component of the asymmetry from the directed component for the analysis of nucleon and fragment transverse flow, I have demonstrated that the proton elliptic flow at the AGS exhibits a rapidity dependence, with in-plane elliptic flow measured for mid-rapidity region, and out-of-plane elliptic flow measured at the projectile/target rapidities. The measured rapidity dependence of elliptic deformation of the flow tensor provides a good probe for the study of the transient pressure in the collision.

I have compared the proton elliptic flow data to the predictions of the RQMD v2.3 model. I have shown that the model explains general features exhibited by the experimental data, but a better quantitative description of the data is needed. I have also measured the elliptic flow signal of deuterons. It has been shown that the amplitude of deuteron elliptic flow is larger in the beam rapidity region compared to

that of protons. This trend is consistent with predictions of the coalescence model of deuteron production including volume effects.

My analysis detected a weak in-plane elliptic of pions for the first time at the AGS. The observed effect is attributed to the less effective screening of pions by the cold spectator nucleons at incident energies higher than those of Bevalac. I have also analyzed the azimuthal distributions of positive and negative kaons. I have shown that at the AGS  $K^+$  exhibit a weak negative directed flow.

# Contents

<b>1</b>	<b>Introduction</b>	<b>1</b>
1.1	The Quest for the Quark-Gluon Plasma . . . . .	1
1.2	Quantum Chromodynamics and Phase Transition . . . . .	2
1.3	Formation and Signatures of the QGP . . . . .	4
1.4	Equation of State and Collective Flow . . . . .	6
1.5	Outline . . . . .	9
<b>2</b>	<b>Collective Flow in Nuclear Collisions</b>	<b>10</b>
2.1	Radial Flow . . . . .	10
2.1.1	Fireball model . . . . .	11
2.1.2	Blast-wave scenario . . . . .	12
2.1.3	Longitudinal expansion . . . . .	15
2.1.4	Transverse expansion . . . . .	15
2.2	Azimuthally Anisotropic Flow . . . . .	18
2.2.1	Directed flow . . . . .	20
2.2.2	Elliptic flow . . . . .	30
2.3	Summary . . . . .	39
<b>3</b>	<b>E877 experiment at the AGS</b>	<b>40</b>
3.1	Beam Definition Detectors . . . . .	40

3.1.1	Beam counters . . . . .	41
3.1.2	Beam vertex detectors . . . . .	43
3.2	Calorimeters . . . . .	43
3.2.1	Target calorimeter . . . . .	44
3.2.2	Participant calorimeter . . . . .	45
3.2.3	Uranium calorimeter . . . . .	45
3.3	Forward Spectrometer . . . . .	46
3.3.1	Drift chambers . . . . .	47
3.3.2	Multi-wire proportional chambers . . . . .	48
3.3.3	Time-of-flight hodoscope . . . . .	49
3.3.4	Vertex detectors . . . . .	50
3.3.5	Forward scintillators . . . . .	51
<b>4</b>	<b>Data Reduction and Calibration</b>	<b>52</b>
4.1	Overview . . . . .	52
4.2	Calibration . . . . .	53
4.2.1	Participant calorimeter . . . . .	53
4.2.2	Drift chambers . . . . .	54
4.2.3	Time-of-flight hodoscope . . . . .	56
4.3	Spectrometer Alignment . . . . .	59
4.3.1	Alignment of tracking detectors . . . . .	59
4.3.2	Finding the <b>z</b> -position of DC2 . . . . .	62
4.3.3	Alignment of vertex chambers . . . . .	63
4.4	Track Reconstruction . . . . .	65
4.4.1	Track finding algorithm . . . . .	65
4.4.2	Particle identification . . . . .	68
4.4.3	Acceptance calculation . . . . .	74

4.4.4	Occupancy correction . . . . .	76
4.5	Centrality Determination . . . . .	77
<b>5</b>	<b>Flow Analysis Relative to the Reaction Plane</b>	<b>81</b>
5.1	Reaction Plane Determination . . . . .	82
5.2	Fourier analysis of azimuthal distributions . . . . .	86
5.3	Reaction plane resolution . . . . .	94
<b>6</b>	<b>Elliptic Flow of Protons and Deuterons</b>	<b>98</b>
6.1	Experimental Results . . . . .	98
6.1.1	$\langle p_x \rangle$ -subtraction . . . . .	101
6.1.2	Elliptic Flow of Protons and Deuterons . . . . .	105
6.2	Discussion . . . . .	114
6.2.1	RQMD comparison . . . . .	117
6.2.2	Coalescence afterburner . . . . .	123
6.2.3	Elliptic flow and collective expansion . . . . .	129
<b>7</b>	<b>Elliptic Flow of Charged Pions and Kaons</b>	<b>135</b>
7.1	Experimental Results on Flow of Pions . . . . .	135
7.2	Discussion . . . . .	141
7.3	Kaon identification . . . . .	147
7.4	Experimental Results on Flow of Kaons . . . . .	150
7.5	Discussion . . . . .	155
<b>8</b>	<b>Conclusions</b>	<b>159</b>



# List of Figures

1.1	Phase diagram of nuclear matter . . . . .	3
2.1	Center-of-mass kinetic energy spectra for light fragments emitted into $\theta_{c.m.} = 90^\circ \pm 15^\circ$ from the reaction Au+Au at $E = 1$ A·GeV . . . . .	14
2.2	Rapidity distributions for central 14.6 A·GeV/c Si+Au collisions compared with isotropic thermal distributions and distributions for a longitudinally expanding source . . . . .	16
2.3	Particle spectra for central 14.6 A·GeV/c Si+Au collisions at $y = 1.3$ compared to calculated spectra for a transversely expanding source . . . . .	17
2.4	Schematic view of the event shape in the center-of-mass frame . . . . .	19
2.5	View of a collision in the transverse plane . . . . .	20
2.6	Illustration of directed flow . . . . .	21
2.7	$d^2N/dp_x dp_y$ and $dN/d\phi$ distributions in the presence of positive directed flow . . . . .	21
2.8	Mean in-plane transverse momentum of the fragments versus normalized rapidity in the reaction Au+Au at Bevalac energies. . . . .	25
2.9	Comparison of measured values of $v_1$ for protons in Au+Au collisions at 10.8 GeV/c with those predicted by two versions of the RQMD event generator . . . . .	26

2.10	Flow parameter of the proton directed flow as a function of the beam kinetic energy per nucleon . . . . .	27
2.11	Excitation function of the transverse directed flow . . . . .	28
2.12	Illustration of elliptic flow . . . . .	30
2.13	$d^2N/dp_x dp_y$ and $dN/d\phi$ distributions in the presence of positive and negative elliptic flow . . . . .	31
2.14	Typical $dN/d\phi$ distributions for protons, deuterons and tritons measured in Bi+Bi collisions at 0.4 A-GeV . . . . .	35
2.15	Energy dependence from SIS to SPS energies of the elliptic flow . . .	36
2.16	Calculated elliptic flow excitation functions for Au + Au reactions . .	38
2.17	Out-of-plane/in-plane ratio for $\pi^+$ as a function of the transverse momentum for semicentral Au+Au collisions at 1 GeV/nucleon . . . . .	39
3.1	E877 experimental setup . . . . .	41
3.2	Beam scintillator counters . . . . .	42
3.3	Cherenkov beam counter . . . . .	42
3.4	Side and end views of the target calorimeter . . . . .	44
3.5	Participant calorimeter in various views . . . . .	46
3.6	Layout of the drift chambers . . . . .	48
3.7	Time-of-flight hodoscope wall . . . . .	49
3.8	Cross section of the vertex pad chamber assembly . . . . .	50
4.1	Time offsets in DC2 and DC3 plane before and after calibration . . .	55
4.2	Measured pulse height distribution for a counter near the beam particle trajectories . . . . .	57
4.3	Residuals of the fit to straight tracks used to align the components of the spectrometer . . . . .	60

4.4	Difference between the measured position and fitted position for the two BVERs, DC2 and DC3 after corrections . . . . .	61
4.5	Difference between the measured position and fitted position $\delta x$ for the four MWPCs before and after correction . . . . .	62
4.6	Width of the track focus spot at $z = 0$ as function of the assumed $z$ -position of DC2 . . . . .	63
4.7	Dependence of the $x$ -distance between track and its closest cluster on the $x$ -position of the cluster for VTXA, VTXB before corrections . . .	64
4.8	Dependence of the $x$ -distance between track and its closest cluster on the $x$ -position of the cluster for VTXA, VTXB after corrections . . . .	65
4.9	$x - z$ view of a typical Au+Au event in E877 event display program .	67
4.10	Scatter plot of the inverse momentum $1/p$ versus the inverse of the measured velocity $1/\beta$ . . . . .	69
4.11	Mass spectra of positive particles in different momentum windows . .	70
4.12	Mass squared resolution for protons, positive pions, and positive kaons as a function of momentum . . . . .	71
4.13	Contour plot of mass versus momentum distribution with PID cuts shown by the solid lines . . . . .	73
4.14	Measured mass squared distributions of positive particles in the momentum range of $1.5 < p < 2.0$ GeV/c for different vertex cuts . . . .	74
4.15	Calculated acceptance of various particles in the E877 spectrometer as a function of $p_t$ and $y$ . . . . .	75
4.16	Probability of track survival as a function of track separation in DC2, DC3 and TOFU . . . . .	76
4.17	$dN/dE_t$ distribution and transverse energy differential cross-section for PCAL . . . . .	78
4.18	Centrality as a function of $E_t$ for TCAL and PCAL . . . . .	79

5.1	Distribution of transverse energy vector and determined reaction plane angle in the PCal4 pseudorapidity window . . . . .	84
5.2	Residuals of the reaction plane angle determined in the PCal4 pseudorapidity window and its corrected value for each step of the correction procedure . . . . .	87
5.3	Illustration of the $p_t$ -dependence of the $v_1$ and $v_2$ coefficients using a simplified schematic model . . . . .	89
5.4	$v_1$ and $v_2$ as a function of $p_t$ for Monte Carlo simulated momentum distributions shifted by different $\langle p_x \rangle$ . . . . .	90
5.5	Monte Carlo simulated momentum distribution and its $v_1(p_t)$ and $v_2(p_t)$ signals in two different reference frames . . . . .	92
5.6	Same as Fig. 5.5, but with limited $p_t$ acceptance . . . . .	93
5.7	Inverse correction factors for the first and second moment in four different bins of pseudorapidity . . . . .	95
5.8	Inverse correction factors for $v_1$ , with and without optimization, in four different bins of pseudorapidity . . . . .	96
5.9	Inverse correction factors for $v_1$ and $v_2$ in the combined window $2.0 < \eta < 4.5$ . . . . .	97
6.1	$v_2(p_t)$ of protons for different rapidity and centrality bins . . . . .	100
6.2	Contour plot of $d^2N/dp_x dp_y$ distributions for protons and deuterons .	101
6.3	Mean transverse momentum in the reaction plane of protons and deuterons . . . . .	103
6.4	$v_1(p_t)$ and $v_1'(p'_t)$ of protons for various rapidity bins and collision centralities . . . . .	104
6.5	$v_2'(p'_t)$ and $v_2(p_t)$ of protons for various rapidity bins and collision centralities . . . . .	106

6.6	$v'_2(p'_t)$ and $v_2(p_t)$ of deuterons for various rapidity bins and collision centralities . . . . .	107
6.7	Fit of $v'_2(p'_t)$ of protons . . . . .	110
6.8	$v'_2(y)$ of protons for different collision centralities . . . . .	112
6.9	Fit of $v'_2(p'_t)$ of deuterons . . . . .	113
6.10	Elliptic flow of protons as a function of rapidity for 158 A·GeV Pb+Pb collisions and 11.5 A·GeV Au+Au collisions . . . . .	115
6.11	RQMD 2.3 (Cascade) rapidity distributions of participant and spectator protons for $\sigma_{top}/\sigma_{geo}=7\%$ . . . . .	118
6.12	Comparison of proton $v'_2(p'_t)$ data with calculations of RQMD v2.3 run in cascade mode . . . . .	120
6.13	Comparison of proton $v'_2(p'_t)$ data with calculations of RQMD v2.3 run in mean field mode . . . . .	121
6.14	Comparison of proton $v'_2(y)$ data with calculations of RQMD v2.3 run in cascade and mean field modes . . . . .	122
6.15	Comparison of deuteron $v'_2(p'_t)$ data with calculations of coalescence model combined with the RQMD v2.3 event generator run in cascade mode . . . . .	124
6.16	Comparison of deuteron $v'_2(p'_t)$ data with calculations of coalescence model combined with the RQMD v2.3 event generator run in mean field mode . . . . .	125
6.17	$v'_2(y)$ for deuterons as calculated by the coalescence model combined with RQMD v2.3 run in cascade and mean field modes . . . . .	126
6.18	$v'_2(p_t)$ of protons and deuterons in the coalescence model combined with RQMD v2.3 (mean field) event generator . . . . .	127
6.19	$v_1(p_t)$ of protons and deuterons in the coalescence model combined with RQMD v2.3 event generator . . . . .	128

6.20	Deuteron mass spectra at $\phi' = 0^\circ$ and $\phi' = 90^\circ$ for Au+Au collisions at 600 A·MeV . . . . .	130
6.21	Proton transverse mass spectra for particles emitted into the three bins in the azimuthal angle $\phi'$ . . . . .	132
6.22	Average transverse expansion velocity $\langle\beta_t\rangle$ as a function of the azimuthal angle $\phi'$ . . . . .	133
7.1	Mean transverse momentum in the reaction plane of protons and negative pions . . . . .	136
7.2	$v_1(p_t)$ of positive and negative pions for different rapidity and centrality bins . . . . .	137
7.3	$v_2(p_t)$ of positive and negative pions for different rapidity and centrality bins . . . . .	139
7.4	$v_1(p_t)$ and $v_2(p_t)$ of positive pions for rapidity bin $2.8 < y < 3.2$ and different collision centralities . . . . .	140
7.5	$v_1(p_t)$ and $v_2(p_t)$ of negative pions for rapidity bin $2.8 < y < 3.2$ and different collision centralities . . . . .	140
7.6	Rapidity dependence of directed and elliptic flow of negative pions for different collision centralities . . . . .	141
7.7	Elliptic flow parameter $P_2$ for mid-rapidity $\pi^+$ and $\pi^-$ as a function of the transverse momentum measured for semicentral $^{209}\text{Bi}+^{209}\text{Bi}$ collisions at 400, 700, and 1000 A·MeV . . . . .	143
7.8	Comparison of $\pi^- v_2(p_t)$ data with calculations of RQMD v2.3 run in cascade mode . . . . .	145
7.9	Comparison of $\pi^- v_2(p_t)$ data with calculations of RQMD v2.3 run in mean field mode . . . . .	145

7.10	Comparison of $\pi^- v_2(y)$ data with calculations of RQMD v2.3 run in cascade and mean field modes . . . . .	146
7.11	Momentum versus mass squared contour plot with and without vertex chamber confirmation . . . . .	148
7.12	Mass squared distributions for negative and positive kaons in different momentum windows . . . . .	149
7.13	Acceptance plots for positive and negative kaons . . . . .	150
7.14	$v_1(p_t)$ of positive and negative kaons for different rapidity and centrality bins . . . . .	151
7.15	$v_2(p_t)$ of positive and negative kaons for different rapidity and centrality bins . . . . .	152
7.16	Azimuthal distributions of positive kaons . . . . .	153
7.17	Azimuthal distributions of positive kaons for different rapidity and centrality bins . . . . .	154
7.18	Azimuthal distributions of negative kaons for different rapidity and centrality bins . . . . .	155
7.19	$v_1(y)$ for $K^+$ and $K^-$ as calculated by the RQMD v2.3 run in cascade and mean field modes . . . . .	157
7.20	$v_2(y)$ for $K^+$ and $K^-$ as calculated by the RQMD v2.3 run in cascade and mean field modes . . . . .	157



# List of Tables

4.1	1994 detector positions and parameters of 1995 alignment . . . . .	67
4.2	Parameters of particle identification . . . . .	73
4.3	Maximum momentum cuts for different particles . . . . .	74
5.1	Definition of windows in polar angle and pseudorapidity for the determination of the reaction plane . . . . .	84
6.1	Definition of the centrality regions . . . . .	100
6.2	Inverse slope parameters $T_B$ of protons . . . . .	110
6.3	Ellipticity parameter $\varepsilon$ of protons for different rapidities and collision centralities . . . . .	112
6.4	$v_2'$ of protons and deuterons in the rapidity region $3.0 < y < 3.2$ for different collision centralities . . . . .	114



# Acknowledgments

First and foremost I must thank my wife for her love and unconditional support during my studies at McGill. I am forever indebted to her as she sacrificed her career in medicine to be with me during all these years. I dedicate this thesis to her and our daughter.

I want to express my sincere gratitude to my advisors, Prof. Jean Barrette and Prof. S. K. Mark. I thank Tommy Mark for his interest in me and providing the opportunity to study here, as I was the first (in recent memory) student from Russia to be accepted to a graduate program at the department of Physics. His guidance during my first years of graduate school and research was a great deal of help, for which I am very grateful. I am enormously indebted to Jean Barrette, the leader of the E877 group at McGill, for his advice and guidance throughout this work. This thesis could not have been written without his input. I thank him from the bottom of my heart.

I thank Sergei Panitkin, who encouraged me to pursue particle physics and led me through my Bachelor's and Master's degrees. He was my inspiration to stay in physics and to come to North America for a Ph.D.

My warmest thanks go to another good friend of mine, Nickolai Starinski, who is now at the South Pole. He has helped me more than I deserved.

I am grateful to Sergei Voloshin for his generosity in sharing ideas and the in-

valuable discussions we have had. I also learned a great deal from Profs. Peter Braun-Munzinger, Johanna Stachel and Tom Hemmick.

I must thank my fellow graduate students, Yi Dai and Yujin Qi, who have been my constant companions in the quest which is about to end. I wish them all the best in their future endeavors. I owe my gratitude to Roger Lacasse, who always gave me a hand whenever I needed help. I want to thank Thongbay Vongpaseuth, without whom the analysis of the 1995 data would not have been possible. I am thankful to Mark Pollack and Stephen Johnson for all their help.

I also wish to thank my colleagues and good friends Sergei Sedykh and Vlad Pantuev. My special thanks go to Marzia Rosati, who had a great influence on me while we were working on the PHENIX experiment. I would also like to thank Ed O'Brien and Jeff Mitchell for their help during that period.

I am grateful to Steve Kecani, Leo Nikkinen and Vasile Topor Pop.

Finally, I wish to thank all the members of the E877 collaboration.

The E877 collaboration: J. Barrette<sup>5</sup>, R. Bellwied<sup>9</sup>, S. Bennett<sup>9</sup>, R. Bersch<sup>7</sup>, P. Braun-Munzinger<sup>2</sup>, W. C. Chang<sup>7</sup>, W. E. Cleland<sup>6</sup>, M. Clemen<sup>6</sup>, J. Cole<sup>4</sup>, T. M. Cormier<sup>9</sup>, Y. Dai<sup>5</sup>, G. David<sup>1</sup>, J. Dee<sup>7</sup>, O. Dietzsch<sup>8</sup>, M. Drigert<sup>4</sup>, K. Filimonov<sup>5</sup>, S. C. Johnson<sup>7</sup>, J. R. Hall<sup>9</sup>, T. K. Hemmick<sup>7</sup>, N. Herrmann<sup>2</sup>, B. Hong<sup>2</sup>, Y. Kwon<sup>7</sup>, R. Lacasse<sup>5</sup>, Q. Li<sup>9</sup>, T. W. Ludlam<sup>1</sup>, S. K. Mark<sup>5</sup>, R. Matheus<sup>9</sup>, S. McCorkle<sup>1</sup>, J. T. Murgatroyd<sup>9</sup>, D. Miśkowiec<sup>2</sup>, E. O'Brien<sup>1</sup>, S. Panitkin<sup>7</sup>, V. Pantuev<sup>7</sup>, P. Paul<sup>7</sup>, T. Piazza<sup>7</sup>, M. Pollack<sup>7</sup>, C. Pruneau<sup>9</sup>, Y. Qi<sup>5</sup>, M. N. Rao<sup>7</sup>, E. Reber<sup>4</sup>, M. Rosati<sup>5</sup>, N. C. daSilva<sup>8</sup>, S. Sedykh<sup>7</sup>, U. Sonnadara<sup>6</sup>, J. Stachel<sup>3</sup>, E. M. Takagui<sup>8</sup>, S. Voloshin<sup>3</sup>, T. B. Vongpaseuth<sup>7</sup>, G. Wang<sup>5</sup>, J. P. Wessels<sup>3</sup>, C. L. Woody<sup>1</sup>, N. Xu<sup>7</sup>, Y. Zhang<sup>7</sup>, C. Zou<sup>7</sup>

<sup>1</sup>BNL - <sup>2</sup>GSU - <sup>3</sup>Univ. of Heidelberg - <sup>4</sup>Idaho Nat. Eng. Lab. - <sup>5</sup>McGill Univ. - <sup>6</sup>Univ. of Pittsburgh - <sup>7</sup>SUNY, Stony Brook - <sup>8</sup>Univ. of São Paulo, Brazil - <sup>9</sup>Wayne State Univ.

# Chapter 1

## Introduction

### 1.1 The Quest for the Quark-Gluon Plasma

Theoretical and experimental studies of hot and/or dense nuclear matter constitute one of the most active frontiers in modern physics. This field of research is of cross-disciplinary interest to nuclear and particle physics, astrophysics and cosmology. It offers the only means to study the fundamental theory of strong interactions in the limit of extremely high temperatures and densities [1]. It is predicted that under such conditions ordinary nuclear matter can be transformed into a plasma of quarks and gluons. The universe is believed to have consisted of such a plasma just a few microseconds after the Big Bang explosion. It may still exist in the cores of dense neutron stars.

A quark-gluon plasma state can be created in the laboratory by collisions between two nuclei at very high energy. When two relativistic heavy ions smash into each other, large amount of energy is deposited in the collision volume of nuclear dimensions, which creates high baryon density and temperature. Beams of heavy nuclei with energies of tens of GeV per nucleon are currently available at the Brookhaven

Alternating Gradient Synchrotron (AGS) and the CERN Super Proton Synchrotron (SPS). The Brookhaven Relativistic Heavy Ion Collider (RHIC) and CERN Large Hadron Collider (LHC) which are now under construction will provide beams with energies reaching another order of magnitude. One of the main goals of present and future experiments at these facilities is to study the formation of hot and dense hadronic matter and its possible transition to the quark-gluon plasma.

## 1.2 Quantum Chromodynamics and Phase Transition

The ultimate theory of strong interaction, the quantum chromodynamics (QCD), describes nuclear matter through the interaction of its fundamental constituents, quarks, by the exchange of color force carriers, gluons. It exhibits two fundamental and related features, one is the color confinement, and the other is approximate chiral symmetry and its spontaneous breaking. The former expresses the fact that quarks have never been observed isolated, but only in hadronic bound states, such as baryons and mesons. The chiral symmetry manifests itself in the smallness of current quark masses and the vanishing quark condensate in vacuum. It is spontaneously broken in nature, with the value of the quark condensate, which describes the density of quark-antiquark pairs found in the QCD vacuum, of  $\langle \bar{\psi}\psi \rangle \approx (235 \text{ MeV})^3$  [2]. The quarks confined in hadrons have large effective masses ( $\tilde{m}_u \approx \tilde{m}_d \approx 300 \text{ MeV}$ ,  $\tilde{m}_s \approx 500 \text{ MeV}$ ) obtained by interactions among themselves and with surrounding vacuum. According to the QCD calculations, the quark condensate decreases with increasing temperature of a hadronic system. At higher temperatures, spontaneously broken chiral symmetry is expected to be gradually restored. The high density of color charges leads to a screening of long range confining forces, resulting in a color deconfinement. At very

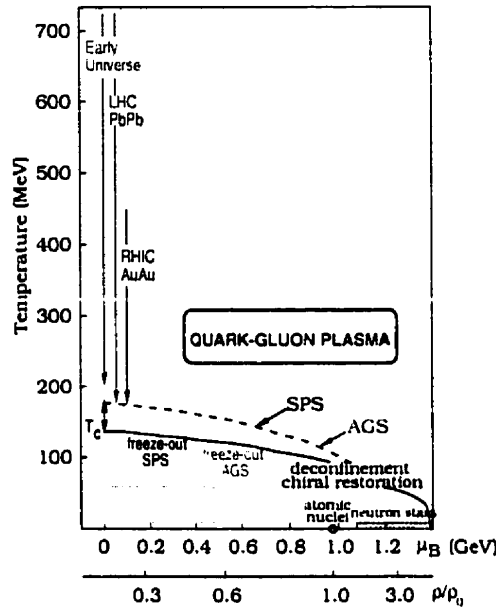


Figure 1.1: Phase diagram of nuclear matter (from [3]).

high temperatures/densities nuclear matter is predicted to undergo a phase transition to a state where color degrees of freedom are no longer confined, the quark-gluon plasma.

Numerical simulations of the QCD equation of state on a finite discretized volume of space-time, usually referred to as lattice gauge theory, have established the transition temperature to lie in the range  $150 \pm 10$  MeV at vanishing net quark density. Chiral symmetry is also expected to be restored at high baryon density ( $4\rho_0 < \rho_c < 10\rho_0$ ) even at zero temperature. The phase diagram of nuclear matter is presented in Fig 1.1, where the predicted phase boundary is shown as the baryon chemical potential  $\mu_B$ , and the nuclear density  $\rho/\rho_0$ , where  $\rho_0 \approx 0.17 \text{ GeV}/\text{fm}^3$  is the normal nuclear density, versus the system's temperature. At relatively low temperatures/densities the nuclear matter can be described as an interacting hadronic gas. The QGP is formed when the hadronic system is excited beyond the boundary of the phase transition.

An analysis of recent experimental data from the AGS and SPS indicates that large energy deposition and high degree of stopping of baryons lead to the formation of a hot and dense fireball of excited nuclear matter, whose temperature and density may traverse the transition region into the quark-gluon plasma regime [3]. When completed in 1999, the Relativistic Heavy Ion Collider will provide beams of heavy ions capable of reaching temperature and density trajectories that lie close to that of the early universe [4].

### 1.3 Formation and Signatures of the QGP

There are two main approaches to describing the collision process at the parton level: QCD string breaking and the partonic cascade. Regardless of the model, rescattering of the partons leads to the formation of a thermalized state. A local thermal equilibrium is characterized by the condition that the mean free path of constituents is much less than the system dimensions. The evolution of the quark-gluon plasma after it has reached the thermodynamical equilibrium can be described in the framework of relativistic hydrodynamics. The thermalization is followed by the mainly longitudinal expansion of the fireball, together with the chemical equilibration. The expanding system cools down until it reaches the critical transition temperature. At that stage (a few  $fm/c$  after the collision), the matter stays at the mixed phase where the quark-gluon plasma converts into a hadronic gas. Hadronization is followed by the final state interactions.

Much work has expanded in developing techniques and probes which are sensitive to the presence of a QGP phase. The problem is the expected small size (a few fermi in diameter) and short lifetime ( $5 - 10 fm/c$ ) of the plasma. Furthermore, the hot hadronic gas phase following the hadronization of plasma and the strong final state interactions will obscure possible signals emerging from the plasma state.

Nevertheless, a number of different methods for observation of the QGP have been proposed so far. The possible signatures sensitive to phenomena associated with the creation of plasma include:

- **Color Deconfinement**

- *Charmonium Suppression*: Formation of a ( $c\bar{c}$ ) bound state is expected to be suppressed inside the quark-gluon plasma.
- *Hard Quark and Gluon Jets*: Energy loss of a fast parton can probe the stopping power of plasma.

- **Chiral Symmetry Restoration**

- *Penetrating Electromagnetic Probes - Lepton Pairs and Direct Photons*: Provide information of the interior of the quark-gluon plasma during the earliest and hottest phase of its evolution.
- *Strangeness and Antibaryon Enhancement*: The threshold for production of strange hadrons and baryon-antibaryon pairs is lower in the presence of the QGP.
- *Disoriented Chiral Condensates (DCC's)*: Domains of DCC's may be formed, resulting in fluctuation of a charge to neutral pion multiplicity ratio.

- **Equation of State**

- Possible modifications in the dependence of energy density  $\epsilon$ , pressure  $P$ , and entropy density  $s$  of superdense hadronic matter on temperature  $T$  and baryochemical potential  $\mu_B$ .

To date, the measurements have not been able to observe an unambiguous signal for the quark-gluon plasma. However, some experimental results are quite peculiar

and may indicate a QGP creation. The future experiments at RHIC and LHC will examine an entire spectrum of possible signatures of the QGP formation. An experimental demonstration of a combination of signals would constitute the discovery of the quark-gluon plasma.

## 1.4 Equation of State and Collective Flow

An investigation of the equation of state (EOS) of nuclear matter, relating the dependence of the pressure on the density and temperature of the excited system, is of fundamental interest. The influence of a phase transition in the EOS on the collective dynamical evolution of the system is predicted by recent lattice QCD calculations. It was shown that close to the critical temperature the pressure is rising with temperature more slowly than the energy density. The tendency of matter to expand is thus reduced and in this temperature region the equation of state of nuclear matter is unusually "soft".

One of the observables which is related to the stiffness of the equation of state is collective flow. The hot and compressed nuclear matter behaves like a compressible fluid. The first application of a fluid-dynamics model for description of collisions of nucleons and nuclei was made in the classical work by L.D. Landau [5]. Later studies [6, 7, 8] assumed that hydrodynamics was governed by the formation of a shock wave that could be formed when a high-energy particle exceeding the nuclear speed of sound passes through a nucleus. The models examining the effects of shock waves during nucleus-nucleus collisions showed that the transverse front of the stopped and shocked matter was expanding faster than the longitudinal front, resulting in nucleons being pushed outwards perpendicular to the relative motion of the two nuclei.

The first experimental evidence of this collective motion was obtained at the Bevalac in Berkeley [9, 10]. The data from  $4\pi$  detectors, the Plastic Ball and the

Streamer Chamber, confirmed fluid-dynamics predictions for the occurrence of side-ward flow. The flow effects have since been studied in great detail in a wide energy range, starting from low and intermediate energy ( $\approx 0.1$  A·GeV) experiments at the NSCL of Michigan State University and GANIL, to relativistic energies of the Bevalac-LBL and SIS-GSI ( $\approx 1$  A·GeV), and recently extending to the experiments at ultra-relativistic energies of the AGS-BNL ( $\approx 10$  A·GeV) and SPS-CERN ( $\approx 200$  A·GeV). A detailed review of the collective flow phenomena observed at all available energies is given in [11]. The energy range of several orders of magnitude allows the investigation of possible changes in the flow behaviour with respect to the incident energy.

During the course of a collision between two heavy nuclei, initial compression and heating are followed by an expansion stage. The expansion dynamics of equilibrating matter is governed by the EOS, and the collective motion driven by the pressure gradients can be used as a tool to study the transient pressure built up through all the stages of compression, heating and subsequent expansion.

Two types of flow patterns may be developed as the system expands: (1) axially symmetric radial flow, and (2) azimuthally anisotropic transverse flow.

The radial expansion is azimuthally isotropic, and, in low and intermediate energy heavy-ion collisions, it is also spherically symmetric. At higher relativistic energies, the radial expansion is considered separately in the transverse and longitudinal directions.

The radial flow is the most pronounced in very central collisions. It manifests itself in the appearance of a “shoulder arm” and mass dependence in the slopes of the transverse momentum spectra of identified particles, not compatible with the assumption of a purely thermal distribution. The radial flow was suggested to be a sequence of a blast wave from compressed nuclear matter. In this picture, the isotropic expansion converts part of the initial thermal energy into radial flow before the final

breakup of the hot equilibrated system. Understanding radial flow is essential to determine the freeze-out temperature and the chemical properties of nuclear matter.

At relativistic energies, the symmetry becomes cylindrical, and the expansion may be broken into longitudinal and transverse components. The longitudinal flow (along the beam direction) reveals itself in the widening of the rapidity distributions of identified particles. But due to uncertainty in initial conditions the longitudinal expansion can not be very useful in extracting the parameters of the EOS.

The transverse expansion is predicted to be very sensitive to the equation of state. Contrary to the longitudinal expansion, the absence of “primordial” transverse motion makes it possible to neglect initial conditions.

In addition to the transverse component of the azimuthally symmetric radial flow, the geometry of the collision may lead to the appearance of azimuthal anisotropies in the particle distributions in the transverse plane. The measurement of these azimuthal anisotropies requires the knowledge of a reaction plane, defined by the impact parameter vector and the incident beam direction, which is best accessible to experimental observation in semi-central collisions.

Two major types of azimuthally anisotropic flow have been studied more extensively both experimentally and theoretically: directed transverse flow and elliptic transverse flow. The directed flow describes the collective sideward motion of particles, and elliptic flow signals the elliptical deformation of the flow tensor. The existence of two transverse flow components provides additional valuable information on the transient pressure. The study of higher-order azimuthal asymmetries is also of interest [12].

## 1.5 Outline

The thesis is devoted primarily to the study of elliptic flow. However, for correct interpretation of the obtained results it is essential to have a complete picture of the reaction dynamics, as different flow effects may have an influence on each other. In the next chapter we present an overview of collective flow effects observed in nucleus-nucleus collisions. The current status of experimental and theoretical efforts is also discussed therein. The E877 experiment is described in chapter 3. The details of calibration procedures and data reduction are given in chapter 4. The method used to measure the reaction plane is discussed in chapter 5. The results and discussion of Fourier analysis of elliptic flow of protons and deuterons are presented in chapter 6. Elliptic flow of charged pions and kaons is studied in chapter 7. Conclusions and summary of the results are given last.

## Chapter 2

# Collective Flow in Nuclear Collisions

One of the major goals of physics of heavy-ion collisions is to learn the equation of state of hot/dense hadronic matter. The details of the dense stage are obscured by the re-scatterings, but some are preserved and accumulated during the expansion: collective flow is a tool to study them. A detailed overview of collective flow phenomena is given in [11]. Below we discuss the phenomenology of different aspects of the collective behaviour. The reader is also referred to [13].

### 2.1 Radial Flow

The radial flow characterizes the expansion phase and is very important for a full thermodynamic description of the collision and the freeze-out. Its very existence was debated for years, but now it is widely accepted that the experimental measurements of particle spectra can only be understood by introducing the radial flow velocities. The basic feature of the measured transverse momentum spectra is the exponential decay over several orders of magnitude with an almost uniform slope. For the

thermalized system the particle spectra reflect the temperature of the system at the time when the particles decouple, i.e. the freeze-out temperature. The observed distributions are also influenced by the collective motion and resonance decays.

The radial flow has been studied experimentally over a wide energy range spanning from Bevalac/SIS energies [14, 15] to the AGS [16] and SPS [17] experiments. The detailed analysis of the shape of the measured particle spectra provides necessary constraints on different theoretical models.

### 2.1.1 Fireball model

The fireball model [18] was the first attempt to describe the measured cross sections in a heavy-ion collision by a collective thermal model. In such approach, the matter is assumed to be globally thermalized by the end of the reaction, and the cross section is determined from the thermal momentum distributions of the particles. The invariant momentum spectrum of particles radiated by a thermal source with temperature  $T$  is given by

$$E \frac{d^3 N}{d^3 p} = \frac{gV}{(2\pi)^3} E e^{-(E-\mu)/T}, \quad (2.1)$$

where  $E$  is the energy,  $g$  is the spin-isospin degeneracy factor for the particle species,  $\mu$  is the grand canonical potential,  $V$  is the volume of the source. The model assumes that the matter is close to an ideal gas at break-up and collective flow is not included. In terms of measurable observables, the dynamics of the collision zone at freeze-out can be revealed by analyzing the Boltzmann-like shape of the transverse mass  $m_t = \sqrt{p_t^2 + m^2}$  spectrum, which is usually fit by

$$\frac{d^2 N}{m_t^2 dm_t dy} = N_0(y) \exp\left(-\frac{m_t - m}{T_B}\right), \quad (2.2)$$

where  $y = \tanh^{-1}(p_z/E)$  is the rapidity of the particle and  $T_B$  is the slope parameter.

This simple model was very powerful and provided a good description of many experimental results. However, it has been shown that in the high energy heavy-ion

collisions the observed hadrons do not exhibit the simple, purely thermal distributions. In the thermal model, all emitted particles should have the same average kinetic energy. The experimental measurements revealed an existence of two phenomena not compatible with this assumption: (1) an appearance of a “shoulder arm” in the kinetic energy spectra of identified particles, and (2) a quasi-linear dependence of the average kinetic energy on the particle mass. Both of these features provide an experimental evidence for the existence of radial flow.

### 2.1.2 Blast-wave scenario

One of the models which was developed to explain the shape of the particle spectra demonstrated that the observed cross sections may be understood as typical of the blast pressure wave produced by the exploding nuclear matter [19]. The adiabatic expansion of the hot and dense fireball leads to a blast wave, the energy for which comes from the primordial isotropic thermal energy of particle random motion. In a hydrodynamical approach, the matter locally acquires an outward-directed macroscopic radial flow velocity  $\beta_r$  by converting internal thermal energy into work through a pressure gradient  $\nabla P$ . The resulting final break-up state thus has a collective expansion or radial flow superimposed with the thermal motion. The observed particle velocities have then two components

$$\mathbf{v} = \beta_r + \mathbf{v}_{\text{therm}}. \quad (2.3)$$

Collective flow velocity is assumed to be the same for all particles, and the thermal random velocity is deduced from the thermal temperature, which is also common for all particles. The average kinetic energy of a particle with mass  $m$  is then

$$\langle E \rangle \approx \langle E_{\text{flow}} \rangle + \langle E_{\text{therm}} \rangle = m \left( \frac{1}{\sqrt{1 - \beta_r^2}} - 1 \right) + \frac{3}{2}T. \quad (2.4)$$

While the thermal energy is independent of  $m$ , the collective flow contribution is proportional to  $m$ . As a consequence, the model explains the basic feature exhibited by the experimental data, that is the energy spectra of pions decrease more steeply with energy than proton spectra. The energy distribution in the center of mass for particles emitted from a thermally equilibrated, radially expanding source characterized by a temperature  $T$  and a radial flow velocity  $\beta_r$  is given by [19]

$$\frac{dN}{dEd\Omega} = \frac{8\pi e^{\mu/T}}{(2\pi\hbar)^3} \exp\left(\frac{-\gamma E}{T}\right) \left[ \left(\gamma + \frac{T}{E}\right) \frac{\sinh \alpha}{\alpha} - \frac{T}{E} \cosh \alpha \right], \quad (2.5)$$

where  $E$  and  $p$  are the total energy and momentum of the particle in the center of mass,  $\gamma = (1 - \beta_r^2)^{-1/2}$ , and  $\alpha = \gamma\beta_r p/T$ . Fig 2.1 shows kinetic energy spectra measured by the EOS collaboration for light fragments in Au+Au collisions at 1 A-GeV [14]. The experimental data are fitted with a purely thermal model and a blast-wave model. The expression (2.5) describes well the “shoulder arm” shape of the spectra and provides the “true” hadronic decoupling temperature. The same temperature  $T$  and radial flow velocity  $\beta$  simultaneously describe all the spectra, whereas fitting with the Maxwell-Boltzmann interpretation (2.2) would suggest a much higher temperature that also changes with emitted particle type.

The original blast-wave model [19] assumed a constant radial flow velocity. The later developments [20, 21] suggested using a radial velocity profile of type

$$\beta_r(r) = \beta_s \left(\frac{r}{R}\right)^n, \quad (2.6)$$

where  $R$  is the freeze-out radius of the system,  $\beta_s$  is the maximum surface velocity,  $n$  is the parameter varying the form of the profile. As the experimental program developed to relativistic and ultra-relativistic energies, the radial flow could no longer be considered as spherically symmetric, so longitudinal and transverse expansions are treated separately at these energies.

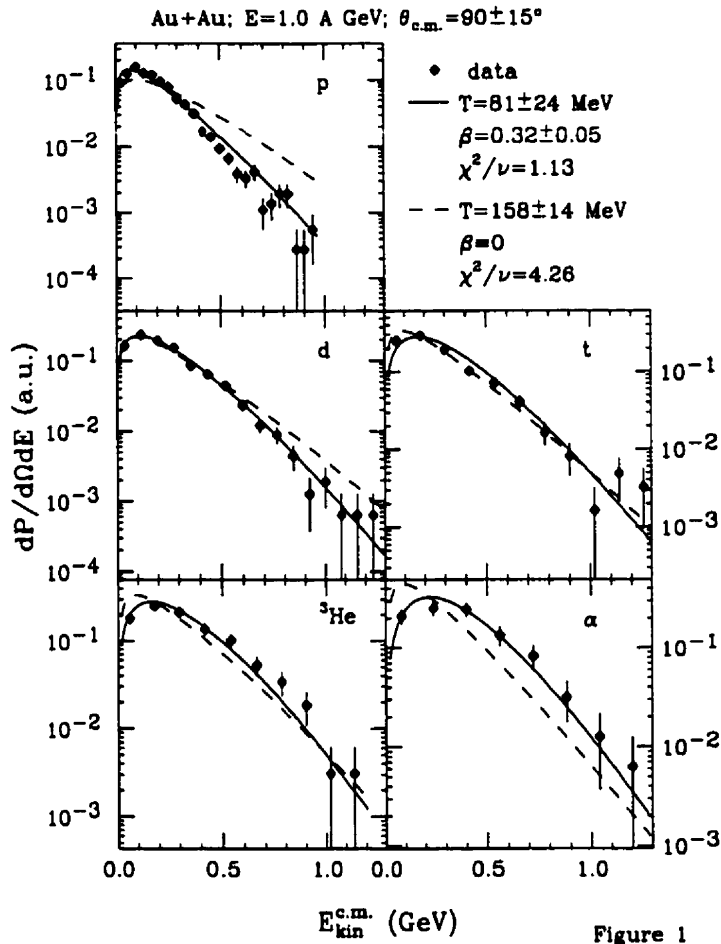


Figure 2.1: Center-of-mass kinetic energy spectra for light fragments emitted into  $\theta_{c.m.} = 90^\circ \pm 15^\circ$  from the reaction Au+Au at  $E = 1$  A-GeV. Also shown are the fits of the spectra assuming a radially expanding thermal source (solid lines), and a purely thermal source (dashed lines) (from [14]).

### 2.1.3 Longitudinal expansion

In an isotropic thermal model, the rapidity distribution is obtained by integrating equation (2.1) over  $m_t$ :

$$\frac{dN_{therm}}{dy} \sim m^2 T (1 + 2\chi + 2\chi^2) \exp(-1/\chi), \quad (2.7)$$

where  $\chi = T/(m \cosh y)$ . The measured rapidity distributions are much wider than given by the above expression. Such an anisotropy can be explained by introducing a common collective flow velocity in longitudinal direction. The boost-invariant longitudinal expansion model was originally postulated by Bjorken [22] for asymptotically high energies. A phenomenological model [23] modified the boost-invariant scenario by restricting the boost angle  $\eta$  to the interval  $(\eta_{min}, \eta_{max})$ . The rapidity distribution is then the integral over the uniformly distributed thermal sources (2.7) boosted individually by  $\eta$ :

$$\frac{dN}{dy} = \int_{\eta_{min}}^{\eta_{max}} d\eta \frac{dN_{therm}}{dy}(y - \eta). \quad (2.8)$$

A comparison of the measured rapidity distributions for central 14.6 A·GeV/c Si+Au collisions with isotropic thermal distributions at  $T=0.12$  GeV and distributions for a source at the same temperature expanding longitudinally with a mean velocity  $\langle\beta_l\rangle = 0.52c$  are shown in Fig. 2.2 (from [24]). The agreement between the measured distributions and the model with a longitudinal flow is remarkably good for all particle species.

### 2.1.4 Transverse expansion

In the same phenomenological approach, the transverse momentum spectra are obtained by boosting the thermal sources with the boost angle  $\rho = \tanh^{-1} \beta_t$ , with the transverse velocity distribution  $\beta_t(r)$  parameterized with the profile (2.6):

$$\frac{dN}{m_t dm_t} \sim \int_0^R r dr m_t I_0 \left( \frac{p_t \sinh \rho}{T} \right) K_1 \left( \frac{m_t \cosh \rho}{T} \right), \quad (2.9)$$

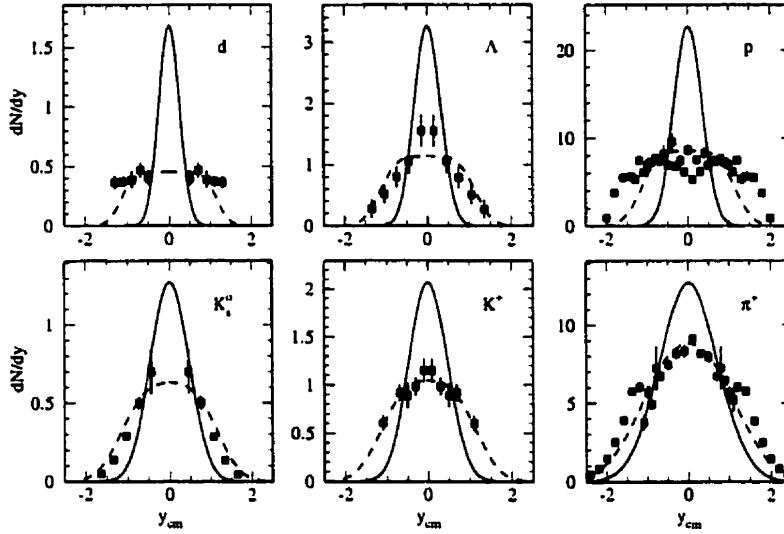


Figure 2.2: Rapidity distributions for central 14.6 A-GeV/c Si+Au collisions compared with isotropic thermal distributions at  $T=0.12$  GeV (solid lines) and distributions for a source at the same temperature expanding longitudinally with a mean velocity  $\langle\beta_t\rangle = 0.52c$  (dashed lines) (from [24]).

where  $I_0, K_1$ , are the modified Bessel functions defined as

$$I_0 = \frac{1}{2\pi} \int_0^{2\pi} e^{z \cos \phi} d\phi,$$

$$K_1 = \int_0^\infty \cosh ye^{-z \cosh y} dy.$$

The fits of the above expression to the data (Fig. 2.3 from [24]) with linear ( $n = 1$ ) velocity profile result in the average transverse expansion velocity  $\langle\beta_t\rangle = 0.39$  (0.33) $c$  at  $T = 0.12$  (0.14) GeV. The fit is consistent with two choices of  $(T, \langle\beta_t\rangle)$  coordinates alluding to a well-known fact that in such phenomenological analysis the transverse spectra may be described by a wide range of  $(T, \langle\beta_t\rangle)$  pairs, as both parameters are highly correlated.

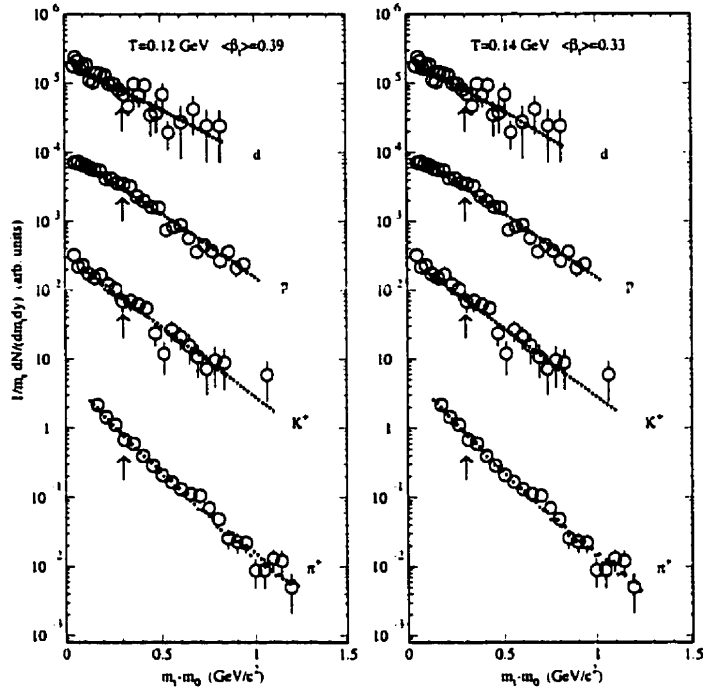


Figure 2.3: Particle spectra for central 14.6 A·GeV/c Si+Au collisions at  $y = 1.3$  compared to calculated spectra for a source at  $T = 0.12$  GeV expanding transversely with a mean velocity  $\langle\beta_t\rangle = 0.39c$  (left) and a source at  $T = 0.14$  GeV and  $\langle\beta_t\rangle = 0.33c$  (right). The arrows indicate the beginning of the fit region (from [24]).

The radial flow velocities are found to be maximal in the most central collisions and increase as a function of beam energy. Up to now, all the available experimental data on the slopes of particle spectra can be consistently described within a hydrodynamical picture by a freeze-out temperature and a radial flow velocity.

## 2.2 Azimuthally Anisotropic Flow

Another type of flow that may develop in the course of a nucleus-nucleus collision is azimuthally anisotropic flow. This flow effect is of different origin than radial flow. It is established early on in the reaction and carries out the memory of the collision geometry. It is expected to provide information about the hot and dense state of the collision. Unlike radial flow, the evidence for which is somewhat circumstantial, the azimuthal anisotropies can be measured directly by a variety of methods.

Early studies of emission patterns and event shapes in high multiplicity heavy-ion reactions employed the sphericity method [25, 26], in which the event shape is approximated by a 3-dimensional ellipsoid. From the momenta of all measured particles  $p(\nu)$ ,  $\nu = 1, \dots, N$  in a given collision with multiplicity  $N$ , one constructs the sphericity tensor defined in the center-of-mass frame as

$$S_{ij} = \sum_{\nu=1}^N w(\nu) p_i(\nu) p_j(\nu), \quad (2.10)$$

where  $p_i$  ( $i = 1, 2, 3$ ) is the  $i$ th component of the momentum, and  $w(\nu)$  is the weight factor. Usually the weight is chosen in such a way that composite particles have the same weight per nucleon as the individual nucleons of the composite particle at the same velocity. If the weight  $w(\nu) = 1/2m(\nu)$ , then  $S_{ij}$  is the total kinetic energy in the nonrelativistic limit. The sphericity tensor approximates the event shape by an ellipsoid whose orientation in space and aspect ratios can be calculated by diagonalization. A schematic view of the 3-dimensional event shape and its orientation in coordinate space is depicted in Fig 2.4. The polar angle  $\theta_{flow}$  of the major principal axis to the beam axis is called the flow angle. The sphericity analysis was successfully used for the first observation of collective flow in nuclear collisions [9]. The main limitation of this method, however, is the reduction of all information about the event to the single observable, the flow angle. Also, the flow angle depends on the beam

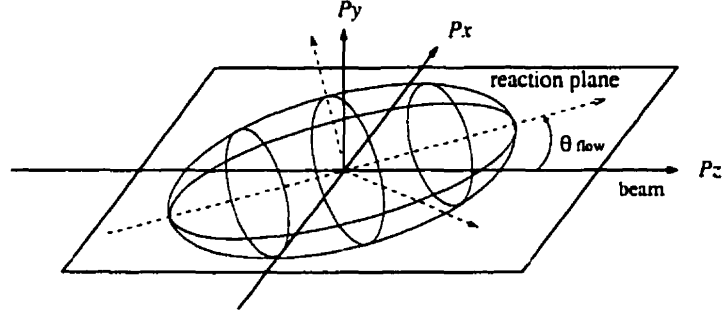


Figure 2.4: Schematic view of the event shape in the center-of-mass frame.

energy:

$$\tan \theta_{flow} \approx \frac{\langle p_x \rangle|_{y=y_{beam}}}{p_{beam}}. \quad (2.11)$$

At ultra-relativistic energies most of the available energy remains in the longitudinal direction. The flow angle becomes very small, independently of whether or not there are collective effects. At the AGS energy,  $\theta_{flow}$  is of the order of  $2.5^\circ$ . This means that at high energies the flow pattern should be studied in the plane transverse to the beam axis.

In the collision of two nuclei, the reaction plane is defined by the beam axis  $\vec{z}$  and the impact parameter vector  $\vec{b}$  (Fig. 2.5). In the transverse direction,  $\phi$  is the azimuthal angle of an outgoing particle, measured with respect to the direction of the impact parameter. The flow is present if particle emission is not isotropic. As it is usually analyzed in the plane transverse to the orientation of the impact parameter, this type of flow is sometimes denoted as transverse flow, which should not be confused with the transverse component of the azimuthally symmetric radial flow described earlier. The azimuthal anisotropy may be detected and quantified by the global transverse momentum analysis [27], or by a generalized method of Fourier expansion [28] of the azimuthal distributions. The essence of these methods is to

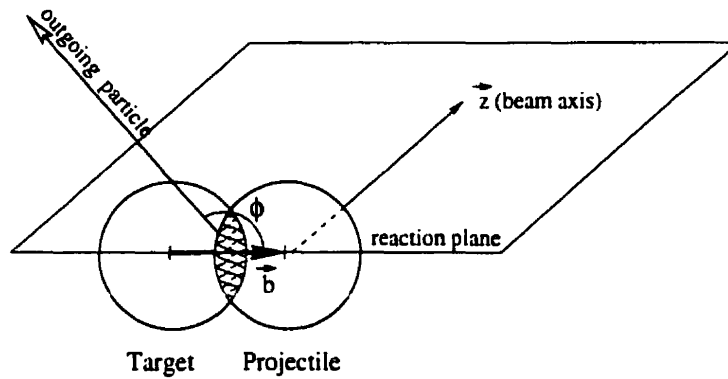


Figure 2.5: View of a collision in the transverse plane.

first estimate the reaction plane. The details of this procedure for the experiment that is a subject of this thesis will be discussed in chapter 5. Below we introduce the observables used in each method and give a brief experimental and theoretical overview of two major effects observed so far, *directed* (or “sideward”) flow and *elliptic* flow.

### 2.2.1 Directed flow

When two nuclei collide at non-zero impact parameter, the high pressure is developed at the impact. The matter will have a tendency to flow in the direction where the pressure gradient is larger. If the system reached a thermal equilibrium, the pressure gradient is steeper in the direction of the impact parameter. As a consequence, the transverse hydrodynamical expansion would generate collective motion pronounced in the direction of the reaction plane (Fig. 2.6). This reflects itself in the transverse momenta, which are also preferentially oriented along the same direction. In the presence of this “sideways” motion, the two-dimensional transverse momentum distribution  $d^2N/dp_x dp_y$ , where  $x$ -direction is taken along the impact parameter vector, is shifted in the direction of the reaction plane (Fig. 2.7a). This directed motion in

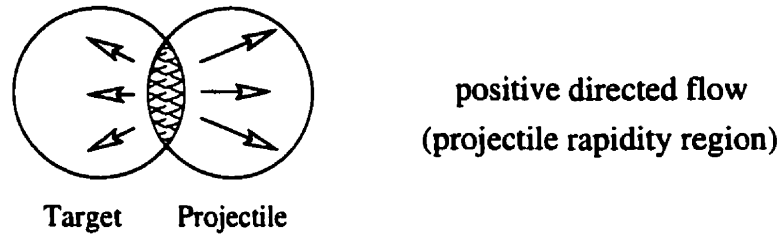
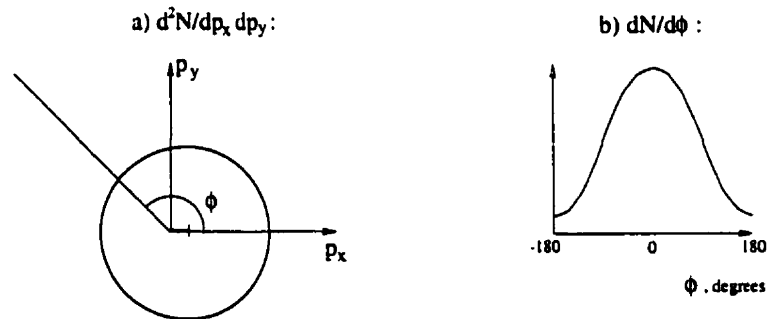


Figure 2.6: Illustration of directed flow.

Figure 2.7:  $d^2N/dp_x dp_y$  and  $dN/d\phi$  distributions in the presence of positive directed flow.

the transverse plane is called *directed flow*.

### Methods and observables

The traditional measure of directed transverse flow is to examine the mean transverse momentum of the particles projected onto the reaction plane [27]:

$$\langle p_x \rangle = \langle p_t \cos \phi \rangle, \quad (2.12)$$

where  $p_t$  is the transverse momentum of the particle, and  $\phi$  is the particle's azimuthal angle taken with respect to the reaction plane orientation. The mean transverse momentum per nucleon in the reaction plane  $\langle p_x/A \rangle$  is studied as a function of rapidity  $y$ . The normalized rapidity  $y_n = (y - y_{cm})/y_{cm}$ , where  $y_{cm}$  is the center-of-mass rapidity,

is usually used to compare the data at different beam energies. For symmetric systems directed flow disappears at  $y_{cm}$  due to the symmetry of collision geometry. When two nuclei collide at non-zero impact parameter, a part of the transverse momentum generated by primary collisions at the one edge of the collision zone would be transported to “spectator particles”. This will eventually appear in the target/projectile fragmentation region shared by many spectator particles as a directed flow. On the other hand, the remaining part of the transverse momentum will be absorbed from the other side of the collision zone. Therefore there is less directed flow in the central rapidity region. For symmetric systems the sign of  $\langle p_x/A \rangle$  changes at  $y_n = 0$ .

The slope of the curve

$$F_y = \left. \frac{\partial[\langle p_x/A \rangle]}{\partial y} \right|_{y=y_{cm}} \quad (2.13)$$

taken in the vicinity of mid-rapidity is scale invariant and usually called flow parameter.  $F_y$  characterizes the transverse velocity imparted to the participants during the collision.

The flow parameter  $F_y$  is a  $p_t$ -integrated observable. In the presence of directed flow, the azimuthal distribution of emitted particles exhibits a cosine-like asymmetry (Fig. 2.7b). A more detailed information on flow can be obtained if the azimuthal anisotropies are described by means of a Fourier expansion [28]. The azimuthal distribution with respect to the reaction plane can be written in a form of Fourier series:

$$\frac{dN}{d\phi} = \frac{\langle N \rangle}{2\pi} \left( 1 + \sum_{n=1}^{\infty} 2v_n \cos n\phi \right). \quad (2.14)$$

The measure of different kinds of anisotropies is provided by the different harmonics:

$$v_n = \langle \cos n\phi \rangle, \quad (2.15)$$

where the brackets denote an average value in a given kinematic window. The dipole ( $n = 1$ ) coefficient quantifies the directed flow. For the particle number distribution,

the coefficient  $v_1 = \langle p_x/p_t \rangle$ . In the projectile rapidity region, directed flow is positive if  $\langle \cos \phi \rangle > 0$ , and negative if  $\langle \cos \phi \rangle < 0$ . Similarly to  $\langle p_x \rangle$ , for symmetric collisions  $v_1(y)$  is an odd function of the center-of-mass rapidity, and signs are therefore reversed in the target rapidity region. Further insights in the study of flow mechanisms is obtained by analyzing the  $p_t$  dependence of the anisotropy.

### Experimental data and model calculations

Since the discovery of “sideward” flow [9, 10], a wealth of experimental results has been obtained. The azimuthally anisotropic flow in nucleus-nucleus collisions at SIS-Bevalac energies has been studied in detail by the Plastic Ball experiments [29], EOS [30], and FOPI [31] collaborations. The E877 experiment was the first to extend flow measurements to energies above the Bevalac [32]. The observation of directed flow at the AGS has stimulated much interest and flow has become a subject of an extensive study in ultra-relativistic nucleus-nucleus collisions. At AGS flow effects are now studied by the E877 [33, 34, 35, 36, 37], E895 [38, 39], and E866/E917 [40] collaborations. The recent measurements of transverse flow at SPS were reported by the NA49 [41] and the WA98 [42, 43] collaborations.

The different properties of azimuthal anisotropies allow for an efficient discrimination between the various theoretical models. The theoretical frameworks that have been developed for the description of nuclear collisions include the semiclassical nonrelativistic nuclear transport models (Boltzmann-Uehling-Uhlenbeck (BUU) [44], Quantum Molecular Dynamics (QMD) [45], cascade codes [46]) and relativistic transport theories (Relativistic BUU [47], A Relativistic Transport (ART) [48, 49], Relativistic Quantum Molecular Dynamics (RQMD) [50, 51]) on the one hand and viscous hydrodynamics models on the other [52, 53, 54]. The cascade codes simulate the nuclear interaction by a succession of stochastic scatterings between particles with measured cross sections. Generally, they cannot reproduce the measured flow values

[55]. In transport codes such as BUU or QMD, propagation between collisions is controlled by the mean field. The mean-field is a functional derivative of the interaction energy for the system, and is directly related to the nuclear equation of state. The models using momentum-dependent mean fields show better consistency with the experimental data. The quantitative description of the EOS, however, is aggravated by a number of not fully understood in-medium effects of hot dense matter, and much effort is needed for theoretical interpretation of all the data.

The magnitude of directed flow depends on the centrality of the collision: it vanishes for central collisions by symmetry, and for very peripheral collisions where compressional effects are low. Below we present some highlights of the experimental results on directed flow observed for semi-central collisions where the effect reaches a maximum and their theoretical interpretations.

*Nucleon and fragment flow.* At the energies up to 12 A·GeV, the mean transverse momentum per nucleon in the reaction plane  $\langle p_x/A \rangle$  plotted as a function of rapidity  $y$  exhibits a typical “S-shaped” dependence. This behaviour is characteristic of the collective transverse-momentum transfer which can be illustrated by the measurements of the EOS collaboration [30]. Figure 2.8 shows the mean in-plane transverse momentum versus normalized rapidity for light fragments in Au+Au collisions at Bevalac energies ranging from 0.25 A·GeV to 1.15 A·GeV. The amplitude of the directed flow signal increases with the beam energy. At the SPS energies, directed flow seems to be concentrated in the fragmentation region, and is almost absent in the central rapidity region [41].

The dependence of directed flow signal on the transverse momentum has been studied by the E877 collaboration [35]. Fig. 2.9 shows the typical measured values of  $v_1(p_t)$  for protons in two rapidity bins. The  $v_1(p_t)$ -dependence of protons is found

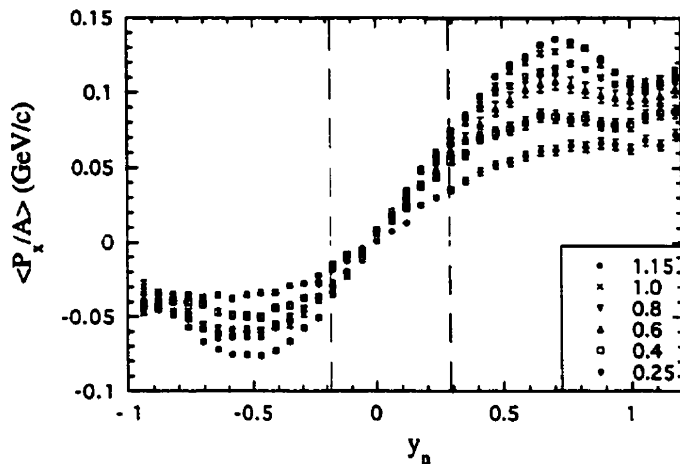


Figure 2.8: Mean in-plane transverse momentum of the fragments ( $p$ ,  $d$ ,  $t$ ,  ${}^3\text{He}$ , and  ${}^4\text{He}$ ) versus normalized rapidity in the reaction Au+Au at Bevalac energies (from [30]).

to increase almost linearly with transverse momentum, contrary to the predictions of the mean-field RQMD model. The directed flow of composite particles shows similar behaviour, with an amplitude increasing with the mass of the fragment both at the Bevalac [56] and AGS [36] energies.

Fig. 2.10 from [57] displays the variation of directed flow of protons with the bombarding energy. The flow parameter  $F_y$  increases as a function of energy up to about 300 A·MeV, where it reaches a maximum. Beyond 400 A·MeV, it starts to decrease, with a steep fall-off to much lower values at the AGS and even lower values at the SPS.

The quantitative evaluation of flow data requires the use of elaborate transport codes. At low and intermediate energies, a BUU transport model taking a momentum and density dependent optical potential well reproduces the data on directed flow in

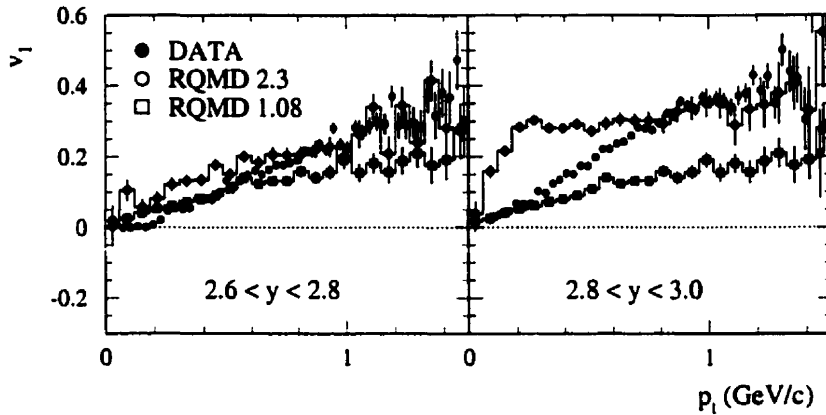


Figure 2.9: Comparison of measured values of  $v_1$  for protons in Au+Au collisions at 10.8 GeV/c in two rapidity bins with those predicted by two versions of the RQMD event generator (from [35]).

symmetric as well as asymmetric nuclear collisions [58]. However, there remain still several difficulties in addressing the question of determination of the nuclear EOS. The comprehensive set of high quality experimental data provides stringent test for microscopic transport models [59].

At the AGS energy it was shown [35] that in a hadronic cascade code, the Relativistic Quantum Molecular Dynamics [50, 51], one can reproduce the overall magnitude of the proton directed flow only if a repulsive mean field between the nucleons is introduced. The model fails, however, to describe the observed near linear  $p_t$  dependence of  $v_1$  signal (Fig. 2.9). This behaviour can be interpreted in the framework of a transversely moving [35] and radially expanding [60] thermal source.

The measurements of directed flow of composite particles provide useful constraints on the theoretical models of their formation. Particularly, it was shown that the volume effects could become significant in the coalescence picture of deuteron production [36].

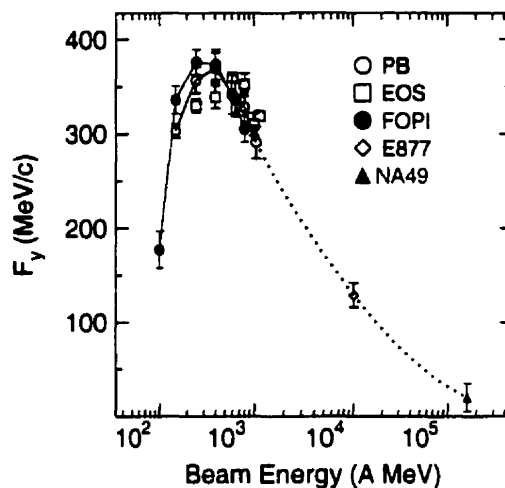


Figure 2.10: Flow parameter of the proton directed flow as a function of the beam kinetic energy per nucleon (from [57]).

In ideal-fluid hydrodynamics, properly scaled flow observables are not expected to depend neither on the size of the system, nor on the incident energy. The variation of directed flow with bombarding energy (Fig. 2.10) is very instructive in search for any possible changes of the EOS or the reaction mechanisms. At low energies (less than 150 A·MeV), the interaction is dominated by the attractive nuclear mean field. At higher energies, individual nucleon-nucleon collisions produce a positive pressure, which deflects the projectile and intermediate rapidity fragments away from the target, resulting in positive directed flow. The overall decrease of the directed flow at energies above 1 A·GeV (see Fig. 2.10) is due to the fact that faster spectators are less easily deflected by the hot, expanding participant matter. However, any drastic changes in the stiffness of the equation of state may be related to the possible phase transition. As one varies the incident energy of a heavy ion collision, the system may reach the softest region in the equation of state and form a long-lived fireball. The hydrodynamical calculations [53, 54] have confirmed that a phase transition in the

nuclear matter equation of state could lead to the appearance of a minimum in the excitation function of the directed flow. It is demonstrated in Fig 2.11 from [61],

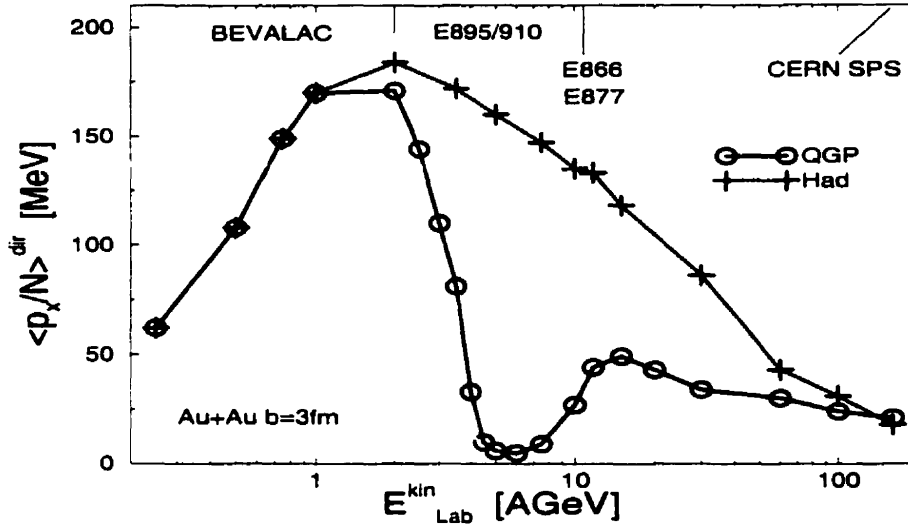


Figure 2.11: Excitation function of the transverse directed flow as calculated from 3+1 dimensional hydrodynamics for Au+Au collisions at impact parameter  $b = 3$  fm. The full line (and the circles) is for an EOS with phase transition to the QGP, the dotted curve (and the crosses) is for a purely hadronic EOS (from [61]).

where the calculations of the transverse directed flow excitation function are plotted for the two possible EOS scenarios. For a purely hadronic equation of state, the directed transverse momentum is monotonically decreasing from SIS to SPS energies. In case of an EOS with phase transition, there is a local minimum in the excitation function around 6 A·GeV. The position of the minimum strongly depends on the model parameters. A quantitative comparison of this model with experimental data is not yet practical as the freeze-out calculation and viscosity effects need to be included in the calculations. On the other hand, A Relativistic Transport (ART) model [48, 49] also predicts the directed transverse flow to be sensitive to the nuclear equation of state. These calculations have demonstrated an importance of transverse

flow measurements in the 2-10 A·GeV energy range.

Recently a detailed experimental program has been completed at the AGS to cover the energy domain from SIS/Bevalac to the AGS. The experiments E866, E917, and E895 are investigating the Au+Au collisions at beam kinetic energies of 2, 4, 6 and 8 GeV. These measurements will provide the necessary constraints on theory.

*Flow of produced particles.* The charged pions produced in heavy-ion reactions in the entire energy range (SIS-SPS) are characterized by a weak negative (opposite to that of protons) directed flow [62, 35, 41]. The AGS data show systematic difference between the flow signals of positive and negative pions in the low  $p_t$  region. The possible interpretations of the observed behavior include pion rescattering on spectator matter, Coulomb interaction with co-moving protons, decays of baryon resonances, and sideward motion of the source.

Due to their large mean free path in nuclear matter, strange particles are predicted to be a sensitive probe of the dense nuclear medium [63]. The measurements from the EOS [64, 65] and FOPI [66] collaborations find that the  $\Lambda$  flow follows the flow of nucleons. The analysis of  $\Lambda$  production at the AGS energy is currently being conducted [67]. In contrast, the  $K^+$ , which are produced in association with the  $\Lambda$ 's, show very little flow. Due to the low production cross section, the data on flow of  $K^-$  are very limited, especially at energies below 2 A·GeV. At the AGS energies, the preliminary results indicate that flow of  $K^-$  is weak and negative, similar to that of  $K^+$  [68]. Further theoretical and experimental work on studies of strange particle production is needed.

The yield of antiprotons is a result of competing processes of initial production and strong absorption in baryon-rich environment. The flow of  $\bar{p}$  is predicted to be of the opposite sign of the nucleon flow [69]. The first preliminary data on directed

flow of antiprotons at the AGS indicate strong azimuthal anisotropy, opposite to the direction of proton flow [68]. A detailed analysis of antiproton flow at the AGS is currently underway [70].

### 2.2.2 Elliptic flow

Directed flow vanishes at  $y_{cm} \approx 0$  because of symmetry reasons. However, due to the large compression achieved in N-N reactions, it is anticipated that strong collective effects should take place at mid-rapidity. Particles emitted in that region originate preferentially from the hot and compressed reaction zone formed by the overlap of projectile and target nuclei during the early stages of nucleus-nucleus collision. The detailed emission pattern is influenced by the geometry of the participant region on one hand, and rescattering and attenuation within the surrounding spectator matter on the other.

Two possible scenarios of particle emission are illustrated in Fig. 2.12. The in-

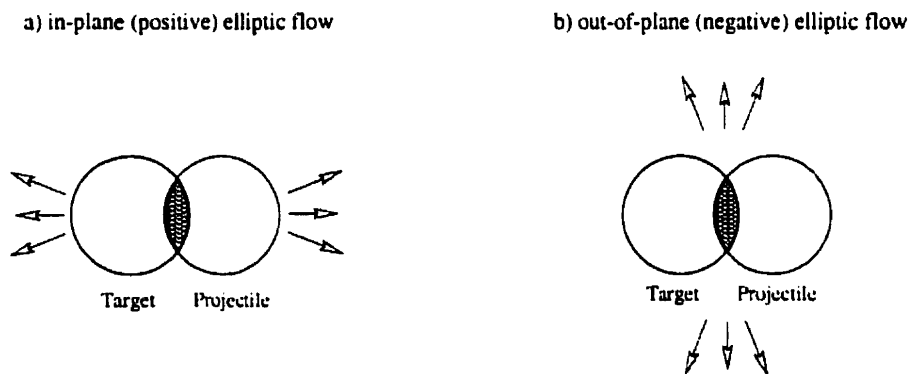


Figure 2.12: Illustration of elliptic flow.

plane elliptic flow is observed when particle emission is enhanced in the reaction plane (Fig. 2.12a). The so-called squeeze-out, or out-of-plane flow corresponds to the particles emitted preferentially in the orthogonal direction to the reaction plane

(Fig. 2.12b). These two effects result in a deviation from a spherical shape of the event and define a second direction of preferred emission.

In the presence of in-plane elliptic flow, the two-dimensional momentum distribution of particles in the transverse plane may be represented by an ellipsoid whose major axis lies in the reaction plane (Fig. 2.13a). The azimuthal distribution of par-

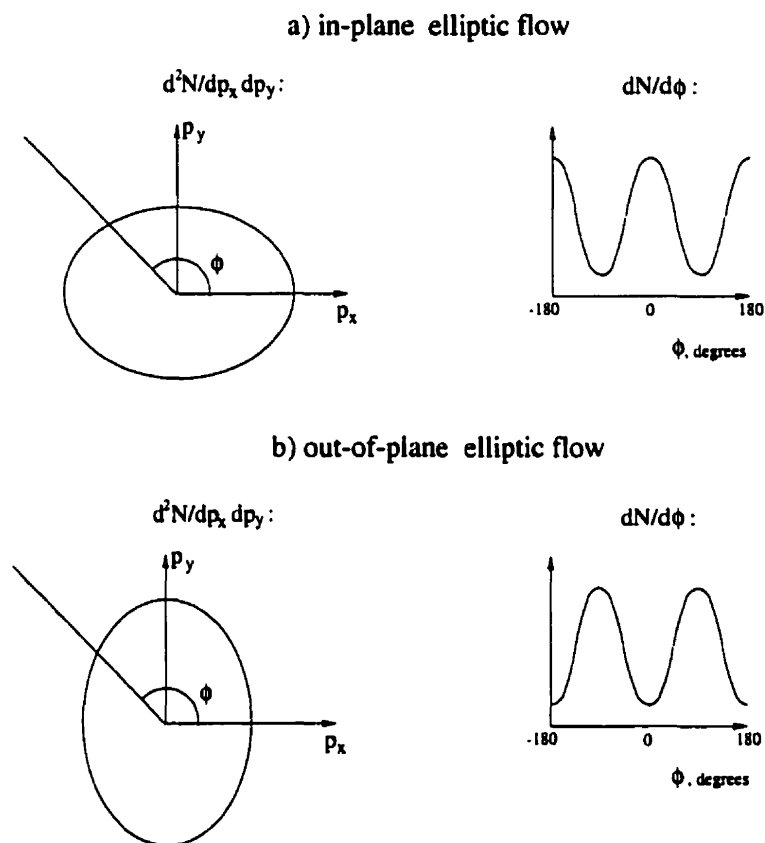


Figure 2.13:  $d^2N/dp_x dp_y$  and  $dN/d\phi$  distributions in the presence of positive (in-plane) and negative (out-of-plane) elliptic flow.

ticles relative to the reaction plane will then behave like a  $\cos 2\phi$  function. If the mechanism of reaction is such that more particles are emitted orthogonally to the reaction plane, then the major axis of the  $d^2N/dp_x dp_y$  distribution is oriented along the same direction, resulting in a  $\frac{\pi}{2}$  phase added to the particle azimuthal distribution

(Fig. 2.13b). These two effects may be quantified by the same observables which have opposite signs for in-plane and out-of-plane flow.

### Methods and observables

The traditional analysis employed for the study of elliptic flow at the Bevalac/SIS energies consists of the fitting the particle azimuthal distributions with the expression

$$N(\phi) \propto 1 + P_1 \cos \phi + P_2 \cos 2\phi, \quad (2.16)$$

where  $\phi$  is the azimuthal angle taken with respect to the reaction plane orientation. The  $P_1 \cos \phi$  term describes the directed flow component in the particle azimuthal distribution and is negligible around mid-rapidity. The parameter  $P_2$  quantifies the strength of the elliptic flow component and is used to construct the ratio of the number of particles at mid-rapidity emitted perpendicular to the reaction plane to the number of particles emitted in the reaction plane:

$$R_N = \frac{N(90^\circ) + N(-90^\circ)}{N(0^\circ) + N(180^\circ)} = \frac{1 - P_2}{1 + P_2}. \quad (2.17)$$

A value for the ratio  $R_N$  larger than unity implies a preferred out-of-plane emission, and following the observation of a squeeze-out effect at the Bevalac is usually called the squeeze-out ratio. In case of in-plane elliptic flow, the ratio  $R_N$  is less than unity.

A similar approach is taken in a generalized Fourier expansion method [28], where the measure of elliptic azimuthal anisotropy is provided by the quadrupole ( $n=2$ ) coefficient in the Fourier decomposition (see equation 2.14) of the particle azimuthal distribution:

$$v_2 = \langle \cos 2\phi \rangle = \langle (p_x/p_t)^2 - (p_y/p_t)^2 \rangle, \quad (2.18)$$

where  $\langle \rangle$  indicates an average over all particles in all events. The coefficient  $v_2$  is positive in case of in-plane elliptic flow, and negative for squeeze-out. Unlike directed

flow, for symmetric systems  $v_2(y)$  is an even function of the center-of-mass rapidity, and elliptic flow has the same sign in the target and projectile rapidity regions.

The advantage of using  $R_N$  and  $v_2$  observables is that they can be analyzed as a function of the transverse momentum. However, one has to be careful in interpretation of obtained results in the region away from mid-rapidity where elliptic flow signal is strongly influenced by the directed flow. This influence is considered by the transverse momentum method [71], in which the flow in-plane and out-of-plane components are determined from the second moments of the transverse momentum components:  $\langle(p_x - \langle p_x \rangle)^2\rangle$  (in-plane), and  $\langle(p_y - \langle p_y \rangle)^2\rangle$  (out-of-plane). The rapidity dependence of the elliptic flow effect is studied by analyzing the ratio of the out-of-plane to in-plane moments. After expanding and dropping the cross terms, the  $p_t$  squeeze-out ratio  $R_{p_t}(y)$  can be written as

$$R_{p_t}(y) = \frac{\langle p_y^2 \rangle - \langle p_y \rangle^2}{\langle p_x^2 \rangle - \langle p_x \rangle^2}. \quad (2.19)$$

The numerator of the above expression is the width of the transverse momentum distribution in the out-of-plane direction, and the denominator is the width of the in-plane distribution corrected for the mean  $p_x$  values caused by the directed flow.

The  $R_{p_t}(y)$  ratio is a  $p_t$ -integrated observable. In chapter 5, we introduce an approach which combines aspects of the above described methods and which is useful in decoupling the influence of directed flow signal on the elliptic flow observables.

### Experimental data and model calculations

The experimental evidence for elliptic flow has been obtained first by the Diogéne Collaboration in Ne-induced reactions at 800 A·MeV [72]. They observed an out-of-plane peak in azimuthal distribution of particles around the beam axis at mid-rapidity. The systematic studies of this squeeze-out effect in Au+Au reactions have been performed by the Plastic Ball Collaboration [73, 71]. The effect has been found

to be strongest for reactions at intermediate impact parameters and most pronounced at mid-rapidity.

The transition from out-of-plane to in-plane elliptic flow has been predicted to occur at relativistic energies [74, 75], and has been first observed at the AGS [34, 35], and then confirmed at the SPS [41, 76].

The mechanism of elliptic flow of nucleons is different than that of produced particles (mainly pions and kaons). Below we will discuss some of the existing data and compare them with the theoretical calculations.

*Flow of nucleons.* At Bevalac/SIS energies, elliptic flow of nucleons and fragments has been studied in detail by the Plastic Ball [71], FOPI [77] and KAOS [78] collaborations. In this energy domain the elliptic flow is always negative (out-of-plane). The magnitude of elliptic flow is found to be larger for heavier systems, and also larger for fragments than for protons. Typical azimuthal distributions of protons, deuterons and tritons measured in Bi+Bi collisions at 0.4 A·GeV are presented in Fig. 2.14 (from [78]). The distributions show maxima around  $\pm 90^\circ$  with respect to the event plane. This pattern demonstrates the preferred emission of particles out of the reaction plane.

At the ultra-relativistic energies, the first indication of elliptic flow has been obtained by the E877 experiment [32]. Contrary to the observations at lower energies, the elliptic flow has been found to be in the reaction plane [34, 35]. Even stronger in-plane flow has been recently measured at the SPS by the WA98 [76] and NA49 [41] experiments.

Fig. 2.15 from [57] shows the variation of the quadrupole coefficient in the Fourier decomposition of nucleon azimuthal distribution with the bombarding energy. At energies below 100 A·MeV the elliptic flow is positive. At intermediate energies the

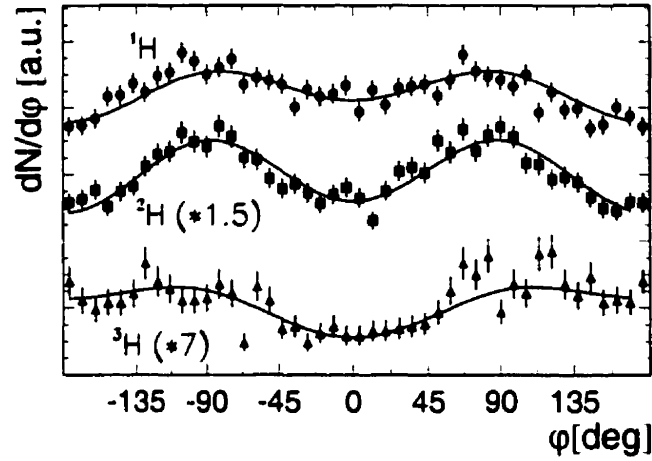


Figure 2.14: Typical  $dN/d\phi$  distributions for protons, deuterons and tritons measured in Bi+Bi collisions at 0.4 A·GeV (from [78]).

elliptic flow changes sign from in-plane to out-of-plane, and reaches the maximum squeeze-out at around 400 A·MeV. At higher energies out-of-plane emission gets weaker, and at energies between 2-8 A·GeV elliptic flow crosses zero again. Positive in-plane elliptic flow of the order of 2% is observed at 10 A·GeV, and it increases up to 6% at 150 A·GeV.

Like directed flow, the elliptic flow is a collective effect and most of the hydrodynamic or microscopic models that include some form of equation of state predict this mechanism of particle emission.

The dependence of the elliptic flow on beam energy may be interpreted as the following. At lower beam energies it reflects the energy dependence of the nucleon-nucleon interaction. At very low energies the interaction is attractive, and the projectile and target form a rotating system that emits particles in the reaction plane. At higher energies, the nucleon-nucleon collisions start to dominate over mean field

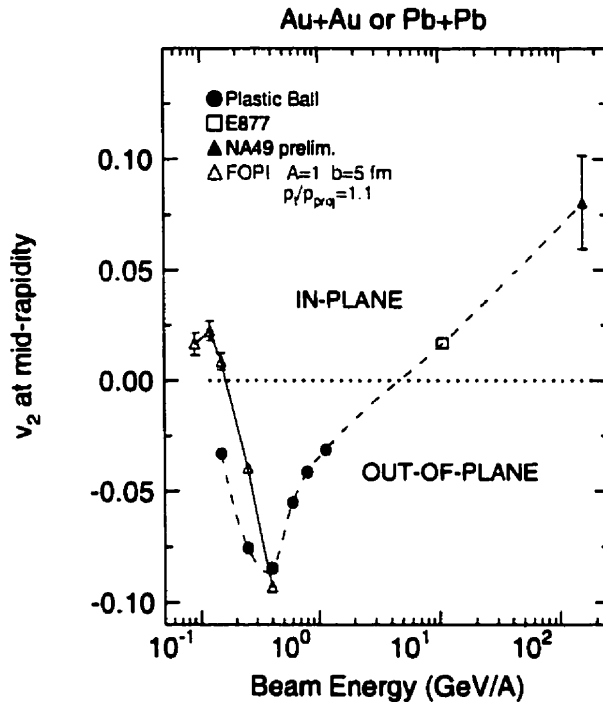


Figure 2.15: Energy dependence from SIS to SPS energies of the elliptic flow (from [57]).

effects and generate a positive pressure. The participant nucleons compressed in the central region are blocked by the cold spectator matter present in the reaction plane, producing a squeeze-out effect. At AGS energies, the emission pattern is a result of competition between the two effects: the initial shadowing of participant hadrons by the spectator nucleons, and the collective flow related to the pressure build-up. The former leads to negative elliptic flow. The latter is developed due to the almond-shaped geometry of the participant region. A larger surface area exposed in the direction of the reaction plane favors in-plane preferential emission and hence positive elliptic flow. So the magnitude and sign of the elliptic flow depend on the pressure built up in the compression stage and the time needed for removal of

spectators from the interaction region. At relativistic energies the crossing time of projectile and target shrinks with the Lorentz factor  $\gamma$ , and the compression related elliptic flow appears to dominate.

The elliptic flow has already been shown to be very sensitive to the pressure at maximum compression [74, 79]. The practical viability of elliptic flow as a probe for the EOS and the phase transition has been investigated by means of a relativistic transport model [80]. It has been shown that the transition energy at which the elliptic flow changes signs is strongly dependent on the parameters of the EOS. The excitation function of elliptic flow also exhibits characteristic signatures which could signal the onset of a phase transition to the QGP. Fig. 2.16 from [80] shows that the slope of the excitation function of the elliptic flow amplitude depends strongly on the stiffness of the EOS. The experimental data in that energy domain will soon be available.

*Flow of pions and kaons.* The azimuthal anisotropies in distributions of produced particles, mainly mesons, are less dynamical in origin than those of nucleons and fragments. Transverse flow of pions and kaons is determined mainly by re-scatterings and absorption effects rather than caused by pressure gradients. The first observation of enhanced emission of pions in the direction perpendicular to the reaction plane was reported at SIS-GSI [81]. The out-of-plane/in-plane ratio  $R_N$  (see equation 2.8) for  $\pi^+$  is presented in Fig. 2.17 as a function of the transverse momentum for semicentral Au+Au collisions at 1 GeV/nucleon. The value of  $R_N$  is larger than unity for all transverse momenta and shows an approximate linear dependence on  $p_t$ . The  $\pi^-$  data yield similar results. One of the possible interpretations of the observed anisotropy is shadowing of pion emission in the event plane by the spectator fragments.

The previous analysis of pion elliptic flow at the AGS energy has not been able

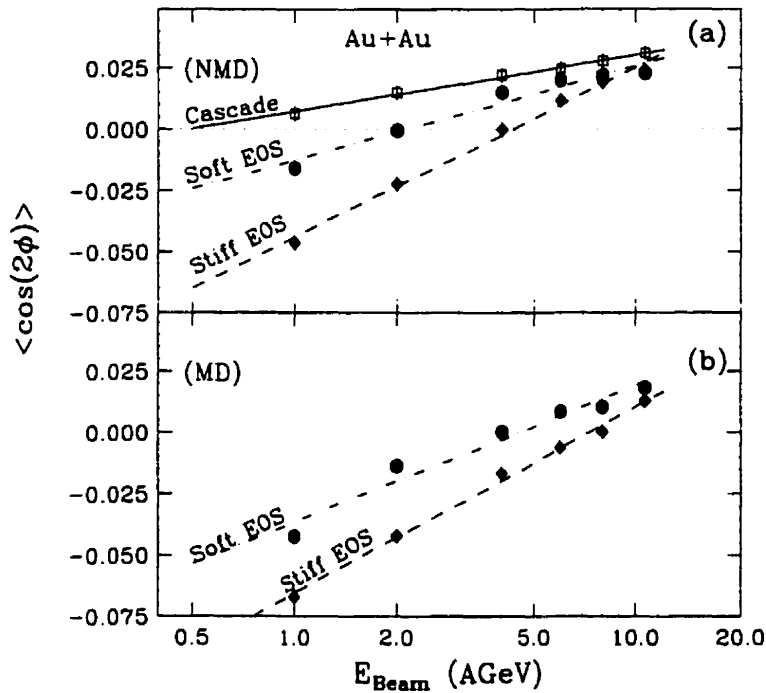


Figure 2.16: Calculated elliptic flow excitation functions for Au + Au reactions. Panels (a) and (b) show, respectively, the functions obtained without (NMD) and with (MD) the momentum dependent forces. (from [80]).

to reveal an existence of any significant effect [35]. With high statistics data available from the last running period of the E877 experiment, we will examine the pion emission pattern in chapter 7. The elliptic flow of pions at the SPS was found to be positive, i.e. of the opposite sign to the Bevalac data. The signal is fairly independent of rapidity but rises with  $p_t$  [41].

The production of strange mesons in relativistic nucleus-nucleus collisions allows the investigation of the effects of mean-field potentials. The  $K^+$  mean free path for rescattering in nuclear matter is substantially longer than the one of pions. The recent results from the KAOS collaboration [82] have shown the existence of negative elliptic flow of  $K^+$  mesons at the energy of 1 A-GeV. The pronounced  $K^+$  out-of-

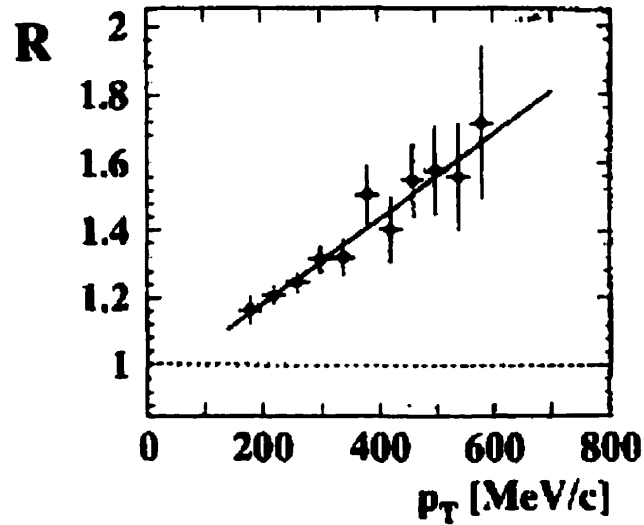


Figure 2.17: Out-of-plane/in-plane ratio for  $\pi^+$  as a function of the transverse momentum for semicentral Au+Au collisions at 1 GeV/nucleon (from [81]).

plane emission at mid-rapidity is reproduced by the RBUU calculation if an additional repulsive in-medium  $K^+N$  potential is taken into account [83].

## 2.3 Summary

Nuclear collisions have been a subject of scientific research already for two decades. Collective effects opened up a way to study the bulk properties of nuclear matter far from stability. Theoretical predictions were confirmed that nuclear matter will exhibit hydrodynamic behaviour if compressed to several times nuclear ground state density and if heated to temperatures in excess of few tens of MeV. Azimuthal anisotropies in particle production, particularly yields of strange and antimatter with respect to the reaction plane, provide a tool for exploring the possible modifications of hadron properties in dense nuclear medium.

## Chapter 3

# E877 experiment at the AGS

The experimental data discussed in this thesis were obtained during the winter 1995 running period of the E877 experiment at the Alternating Gradient Synchrotron (AGS) of the Brookhaven National Laboratory (BNL), Long Island, NY. The E877 experimental setup is presented in Fig 3.1. The beam of  $^{197}\text{Au}$  nuclei is accelerated to momenta of 11.5 A·GeV/c and collides with a 980 mg/cm<sup>2</sup> thick Au target. The projectile trajectory is determined by beam definition detectors. The target is surrounded by a  $4\pi$  calorimetry measuring the energy of particles leaving the interaction region. Charged particles emitted in forward direction are analyzed by a magnetic spectrometer. Below we present a brief description of each component of the apparatus.

### 3.1 Beam Definition Detectors

The group of beam definition detectors is shown on the inset of Fig 3.1. It consists of four beam counters (S1-S4) and two beam vertex detectors (BVER1-BVER2). The beam counters are used to define a valid beam trigger. The trajectory of each beam particle is measured by the BVER detectors. Both the beam counters and vertex

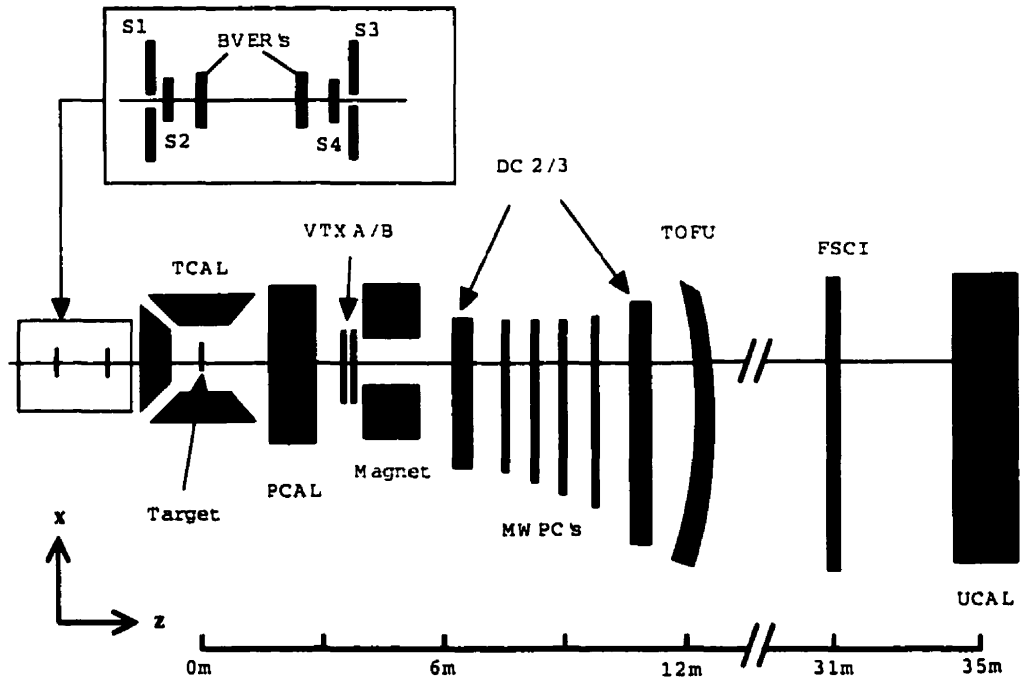


Figure 3.1: E877 experimental setup.

detectors have the ability to reject the events with two beam particles arriving at the target at the same time (double beam events).

### 3.1.1 Beam counters

The beam scintillator counters (BSCIs) are schematically shown in Fig 3.2. The S1 and S3 counters are comprised of 15 cm diameter 0.635 cm thick plastic scintillator disks located inside the beam line vacuum and viewed through lucite light guides by four photomultiplier tubes. The hole in S1 is 1.5 cm diameter and the hole in S3 is 0.6 cm diameter. These two counters, located 4.25 m apart, serve to define the beam in both position and angle, and to veto particles outside the central region of the beam, as well as any upstream interactions. The S2 and S4 counters are used to

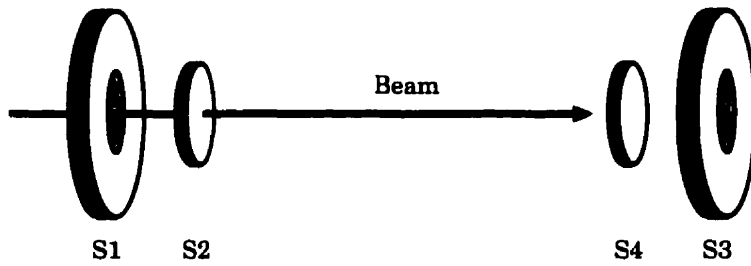


Figure 3.2: Beam scintillator counters.

positively identify beam particles and to produce the start time signal. A valid beam trigger is defined as the coincidence  $\overline{S1} \cdot S2 \cdot \overline{S3} \cdot S4$ .

In 1995, a new set of beam Cherenkov counters were installed in place of the S2 and S4 scintillators for the 1995 run. The mechanical and optical arrangement of one of the beam Cherenkov packages is shown in Fig. 3.3. These counters consist of a

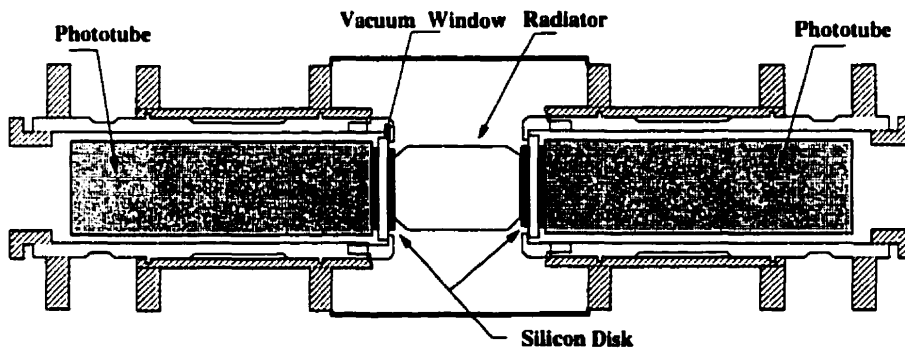


Figure 3.3: Cherenkov beam counter.

thin quartz radiator, 0.2 mm thick and 6.35 cm x 7.62 cm in transverse dimension. The radiators are mounted in blackened lucite supports and placed in the beam inside the vacuum. Cherenkov light produced in the quartz is carried by multiple internal reflections to the edge of the radiator where it is coupled to a 6.35 cm diameter by 0.635 cm thick quartz vacuum window using a UV transmitting silicon disk. The Hamamatsu R2083 phototubes are used to detect the light and are coupled

to the outside of the quartz vacuum window using similar silicon disks. The signal produced in these counters has a very fast rise time because of the Cherenkov light, and has better energy resolution than the beam scintillators due to the better response uniformity. In addition, no degradation of the pulse height response from the quartz radiators was observed for the entire run of the experiment, which accumulated a total of  $4 \times 10^{10}$  beam particles over a period of more than two months [84].

### 3.1.2 Beam vertex detectors

The beam vertex (BVER) detector system consists of the two high precision two-dimensional detectors located at 2.8 m and 5.8 m upstream of the target. The  $300 \mu\text{m}$  thick micro-strip silicon detectors with an active area of  $19.2 \times 19.2 \text{ mm}^2$  etched on 7.6 cm Si wafers are used to measure the angle of the beam particle and its position at the target.

For the 1995 run, each detector was upgraded from the single-sided silicon wafers with an one-dimensional pitch of  $50 \mu\text{m}$  to the double-sided wafers with a  $200 \mu\text{m}$  pitch in both the  $x$  and  $y$  axes. This allowed the measurement of the coordinates of beam particles in two dimensions and infer their position at the target with  $300 \mu\text{m}$  position and  $60 \mu\text{rad}$  angular resolution. The tracking efficiency throughout the run was better than 90%. More details on the BVERs upgrade and performance can be found in [70].

## 3.2 Calorimeters

The E877 apparatus also includes three calorimeters: the target calorimeter (TCAL), the participant calorimeter (PCAL), and the uranium calorimeter (UCAL). The first two detectors are located in the target region and used to provide the global event

characteristics, such as the centrality of the event and orientation of the reaction plane. The UCAL calorimeter is the last detector downstream positioned about 35 meters away from the target and used to measure the energy of forward particles. Combined together, the three calorimeters cover almost the full solid angle with respect to the target.

### 3.2.1 Target calorimeter

The target calorimeter (TCAL) is an electromagnetic calorimeter sensitive to charged and neutral particles and gamma rays. It consists of 832 NaI scintillating crystals arranged in a quasi-projective geometry with respect to the target. Fig. 3.4 shows the geometry of the detector. Four walls of  $3.6 \text{ cm} \times 3.6 \text{ cm} \times 13.8 \text{ cm}$  crystals are

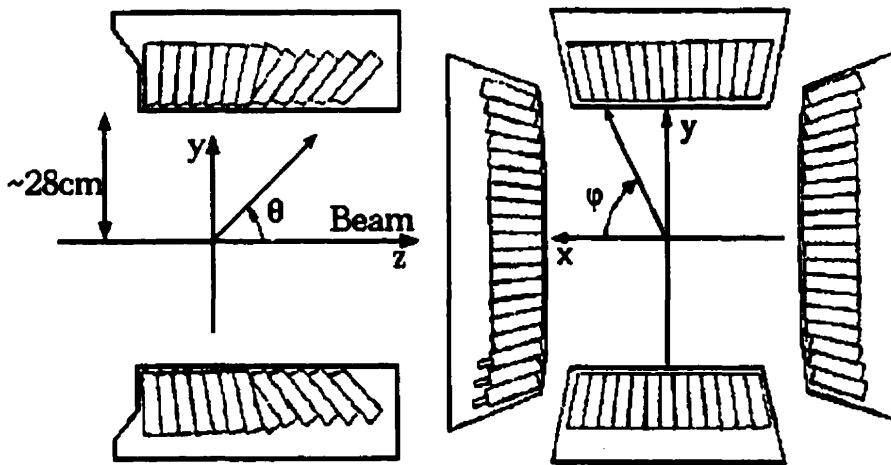


Figure 3.4: Side and end views of the target calorimeter.

placed parallel to the beam direction at approximately 28 cm from the target. The depth of each wall is 5.3 radiation lengths (0.34 hadronic interaction lengths). The signals from the crystals are read out by vacuum photodiodes. The TCAL provides a transverse energy measurement over the full  $2\pi$  azimuthal angle and in the polar

angle region of  $48^\circ < \theta < 135^\circ$ , which corresponds to the pseudorapidity coverage of  $-0.5 < \eta < 0.8$ . A full description of the target calorimeter can be found in [85].

### 3.2.2 Participant calorimeter

The participant calorimeter (PCAL) is a lead/iron/scintillator sampling calorimeter with a depth of 4 nuclear interaction lengths. It consists of four identical quadrants segmented into eight radial and sixteen azimuthal elements and arranged to maintain an azimuthal symmetry around a central opening (Fig. 3.5). Longitudinally the PCAL is divided into two electromagnetic (EM1 and EM2) and two hadronic (HAD1 and HAD2) segments. There are a total of 512 cells in the whole detector. The scintillator plates are read out using wave length shifting optical fibers connected to the photomultipliers. The PCAL measures energy flow in the forward direction and has a complete azimuthal coverage and  $1^\circ < \theta < 47^\circ$  polar angle or  $0.83 < \eta < 4.7$  pseudorapidity coverage. More details about the PCAL can be found in [86, 87].

### 3.2.3 Uranium calorimeter

Similar to PCAL, the uranium calorimeter is a sampling calorimeter with uranium and iron absorber plates. The uranium is used to compensate the energy deposition between hadronic and electromagnetic interactions via the fission. The UCAL consists of 20 modules located at 35 meters downstream of the target. Each module is segmented into 24 10 cm x 10 cm towers. The angular coverage of the UCAL is  $-5.2^\circ < \theta < 1.3^\circ$  horizontally and  $-0.98^\circ < \theta < 0.98^\circ$  vertically. The full description of the detector is given in [88]. The purpose of this device is to measure the energy of the forward particles, especially neutrons. It has not been used in our analysis.

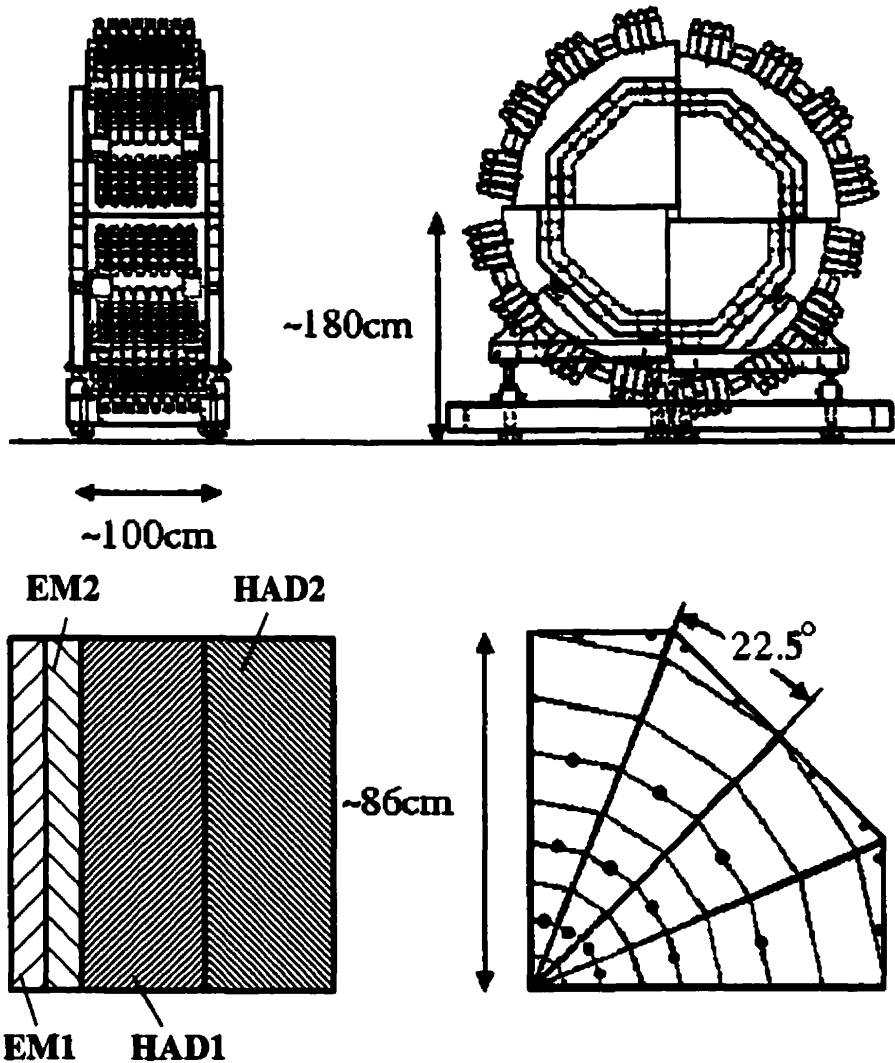


Figure 3.5: Participant calorimeter in various views.

### 3.3 Forward Spectrometer

The charged particles emitted in the forward direction and passing through the collimator are analyzed by a high-resolution forward magnetic spectrometer. The spectrometer is designed to identify particles and to measure their momenta. The first two elements of the spectrometer are the collimator and analyzing magnet.

The spectrometer acceptance is determined by a variable size collimator which is placed at the center of the participant calorimeter and made of four steel plates shaped to project back to the target. The vertical opening is adjusted to match the particle multiplicity with the capabilities of the tracking system. For the Au+Au collisions, the collimator was set to have a vertical (in  $y-z$  plane) opening of  $-21 < \theta < 21$  mrad and a fixed horizontal (in  $x-z$  plane) opening of  $-115 < \theta < 14$  mrad.

The analyzing dipole magnet is positioned 3 meters downstream of the target. The magnet is capable of generating a maximum field of 2.2 T and has an effective length of 1.045 m. The field direction is perpendicular to the spectrometer plane and can be inverted to favor negatively or positively charged particles. In the 1995 run, a field value of -0.3353 T was used which provided a better acceptance for negatively charged particles.

The charge particle identification proceeds by mass reconstruction based on simultaneous measurement of particle momentum and time-of-flight. The forward spectrometer consists of two drift chambers, four multi-wire proportional chambers, two time-of-flight hodoscopes and two pad chamber detectors. Below a brief description of each component of the spectrometer is given.

### 3.3.1 Drift chambers

The momentum of each particle is measured using two high-resolution drift chambers, DC2 and DC3. The detectors are located at 5.4 m and 11.5 m downstream from the target. Each chamber is composed of six planes of alternating anode and field wires separated by an aluminized mylar cathode. A schematic layout of the drift chambers is shown in Fig. 3.6. The distance between anode wires is 6.35 mm in DC2 and 12.7 mm in DC3. This provides a measurement of the  $x$ -coordinate (in the bending plane of the magnet) of the track, with a resolution of 200  $\mu\text{m}$  (500  $\mu\text{m}$ ) for DC2 (DC3).

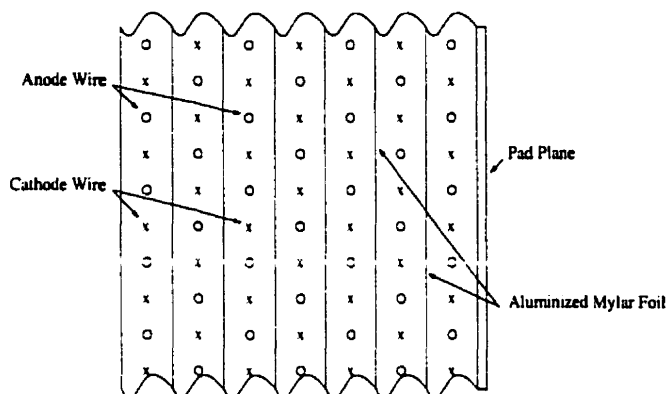


Figure 3.6: Layout of the drift chambers.

The cathode plane of each chamber is segmented into chevron-shaped pads running along the wire direction (perpendicular to the bending plane of the magnet). The pad plane is divided according to the expected particle multiplicity into several density regions. The  $y$ -coordinate of the track is reconstructed with a resolution depending on the pad density region: 2-15 mm in DC2 and 4-36 mm in DC3. For more detailed information regarding the drift chambers see [89].

### 3.3.2 Multi-wire proportional chambers

The tracking ability of the drift chambers is aided by four multi-wire proportional chambers (MWPCs) placed between DC2 and DC3. These detectors are used to improve the pattern recognition of the tracking system in the high multiplicity environment of Au+Au collisions. Each MWPC consists of a number of vertically strung anode wires spaced 5.08 mm apart. The signals from the wires of all four MWPCs provide a bit pattern that is used for an offline track confirmation. A detailed description of the MWPCs construction and operation can be found in [90].

### 3.3.3 Time-of-flight hodoscope

A high granularity time-of-flight hodoscope (TOFU) is used to measure the time-of-flight of the particle. It is installed immediately behind the last tracking chamber (DC3) of the spectrometer in order to increase the efficiency for detecting low-energy kaons before they decay in flight. A sketch of the complete scintillator hodoscope and its mounting structure is shown in Fig. 3.7. The hodoscope wall is comprised

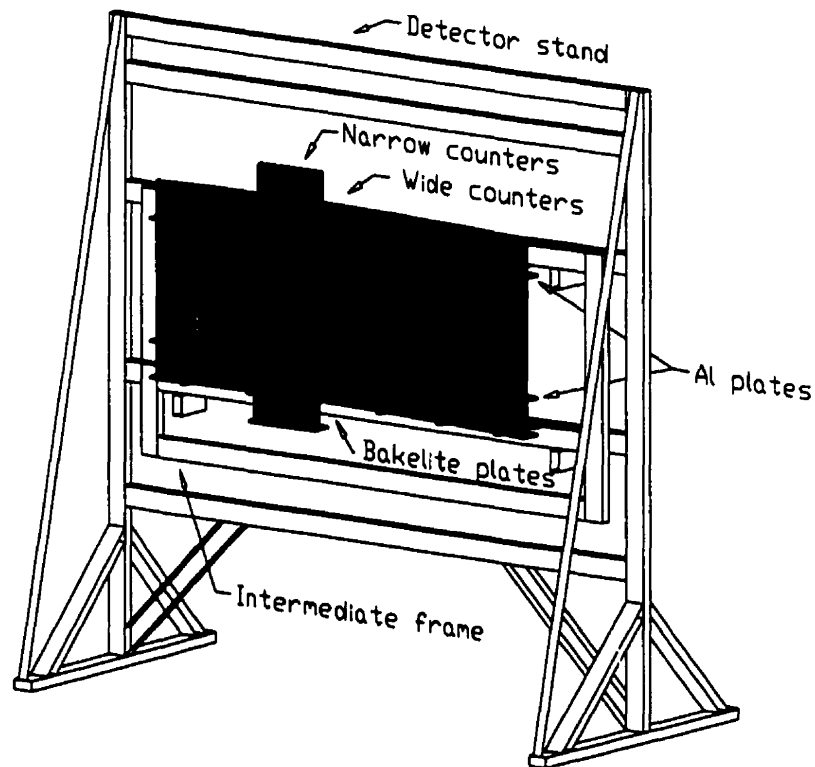


Figure 3.7: Time-of-flight hodoscope wall.

of about 150 scintillator counters, each viewed by two photomultipliers. It has two density regions accommodating a higher occupancy of tracks near the beam. The high density section around the beam is made of counters with a width of 10 mm, and the other is assembled with wider (17 mm) counters. The total sensitive area of the hodoscope wall is  $1.4 \text{ m}^2$ . The overall time-of-flight resolution is about 85 ps.

Besides the measurement of particle time-of-flight, a complementary vertical position of the track is obtained by measuring the time difference between the photomultiplier signals at both ends of the counter with a resolution of 1.8 cm. The particle energy loss in the scintillators given by the photomultiplier pulse height measurements is used to determine the charge of the particle. A complete description of the design, assembly and performance of the time-of-flight hodoscope is given in [91, 84].

### 3.3.4 Vertex detectors

For the 1995 run, two identical highly segmented pad cathode chambers were instrumented and placed at 2 m and 2.25 m downstream of the target, just in front of the spectrometer magnet. They provide a precise measurement of the  $x$ -coordinate of the track before it is bent by the magnetic field. An addition of this upstream tracking information allows to reconstruct the vertex of  $\Lambda$  hyperon decays and improve the signal-to-background ratios for identification of rare particles, such as kaons ( $K^+$ ,  $K^-$ ) and antiprotons  $\bar{p}$ .

The vertex detectors (VTXA/B) are multi-wire proportional chambers with interpolating chevron shaped pad readout. A cross section of the pad chamber assembly is shown in Fig. 3.8. It consists of a wire plane with anode and field wires sandwiched

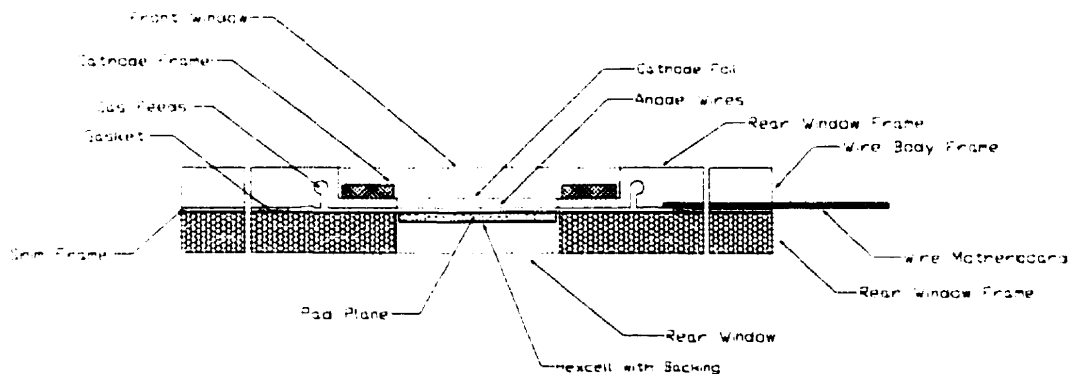


Figure 3.8: Cross section of the vertex pad chamber assembly.

between two cathode planes, one with chevron shaped pads. The signals from each pad are read out by an electronics chain consisting of a preamplifier, a transformer, a shaping amplifier, and a FASTBUS ADC. The position along the wire direction is measured using the geometric charge division method, in which the relative value of the induced charges on the pads determines the avalanche location. The position resolution along the wire direction achieved with 1.75 mm long pads is about 300  $\mu\text{m}$ . The  $y$ -coordinate is determined by the wire spacing (6 mm). A description of the design, implementation and performance of the vertex detectors can be found in [92].

### 3.3.5 Forward scintillators

The last component of the E877 magnetic spectrometer is the forward scintillator hodoscope wall. It consists of 39 plastic scintillators, each 10 cm wide, placed vertically at about 31 meters downstream from the target. The time-of-flight resolution of the forward scintillators is about 350 ps. The measurements from this detector have not been used in this analysis.

# Chapter 4

## Data Reduction and Calibration

### 4.1 Overview

The data presented here were taken in the winter of 1995. The running period lasted for over two months, during which about 80 millions Au+Au events were recorded onto more than 400 8-mm magnetic data tapes. The total amount of collected data exceeds 1.6 Tb. This enormous volume of information is a result of the impossibility to conduct a physics analysis of the event during the data taking, as it requires much more time that is provided by the online recording rate. The common procedure is thus to store for each event the raw data (ADC and TDC counts, bit patterns, etc.) for all the channels of every detector. This raw information is then analyzed offline and reduced to a manageable set of necessary variables. The channels that contain no data are removed, ADC and TDC counts are calibrated and interpreted in terms of pulse height and time, which are subsequently translated into useful quantities, i.e. energy measured in the calorimeters, coordinates measured by the tracking detectors, time-of-flight measured by the scintillator hodoscopes. The last step of this offline data reduction procedure is to reconstruct the physics observables of the event, such

as centrality, reaction plane orientation, particle species and their momenta. Below we present the steps necessary to obtain a set of data which then will be used in the physics analysis.

## 4.2 Calibration

In this section we briefly go over procedures necessary for calibration of the principle detectors used in the data analysis: the participant calorimeter, the drift chambers, and the time-of-flight hodoscope.

A common procedure for all the detectors utilizing the analog-to-digital converters (ADCs) is the pedestal subtraction. The values measured by each ADC channel in the absence of the signal are called pedestals, and need to be subtracted to obtain the correct pulse height. The pedestals collected during the run were fitted by a Gaussian and subsequently subtracted during the data reduction stage.

### 4.2.1 Participant calorimeter

The energy deposited in each cell of the calorimeter is measured by the pulse height in the phototubes attached to each scintillator. Since gain variations of the individual phototubes will result in different readings for the same energy, it is very important to keep those variations to a minimum. During the run, the gain for each phototube was adjusted by varying its high voltage. The calibration was done using a 2.4 mCi  $^{60}\text{Co}$   $\gamma$ -ray source, the position of which could be varied to expose different sections of the calorimeter. During a calibration run, the source was moved by a motor to pass near each section of the calorimeter. The readings of the pulse height in the photomultipliers were then analyzed, and the high voltage was adjusted if the signal did not match a pre-set value. The short term drift of the phototube gains was taken

into account during the production of the reduced data set. A so-called (n,n+1) procedure was employed, during which the average ADC count from the  $n^{\text{th}}$  run was used to calculate the gain factor for the subsequent ( $n^{\text{th}}+1$ ) run. The energy calibration of the PCAL was done later offline. The method utilized a Monte Carlo simulation of the PCAL response [93]. The details of this procedure can be found in [94].

### 4.2.2 Drift chambers

The  $x$ -position of the charged particles traversing the drift chamber is determined by the drift time measurement. A charged particle ionizes gas molecules along its path. The ionization electrons are drifted with constant velocity through the gas volume and amplified at the sense wires in avalanches. By measuring the drift time we can deduce the particle's coordinate with respect to the sense wire.

Due to the varying time delays in electronics and cables, all the channels of the chamber had slightly different time offsets (see Fig. 4.1, left panel). To achieve the best possible resolution, we aligned the start times of all the wires. The time offsets were calculated by fitting a Gaussian to the time spectrum in each channel. The measured times on each wire were then aligned to the mean drift time measured on the first wire. This procedure was done for each of the six wire planes in DC2 and DC3. The time offsets of one of the planes of DC2 and DC3 before and after this calibration are presented in Fig. 4.1.

Due to non-uniform electric field, the drift velocity is not constant for the regions close to and far from the sense wire. This results in non-linearity in time-to-distance relationship, which can be corrected by introducing a weight function for the time distribution  $dN/dt$ :

$$w(t) = \frac{\int_0^{t_{\text{meas}}} \frac{dN}{dt'} dt'}{\int_0^{t_{\text{max}}} \frac{dN}{dt'} dt'}, \quad (4.1)$$

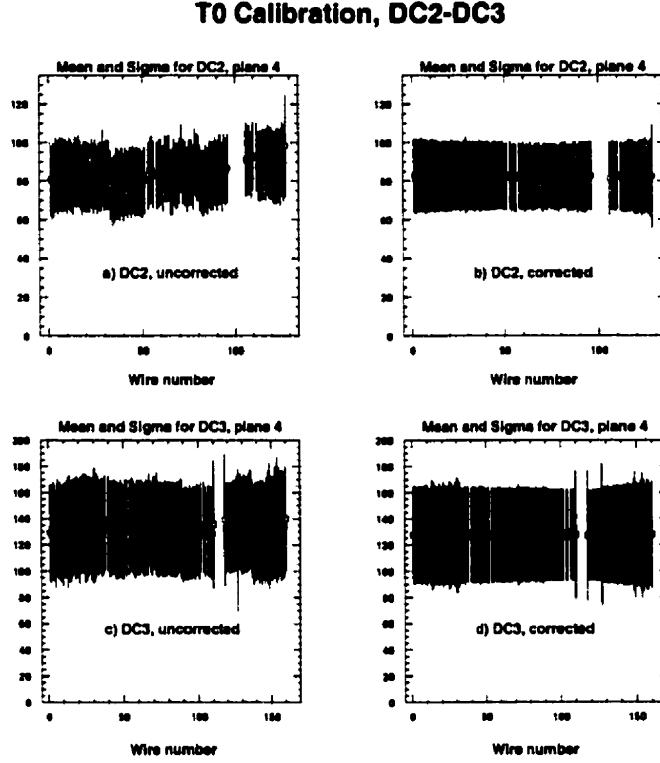


Figure 4.1: Time offsets in nanoseconds of each wire in one of the DC2 and DC3 planes before (left panel) and after (right panel) calibration.

where  $t_{meas}$  is the measured time and  $t_{max}$  is the largest measured time. The drift distance to the sense wire is then determined by:

$$d(t) = \frac{x_{cell}}{2} w(t), \quad (4.2)$$

where  $x_{cell}$  is the drift cell size (3175  $\mu\text{m}$  for DC2 and 6350  $\mu\text{m}$  for DC3). The introduction of the weight function  $w(t)$  results in a linear relationship between the measured time and distance and significantly improves the position resolution. It was calculated for each plane of the drift chamber, with the (n,n+1) procedure employed for calibration of subsequent runs. After completing the calibration, the average

$x$ -position resolution over six planes is  $\sim 250\mu\text{m}$  for DC2 and  $\sim 500\mu\text{m}$  for DC3.

The pad plane of the drift chambers is used to measure the  $y$ -coordinate of the track. The movement of the electrons and positive ions induces charge on the cathode plane which is segmented into chevron-shaped pads. The  $y$ -position of the particle is inferred from the centroid of the charge distribution divided between the two pads:

$$y = \frac{y_1 Q_1 + y_2 Q_2}{Q_1 + Q_2}, \quad (4.3)$$

where  $y_1, y_2$  are the  $y$ -coordinates of the two pads, and  $Q_1, Q_2$  are the charges deposited on each pad. A test pulser was used to calibrate the gain of each pad channel. The integrated  $y$ -position spectra were linearized by a weight function similar to the one described above.

### 4.2.3 Time-of-flight hodoscope

To achieve the best possible resolution, the time-of-flight system needs to be carefully calibrated. A number of different factors were taken into account. A complete description of the system and discussion of its performance can be found in [91, 84, 70]. Here we briefly go over main steps in the robust calibration procedure.

#### Pulse height measurement

Prior to assembling the individual counters, the relative gain and time resolution of each photomultiplier were measured. This was done using light pulses from an  $\text{N}_2$  dye laser that were simultaneously sent through optical fibers to the tested and reference photomultipliers. The photomultipliers were paired according to their time resolution before being glued to the scintillators.

The initial amount of light emitted by the scintillator is attenuated approximately exponentially with distance as it travels toward the photomultipliers. Thus, the total

signal amplitude  $\Delta E$ , or energy loss of a particle traversing the counter, can be expressed as:

$$\Delta E = c^j \cdot \sqrt{(ph_{\text{top}} \cdot ph_{\text{bottom}})} \quad (4.4)$$

where  $c^j$  is a pulse height normalization constant adjusted for each counter so that a  $Z=1$  minimum ionizing peak has a  $\Delta E=1.0$  amplitude. The individual photomultiplier pulse heights  $ph_i$  were corrected for ADC pedestals and 60 Hz correlated line noise.

A typical calibrated spectrum for a counter situated near the beam particle trajectories is shown in Fig. 4.2. Besides the main peak corresponding to the detection

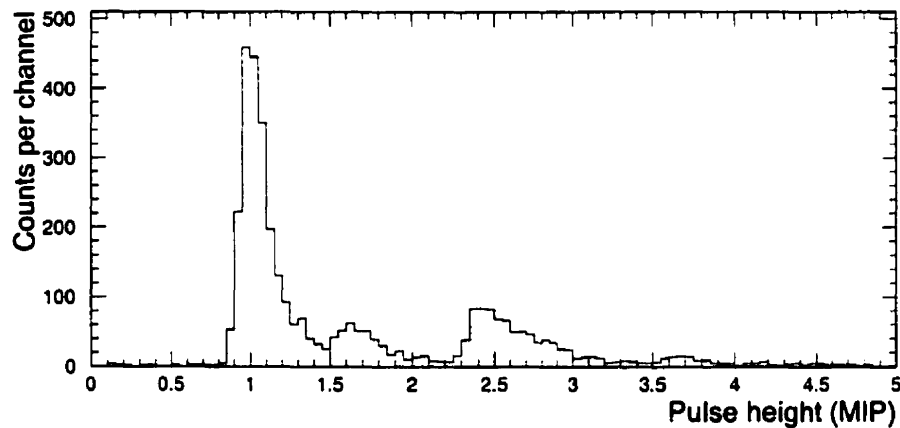


Figure 4.2: Measured pulse height distribution for a counter near the beam particle trajectories.

of single  $Z=1$  minimum ionizing particles, one observes a peak corresponding to the pile-up of two  $Z=1$  particles at 1.6 MIP, and a peak corresponding to the detection of  $Z=2$  particles at 2.4 MIP. The measured pulse height was taken into account in defining the optimum cuts for particle identification, and this was particularly important for the identification of multiply charged fragments like  $^3\text{He}$  and  $^4\text{He}$ .

### Time-of-flight measurement

The time-of-flight of particles from the target to the hodoscope counters is expressed as:

$$\text{TOF} = \frac{(t_{top}^j + t_{bottom}^j)}{2} - t_{start} - T_o^j, \quad (4.5)$$

where  $t_{top}^j$  and  $t_{bottom}^j$  are the times measured by the top and bottom phototubes of the hodoscope counter  $j$ ,  $t_{start}$  is the time measurement given by the beam counters, and  $T_o^j$  is the time offset to be determined for each counter of the hodoscope. The start time resolution provided by the beam counters was carefully analyzed and estimated to be better than 25 ps. The time offsets  $T_o^j$  were obtained by analyzing the mean of the time distribution for each slat. The shifts from the mean value were determined and corrected for during the ntuple production stage.

The fixed level discriminators used for time measurement generate a pulse height dependency of the measured time due to the finite rise-time of the pulses. This time-walk effect is inversely proportional to the square root of the measured amplitude. The correction was calculated for each tube using the corrected but uncalibrated pulse height as given by the ADCs :

$$t_i^j = t_i^j - \frac{b_i^j}{\sqrt{ph_i^j}}, \quad (4.6)$$

where  $b_i^j$  is the time-walk correction parameter for a tube  $i$  of a counter  $j$ . The time-walk correction parameters were determined by minimizing the difference between the measured time-of-flight and the calculated time-of-flight for identified particles. The time-walk correction results in a sizably improved time resolution. An average resolution of 85 ps over the entire hodoscope was obtained.

## 4.3 Spectrometer Alignment

In order to achieve precise track reconstruction it is essential to determine the exact positions of tracking detectors. BNL's survey group measured each detector's position in all three dimensions relative to the target and neutral line. In  $x$ -direction, the position information from the detectors themselves can be used to perform a relative alignment with a precision of tens of microns. Also, in case the position of the detector changed after the survey had been conducted, we still have the means to determine the correct positions of the detectors.

### 4.3.1 Alignment of tracking detectors

The last survey and self-alignment of the spectrometer were done for the 1994 run. For an inspection of the detector positions in 1995, we took the data with magnetic field turned off and the target taken out. Under these conditions the beam makes a straight path through the spectrometer. The beam tracks measured by the two beam vertex detectors (BVERs) and two drift chambers (DC2, DC3) were fitted with a straight line. The residuals  $\delta x$  of the fit are shown in Fig. 4.3 for the two BVERs, DC2 and DC3. The residuals exhibit a significant deviation from zero, thus we need to re-align these elements of the spectrometer.

The mean values of the distributions shown in Fig. 4.3 provide us only with  $x$ -positions of the detectors relative to each other. The absolute position can only be deduced from the survey data, which just proved to be inaccurate. The alignment conducted in previous years showed that the most likely detector to be moved between the running periods is DC2, as it is located in the middle of the experimental setup. The BVERs were also dismantled for the upgrade and might have been moved during re-installation. DC3, on the other hand, is the heaviest of the tracking detectors and rarely needed re-alignment. To minimize the changes in detector positions, we

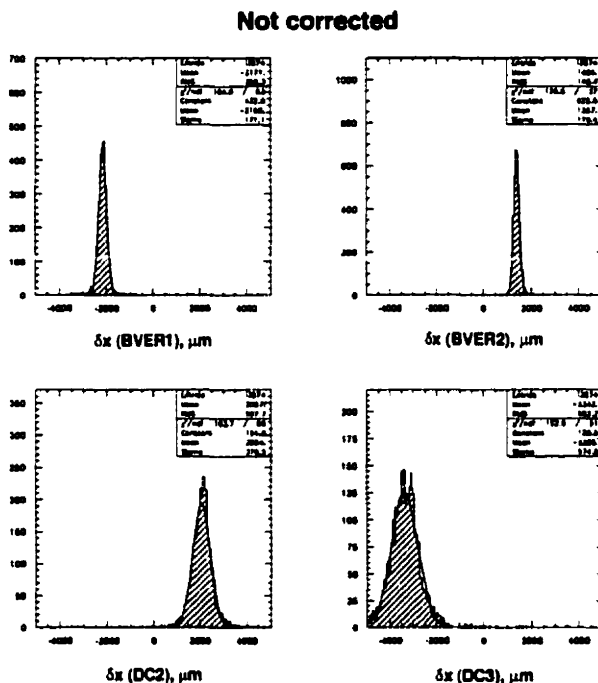


Figure 4.3: Residuals of the fit to straight tracks used to align the components of the spectrometer.

decided that the outmost detectors (BVER1 and DC3) would stay in their places, and  $x$ -positions measured by BVER2 and DC2 would be adjusted to get  $\delta x$ 's centered at zero. Shifting BVER2 by 0.9 mm and DC2 by almost 5 mm resulted in a perfect linear fit of all four detector's  $x$ -positions (Figure 4.4).

The four MWPCs located in between DC2 and DC3 and used for track confirmation were also re-aligned. The fit residuals before and after corrections are presented in Fig. 4.5. In the track reconstruction algorithm, three out of four MWPCs are required for track confirmation. When MWPCs are not aligned (left panel of Fig. 4.5), the probability of satisfying the above criterion is rather low, especially considering the small area where beam particles are traversing the spectrometer. It is indicated by the number of beam tracks found (3874 for 10000 beam triggers) and by the

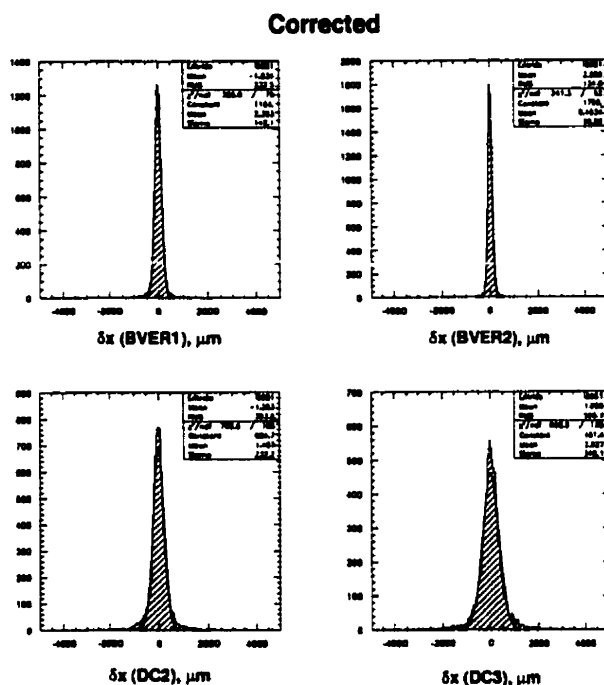


Figure 4.4: Difference between the measured position and fitted position for the two BVERs, DC2 and DC3 after corrections.

shape of the distributions. The right panel of Fig. 4.5 shows the difference between the measured position and fitted position after applying the correction factors given below. The shape of distributions is close to a square with width corresponding to the wire spacing of MWPCs (5.08 mm). The number of found tracks has dramatically improved (8681 for 10000 beam triggers).

We also checked if the detectors were properly aligned in  $y$ -direction. For this purpose we used the real data run as the pad sections of the drift chambers were disabled around the beam area. No significant deviations from the 1994 values were observed.

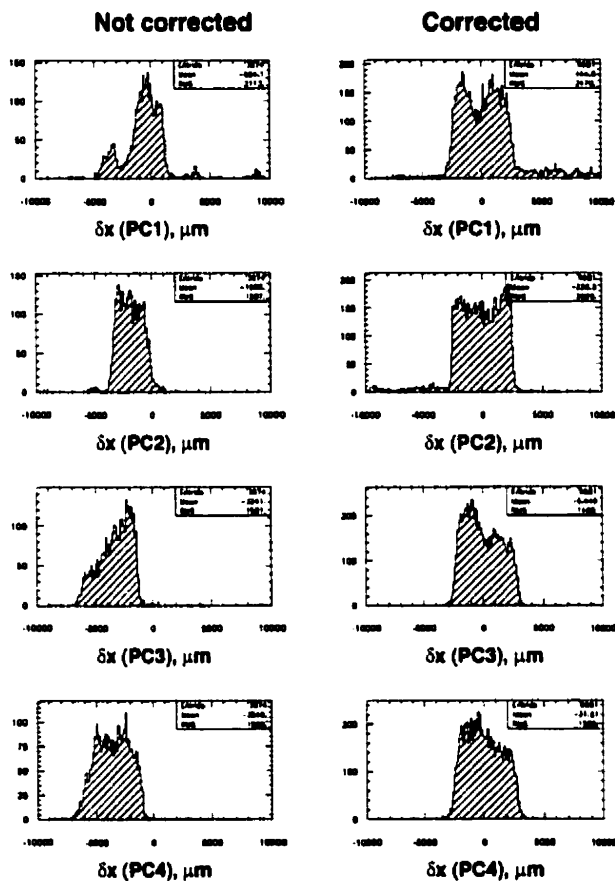


Figure 4.5: Difference between the measured position and fitted position  $\delta x$  for the four MWPCs before and after correction.

### 4.3.2 Finding the $z$ -position of DC2

Since  $x$ -position of DC2 was found to be quite off its 1994 value, we also examined the  $z$ -position of DC2 which is critical to the accuracy of momentum measurement. It is possible to do such an analysis with the data taken with magnetic field turned off but the target in. In such setup, the tracks measured by the drift chambers should be pointing to the initial interaction point at the target, which is measured by the beam vertex detectors. We examined the difference between the  $x$ -position of the beam

particles at the target measured by the BVERs and the one obtained by projecting the tracks measured by the DCs back to the target as a function of the assumed  $z$ -position of DC2 (Fig. 4.6). The variation of  $z$ -position of DC2 changes the width

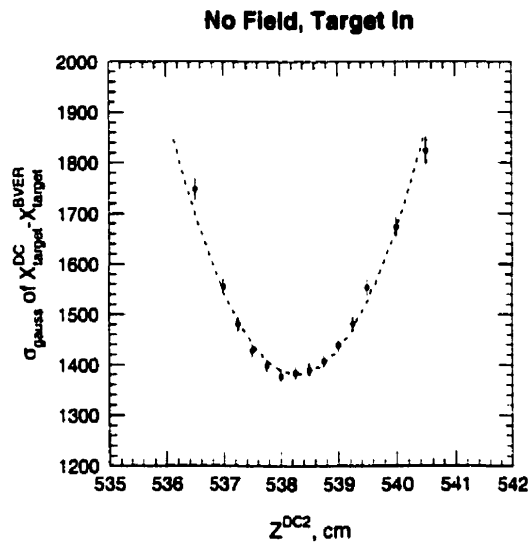


Figure 4.6: Width of the focus spot at  $z = 0$  as function of the assumed  $z$ -position of DC2.

of the “focus spot”, which was found to be minimal for  $z_{DC2} = 538.266$  cm. An adjustment of  $\sim 2.5$  mm was needed compare to the 1994 setup.

### 4.3.3 Alignment of vertex chambers

A new pair of vertex chambers (VTXA, VTXB) was installed for the 1995 run. The clusters measured in these detectors need to be aligned with the back projections of the downstream tracks. For this purpose we have used distributions of the distances  $\Delta x$  and  $\Delta y$  between the coordinate of the track given by the drift chambers and the coordinate of the closest cluster measured in the vertex chamber. The distribution

of  $\Delta x$  as a function of the measured  $x$ -position of the clusters is shown in Figure 4.7 for both vertex chambers. Besides an overall shift of the distribution from the center,

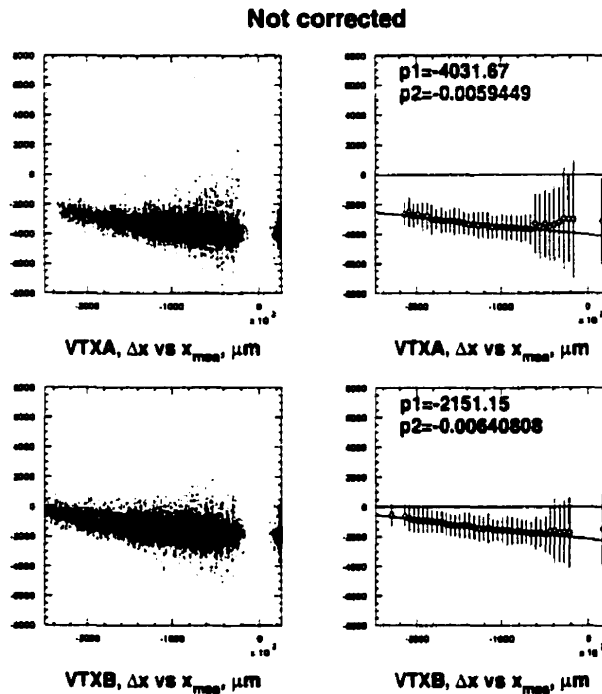


Figure 4.7: Dependence of the  $x$ -distance between track and its closest cluster ( $\Delta x$ ) on the  $x$ -position of the cluster for VTXA, VTXB before corrections.

we observe a linear dependence of the mean values on the measured position. Such dependence is typical for the offset in the  $z$ -position of the detectors. We had adjusted the  $z$ -positions of VTXA and VTXB until the position dependence disappeared, and then shifted the  $x$ -positions of the detectors to bring the mean of the residuals to zero. The results of these corrections are shown in Fig. 4.8. A similar procedure was employed for aligning the vertex detectors in  $y$ -direction. All the corrections to the 1994 detector positions are summarized in Table 4.3.3

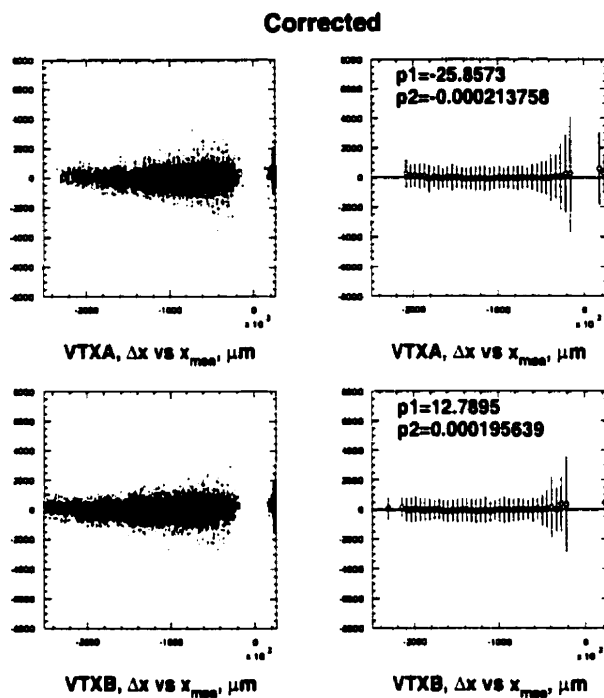


Figure 4.8: Dependence of the  $x$ -distance between track and its closest cluster ( $\Delta x$ ) on the  $x$ -position of the cluster for VTXA, VTXB after corrections.

## 4.4 Track Reconstruction

In this section we first introduce the algorithm used to reconstruct the tracks in the spectrometer, then we describe the particle identification procedures, and last we discuss various corrections needed for determining detector inefficiencies.

### 4.4.1 Track finding algorithm

The particle trajectories are constructed from hits in the tracking detectors using a road-finding algorithm. The principles of the track reconstruction program named QuanaH [95] are briefly outlined here.

Table 4.1: 1994 detector positions and parameters of 1995 alignment.

Detector	$z_{1994}, \mu\text{m}$	$\Delta z_{1995}, \mu\text{m}$	$x_{1994}, \mu\text{m}$	$\Delta x_{1995}, \mu\text{m}$
BVER1	-5856000	0	351	0
BVER2	-2799000	0	-2813	-910
VTXA	2005000	12750	0	-4118
VTXB	2255000	16000	0	-2239
DC2	5385200	-2540	227031	-4905
MWPC1	6632600	0	260230	-1378
MWPC2	7840600	0	285646	-708
MWPC3	9086900	0	318187	1246
MWPC4	10317200	0	348998	1009
DC3	11545981	0	380169	0

In Fig. 4.9 we show an  $x - z$  view of a typical Au+Au event given by the E877 event display. The track reconstruction starts with finding the wire hits in the drift chambers (DC2 and DC3). An *element* is constructed when the hit wires are found for at least 3 out of 6 wire planes of the chamber. The neighboring elements are not allowed to share more than one hit wire. The pad plane of the drift chambers is scanned for the hit pads. The  $y$ -information is determined for each *cluster* of the hit pads, and the clusters are associated with the closest wire plane elements.

Next, all possible combinations of lines connecting the elements in DC2 and DC3 are tested. Four MWPC detectors are used to reject those combinations which along their paths do not have hits in at least 3 MWPCs. The remaining combinations are stored as line *segments*. The segments are then checked if they point toward the magnet opening, and those which do are labeled as track *candidates*. The track

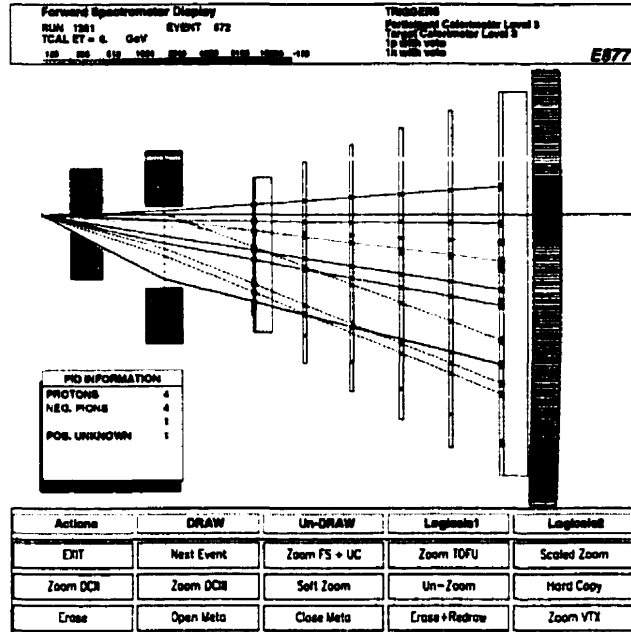


Figure 4.9:  $x - z$  view of a typical Au+Au event in the E877 event display program. The spectrometer components shown from left to right are the collimator, magnet, DC2, four MWPCs, DC3 and TOFU.

candidates are assigned momenta using the interaction position at the target given by the BVER detectors. The rigidity of each track candidate is determined from the radius of its curvature  $R$  in the magnetic field  $B$ :

$$\text{Rigidity} = p_{xz}/Z = eRB, \quad (4.7)$$

where  $p_{xz} = \sqrt{p_x^2 + p_z^2}$ , and  $Z$  is the charge of the particle. The momentum components are then given by

$$p_x = p_{xz} \sin \theta,$$

$$p_z = p_{xz} \cos \theta,$$

$$p_y = p_{xz} \arctan \phi,$$

where  $\theta$  is the angle of the candidate before the magnet in the bend plane ( $x - z$ ) of the spectrometer, and  $\phi$  is its angle in the  $y - z$  plane. Finally, the candidates that share an element or a cluster in DC2/DC3 are rejected, and the surviving candidates become *tracks*.

Each track is also assigned the time-of-flight, which is obtained by extrapolating the measured trajectory to the time-of-flight hodoscope and finding the closest hit in the scintillator wall. The power of the track reconstruction algorithm is illustrated in Fig. 4.9. Based on the hit information, 10 tracks were successfully reconstructed in this particular event, and combining the momentum and time-of-flight information, a preliminary particle identification was performed. The details of the offline particle identification procedure are given below.

#### 4.4.2 Particle identification

A simultaneous measurement of the momentum and time-of-flight for each track allows the identification of particle species. The velocity of each particle is given by  $\beta = v/c = l/\text{TOF}$ , where  $l$  is the flight path length calculated from the measured momentum and known geometry of the spectrometer. In Fig. 4.10 we show a scatter plot of the inverse momentum  $1/p$  versus the inverse of the measured velocity  $1/\beta$  for  $Z=1$  particles produced in central Au+Au collisions. The bands represent different particles separated according to their masses. The resolution is good at low momenta and gradually deteriorates with increasing momentum.

A better evaluation of the quality of the particle identification can be obtained from Fig. 4.11 where the measured mass squared distribution of positive particles is presented for three different momentum intervals. The measured mass squared

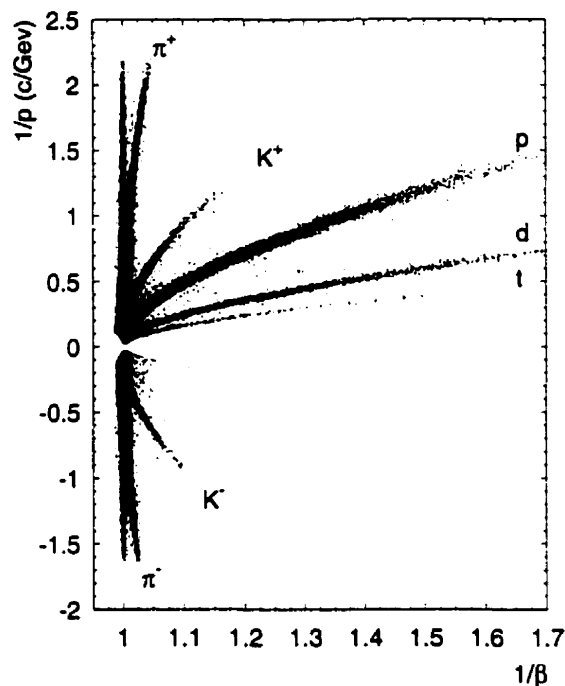


Figure 4.10: Scatter plot of the inverse momentum  $1/p$  versus the inverse of the measured velocity  $1/\beta$  for  $Z=1$  particles produced in central Au+Au collisions at 11.5 GeV/c.

associated with each track is given by:

$$m^2 = p^2 \left( \frac{1}{\beta^2} - 1 \right). \quad (4.8)$$

The three peaks on each spectrum correspond to pions, kaons and protons. The negative  $m^2$  values correspond to fast particles which due to the limited time-of-flight resolution are measured to have velocity greater than  $c$ . The spectra are characterized by a broadening of the mass peaks for increasing momentum. However, it can be seen that kaons are still well separated from pions up to momentum of 3.5 GeV/c.

The experimental mass squared resolution as a function of momentum for the

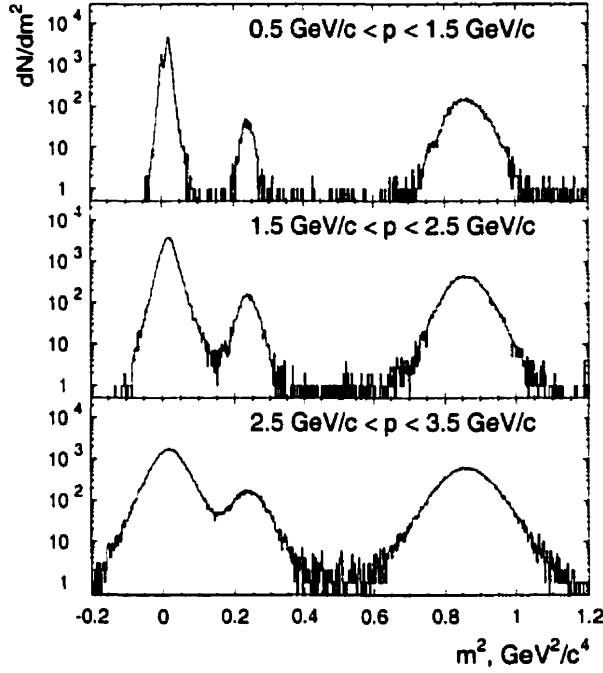


Figure 4.11: Mass spectra of positive particles in different momentum windows.

different particles is presented in Fig. 4.12. The expected mass resolution of the spectrometer is determined by both the momentum and TOF resolutions, and can be parameterized as:

$$\sigma_{m^2}^2 = 4m^4 \left\{ \left( \frac{\sigma_p}{p} \right)^2 + \left( \frac{\sigma_p^{m.s.}}{p} \right)^2 \right\} + \frac{4p^4}{\beta^2} \left( \frac{\sigma_{\text{TOF}}}{t_l} \right)^2, \quad (4.9)$$

where  $t_l$  is the time-of-flight for a  $v = c$  particle to travel the distance  $l$ . The contribution from the momentum resolution consists of two parts:  $\sigma_p$  is related to the position resolution of the tracking detectors, while  $\sigma_p^{m.s.}$  is the resolution due to multiple scattering of the particles. This contribution can be estimated by taking into account the known detector resolutions and propagating the particle through the media, taking also into account the multiple scattering in the target and detector

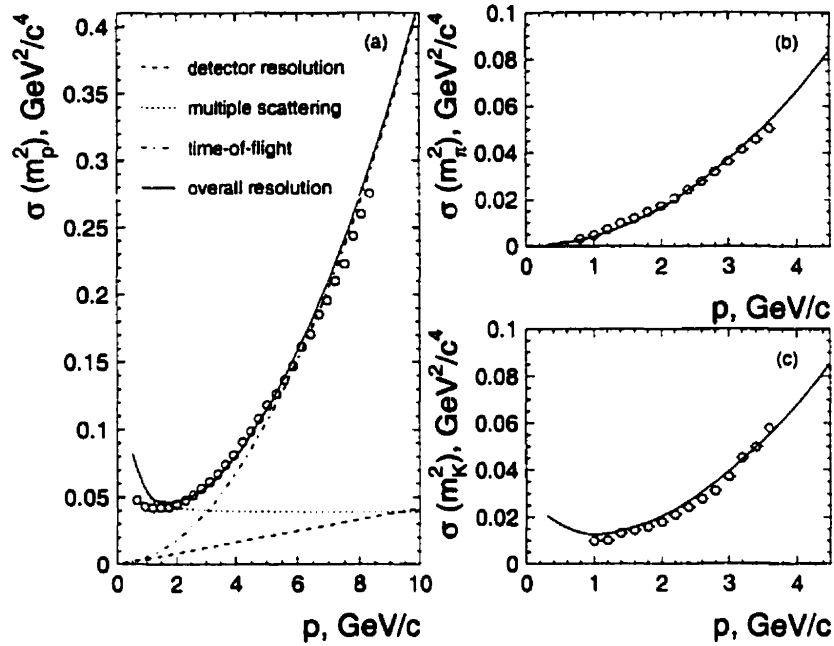


Figure 4.12: Mass squared resolution for (a) protons, (b) positive pions, and (c) positive kaons as a function of momentum. The experimental data (circles) are compared to the calculated resolutions (solid curves). In case of protons, the other curves show the various contributions to the overall resolution.

materials.

The results of such calculations are shown in Fig. 4.12 (solid lines). The time-of-flight resolution  $\sigma_{\text{TOF}}$  is assumed to be 85 ps. The various contributions to the overall resolution are shown in the case of proton (Fig. 4.12a). At very low momentum the mass resolution is mainly determined by multiple scattering of the particle in the spectrometer. However, at high momentum the overall mass resolution is largely dominated by the TOF resolution.

The particle identification was performed by making two dimensional cuts in the

momentum vs mass squared distribution. Performing the standard error propagation on Eq. 4.9,  $\sigma_{m^2}^2$  can be expressed as:

$$\sigma_{m^2}^2 = c_1^2(4m^4 p^2) + c_2^2(4m^4(1 + \frac{m^2}{p^2})) + c_3^2(4p^2(m^2 + p^2)), \quad (4.10)$$

where  $c_1 = \sigma_p/p^2$ ,  $c_2 = \sigma_p^{m \cdot s} \cdot \beta/p$ ,  $c_3 = \sigma_{\text{TOF}}/t_l$  are the parameters representing the position, multiple scattering and time-of-flight resolutions respectively. The parameters best describing the data were found by fitting the mass squared distribution sliced in many momentum windows and extracting for each window the mean value and the width of the distribution for every particle. The dependence of the width of the mass squared distribution was then fitted with Eq. 4.10. The  $c_1$  parameter was estimated analytically [96] and was fixed at 0.0024 c/GeV. The other two parameters are given in Table 4.2 for each particle.

Table 4.2: Parameters of particle identification.

particle	pions	kaons	protons	deuterons	tritons	$^3\text{He}$	$^4\text{He}$
$c_2$	0.0250	0.0250	0.0308	0.0266	0.0273	0.027	0.027
$c_3$	0.00219	0.00222	0.00223	0.00192	0.00195	0.00195	0.00195

The particle identification cuts imposed on the momentum vs measured mass plot are shown in Fig. 4.13. The particles are assigned an identification if their measured mass squared  $m^2$  is within  $\pm 1.5\sigma$  of the mean mass squared. In addition, we also require that  $m^2$  was  $2.5\sigma$  ( $3.5\sigma$  for kaons) away from the mean of other particles. In order to avoid possible mixing of particles in the high momentum region, we also impose the maximum momentum cuts, which are summarized in Table 4.3.

The quality of the particle identification can be improved by requiring for each track a confirmation from the upstream vertex pad detectors. This is illustrated

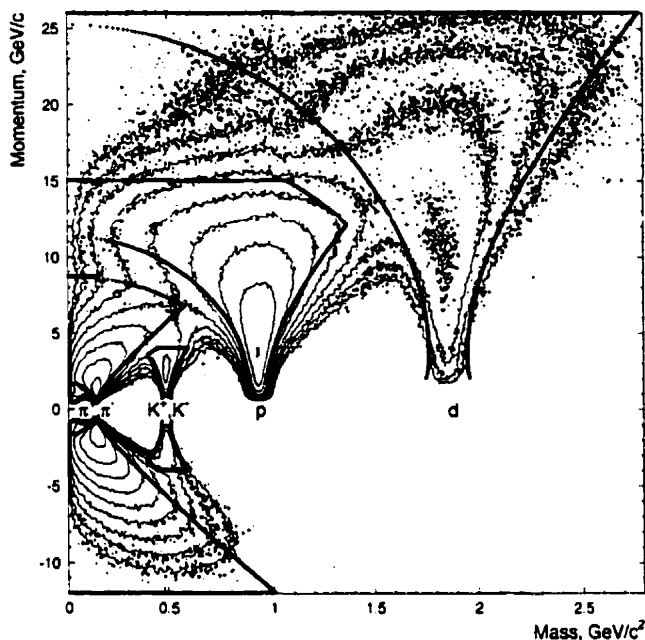


Figure 4.13: Contour plot of momentum versus mass versus distribution with PID cuts shown by the solid lines.

Table 4.3: Maximum momentum cuts for different particles.

particle	$\pi^+$	$\pi^-$	$K^+$	$K^-$	$p$	$d$
$p_{max}, \text{ GeV}/c$	8.7	13.7	3.5	3.5	15.0	26.0

in Fig. 4.14, where we show the measured mass squared distributions of positive particles in the momentum range of  $1.5 < p < 2.0 \text{ GeV}/c$  for different vertex cuts.  $\sigma_{vtx}^{either}$  indicates how close the tracks have to be to the clusters in either of the two vertex chambers to pass the cut. As one tightens the requirement, the signal-to-background ratio improves, but the tracking efficiency worsens. In our analysis, we

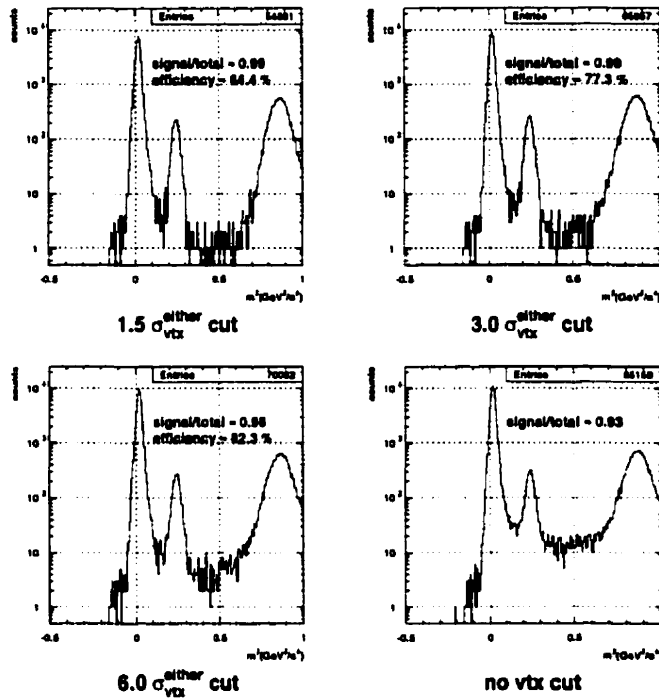


Figure 4.14: Measured mass squared distributions of positive particles in the momentum range of  $1.5 < p < 2.0$  GeV/c for different vertex cuts.

use vertex cuts only for identification of rare particle, such as  $K^+$ ,  $K^-$ .

### 4.4.3 Acceptance calculation

Only small fraction of particles emitted from the collision zone enters the magnetic spectrometer. In order to obtain the particle cross sections, we have to calculate the influence of the spectrometer's geometrical acceptance on the phase space distributions and correct for it.

The acceptance calculation is done using a Monte-Carlo simulation. Randomly generated particles are propagated through a software model of the spectrometer

which accounts for the physical boundaries of the detector systems and their dead sections. Phase space  $(p_t, y)$  distributions of “accepted” particles are then normalized by the total number of generated particles. The calculated acceptance distributions are shown in Fig. 4.15 for positive and negative pions, positive and negative kaons,

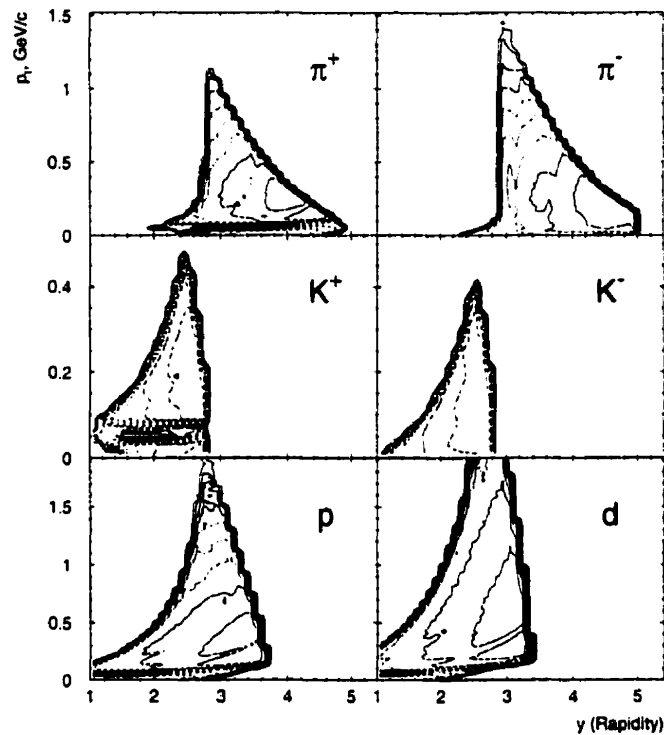


Figure 4.15: Calculated acceptance of various particles in the E877 spectrometer as a function of  $p_t$  and  $y$ .

protons, and deuterons. The left edge of the  $(p_t, y)$ -distributions is due to the geometry of the spectrometer. The right edge is determined by the magnitude of the magnetic field, as it limits the rapidity at which particles with large transverse momentum are accepted. The field polarity setting of the 1995 run also results in the

limited acceptance coverage at low  $p_t$  for positive particles due to the dead sections in the drift chambers near the beam.

#### 4.4.4 Occupancy correction

The finite occupancy of the spectrometer introduces the inefficiency in track reconstruction when two tracks are too close to each other. This is illustrated in Fig. 4.16, where we show the response of DC2, DC3 and TOFU detectors to close hits plotted

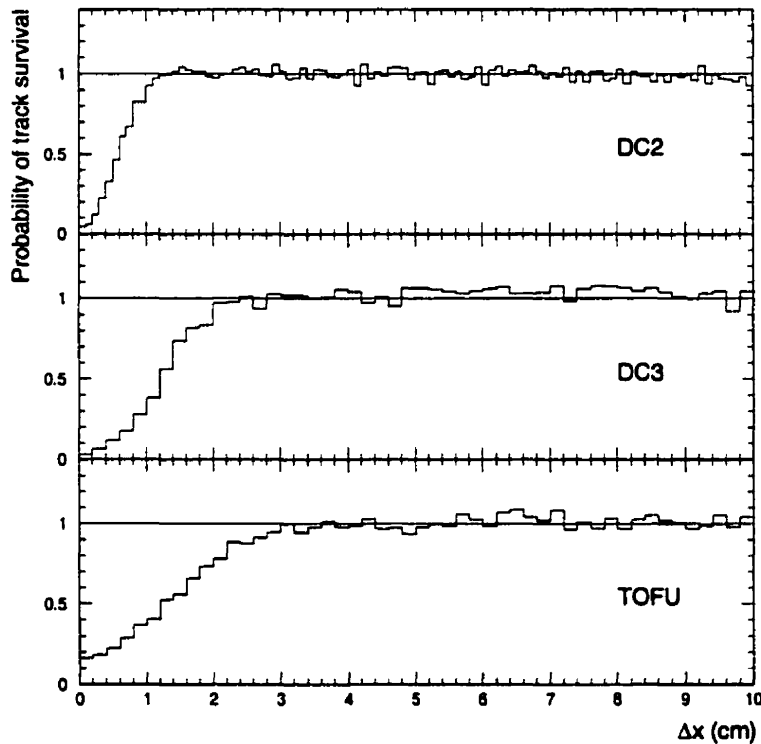


Figure 4.16: Probability of track survival as a function of track separation in DC2, DC3 and TOFU.

as a function of hit separation. The efficiency of resolving close tracks diminishes at distances shorter than 1.0 (2.0) cm in DC2 (DC3). A new method for correcting the occupancy related inefficiency was introduced in the analysis of 1995 data. The

surviving probability functions  $P_{DC2}(\Delta x)$ ,  $P_{DC3}(\Delta x)$  of DC2 and DC3 drift chambers are used to calculate a weight for each track:

$$w = 1 + \frac{1 - P_{DC2} \cdot P_{DC3}}{P_{DC2} \cdot P_{DC3}}. \quad (4.11)$$

The procedure requires two iterations, which bring the track separation distributions shown in Fig. 4.16 to unity. For more details on the 1995 occupancy correction see [70].

## 4.5 Centrality Determination

One of the global observables characterizing the event is centrality, which quantifies the overlap of the projectile and target, or violence of the collision. The degradation of initial longitudinal energy of the participating projectile and target nucleons leads to the production of transverse energy  $E_t$ :

$$E_t = \sum E_i \sin \theta_i, \quad (4.12)$$

where  $\theta$  is the the polar angle in the laboratory defined relative to the beam direction and summation is done over all particles emitted in the solid angle  $\Omega$ . The transverse energy is measured by the two calorimeters, the target calorimeter (TCAL) and the participant calorimeter (PCAL). By analyzing the transverse energy distribution, we can deduce the centrality of the collision.

The differential cross section for  $E_t$  production is given by:

$$\frac{d\sigma}{dE_t} = \frac{f_{ds}}{\rho_{tgt} \cdot \delta_{tgt} \cdot N_{beam}} \cdot \frac{dN}{dE_t}, \quad (4.13)$$

where  $f_{ds}$  is the down-scaling factor,  $\rho_{tgt} = 980 \text{ mg/cm}^2$  and  $\delta_{tgt} = 3.203 \text{ mg/Au}$  are the thickness and density of the 2% Au target, and  $N_{beam}$  is the number of beam particles measured by the beam counters.

As our trigger system has several levels with different thresholds, the overall distribution of  $dN/dE_t$  is obtained by combining the up-scaled data from beam triggers, pre-triggers, and two TCAL  $E_t$  triggers in different  $E_t$  regions (Fig. 4.17a). This

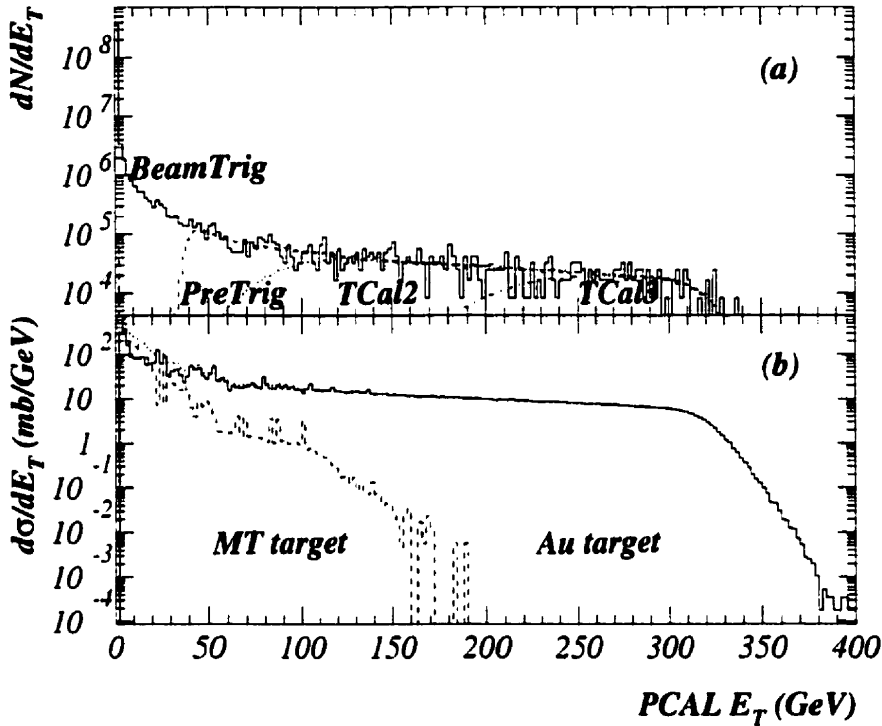


Figure 4.17: (a) PCAL  $dN/dE_t$  distribution for events from beam trigger, pre-trigger and two TCAL  $E_t$  triggers. (b) PCAL  $E_t$  differential cross-section for Au (dotted line) and MT (empty target, dashed line) targets. The solid line is the corrected  $d\sigma/dE_t$  after subtracting the MT target cross-section.

distribution is then normalized according to Eq. 4.13. The cross section is obtained by subtracting the non-target interactions, measured with MT (empty target) runs (Fig. 4.17b).

In a simple geometrical model, the colliding nuclei are treated as intersecting spheres with a radius  $R = 1.2A^{1/3}$  fm. The centrality of the collision is defined by the

ratio of the most central interaction cross section  $\sigma_{top}$  to the geometric cross section  $\sigma_{geo} = 2\pi R^2$ . Using this model, we can make a correspondence between the measured  $E_t$  and percentage of the geometric cross section:

$$\sigma_{top}/\sigma_{geo} = \frac{1}{\sigma_{geo}} \cdot \int_{E_t}^{\infty} \frac{d\sigma}{dE_t'} dE_t'. \quad (4.14)$$

The determined centrality as a function of  $E_t$  measured in TCAL and PCAL is shown in Fig. 4.18. Both calorimeters show consistent dependence, with PCAL being more

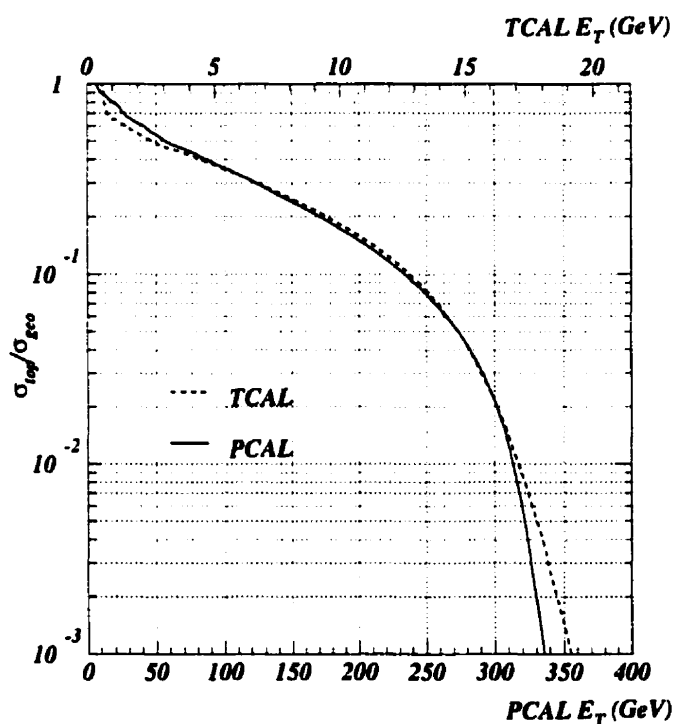


Figure 4.18: Centrality as a function of  $E_t$  for TCAL and PCAL.

sensitive in selecting the most central events. To follow run-to-run variations in the calibrated PCAL energy scale, the correspondence of PCAL  $E_t$  and centrality was done for each run.

The tracking system of the E877 experiment is capable of reconstructing all tracks

with high efficiency for events with centralities less than 26% of the geometric cross section (or PCAL  $E_t > 150$  GeV). For more peripheral collisions, the occupancy of the tracking detectors, particularly of MWPCs becomes a limiting factor, as more and more tracks enter the spectrometer. The number of tracks found by the tracking program decreases if the number of hits in MWPCs is greater than about 20. For centralities corresponding to PCAL  $E_t < 150$  GeV, the tracking program starts to fail to identify more than 5% of the tracks.

## Chapter 5

# Flow Analysis Relative to the Reaction Plane

The analysis of anisotropic transverse collective flow requires the determination of the reaction plane, spanned by the impact parameter vector and the beam axis. The E877 collaboration was first to observe directed flow in Au+Au collisions at the AGS energy [32]. The evidence for this collective effect comes from a pronounced azimuthal anisotropy of the transverse energy measured in different pseudorapidity intervals combined with a strong forward-backward anti-correlation between the direction of the observed transverse energy. The existence of directed flow allows us to reconstruct the reaction plane event by event using the azimuthal anisotropies in the transverse energy distribution measured by the E877 calorimeters.

In this chapter we will first describe the method used for the determination of the reaction plane. The procedure to correct for the non-flatness of the reaction plane distribution will be discussed in detail. A method of analyzing the azimuthal distributions using a Fourier expansion will be introduced, and a novel development for the determination of the second order deformations will be presented. Finally, we

will give a brief description of the procedures used to determine the corrections for the reaction plane resolution.

## 5.1 Reaction Plane Determination

A traditional method for the determination of the reaction plane [27] requires that the detectors provide the momentum three vectors of identified particles in the final state. Our calorimeters do not provide such information. Instead of performing an analysis over the set of the final state particles, we use the energy deposits into the calorimeter cells. Each calorimeter cell is used to construct the direction of the reaction plane by defining the components of the transverse energy directivity vector  $\vec{D}_{E_t} = (D_x, D_y)$ :

$$D_x = \sum_{j=1}^N E_t^j \cos \phi_j^{lab}, \quad (5.1)$$

$$D_y = \sum_{j=1}^N E_t^j \sin \phi_j^{lab}, \quad (5.2)$$

where  $j$  is the index of the  $\phi$  section of the calorimeter and  $\phi_j^{lab}$  corresponds to its azimuthal angle measured in the laboratory frame.

The polar coverage of the two calorimeters is divided into four windows. The definition of windows in polar angle and pseudorapidity  $\eta = -\ln \tan \frac{\theta}{2}$  is given in Table 5.1. The reaction plane angle is independently determined in each window for every event:

$$\Psi_R = \arctan \frac{D_y}{D_x}. \quad (5.3)$$

The correlation of  $\Psi_R$  obtained in different windows is used for the evaluation of the reaction plane resolution. Details of this procedure are described in section 5.3.

Ideally, the randomness of the collision geometry orientation should lead to an isotropic 2-dimensional distribution of the directivity vector  $\vec{D}_{E_t}$ , and consequently,

Table 5.1: Definition of windows in polar angle and pseudorapidity for the determination of the reaction plane.

	TCal1	PCal2	PCal3	PCal4
$\theta_{lab}$	[117°, 53°]	[48°, 28°]	[28°, 15°]	[15°, 1°]
$\eta$	[-0.5, 0.7]	[0.8, 1.4]	[1.4, 2.0]	[2.0, 4.5]

a flat distribution in  $dN/d\Psi_R$ . However, due to non-uniform coverage and calibration inaccuracies of the participant calorimeter, the measured distributions are distorted. The contour plot of the raw 2-dimensional distribution of the transverse energy vector measured in the PCal4 pseudorapidity window is presented in the left panel of Fig. 5.1a. The corresponding distribution of the reaction plane orientation is shown in the right panel. The following procedure has been developed to correct for the non-flatness of the reaction plane distribution. The correction factors are calculated for each run and the measured reaction plane orientation is corrected on an event-by-event basis.

Firstly, the non-uniformity in response of different  $\phi$  sections of the PCal calorimeter is corrected in the first order by:

$$E_{t,i}^{bj} = \frac{E_{t,i}^j}{\langle E_t^j \rangle}, \quad (5.4)$$

where  $i$  is the event index, and  $\langle E_t^j \rangle$  is the  $E_t$  measured in the  $j$  section of the calorimeter averaged over statistics of one run (200k events). Corrected  $d^2N/dD_x^b dD_y^b$  and  $dN/d\Psi_R^b$  distributions are shown in Fig. 5.1b.

At this stage we divide the event sample into several centrality bins according to the total transverse energy measured in the participant calorimeter. At the second step of the correction procedure, the directivity vector  $\vec{D}_{E_t}^b$ , measured in each centrality

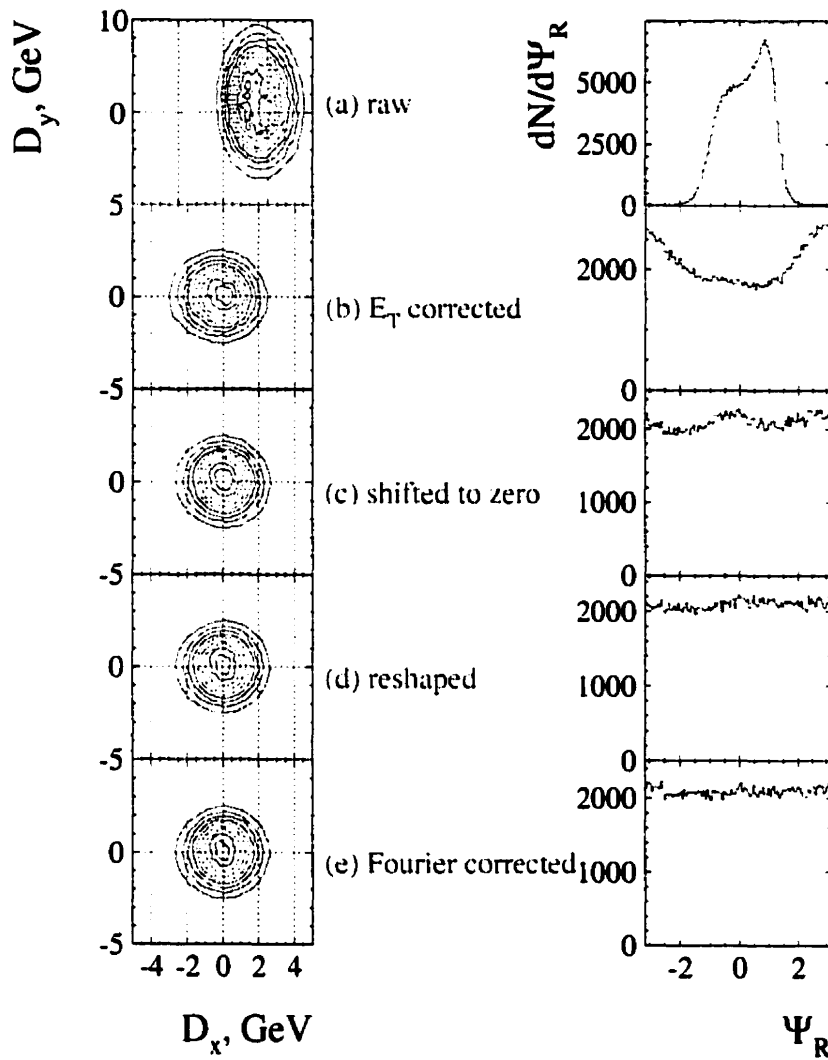


Figure 5.1: Distribution of transverse energy vector  $\vec{D}_{E_t}$  (left panel) and determined reaction plane angle given in radians (right panel) in the PCal4 pseudorapidity window. The figures from top to bottom show the raw distributions and distributions obtained after each step of the flattening procedure.

bin is shifted so that the center of the two-dimensional distribution is at the origin:

$$D_{x,i}^c = D_{x,i}^b - \langle D_x^b \rangle, \quad (5.5)$$

$$D_{y,i}^c = D_{y,i}^b - \langle D_y^b \rangle. \quad (5.6)$$

The resultant distributions of the directivity vector and corrected  $\Psi_R^c$  are presented in Fig. 5.1c.

Then, the second moment (elliptic shape) of the 2-dimensional distribution is corrected by squeezing and stretching out major axes of the observed ellipse. The axes are determined using directivity tensor constructed as follows:

$$S^\perp = \begin{pmatrix} \sum w_i^{c^2} D_{x,i}^{c^2} & \sum w_i^{c^2} D_{x,i}^c D_{y,i}^c \\ \sum w_i^{c^2} D_{x,i}^c D_{y,i}^c & \sum w_i^{c^2} D_{y,i}^{c^2} \end{pmatrix}, \quad (5.7)$$

where  $i$  is the event index,  $w_i^{c^2} = \frac{1}{D_{x,i}^{c^2} + D_{y,i}^{c^2}}$ , and sums run over 200k events. Ellipticity, defined as the ratio of the long to short axis, is found using the eigenvalues  $\lambda_1, \lambda_2$  of tensor  $S^\perp$ :  $\epsilon = \lambda_1/\lambda_2$ . The orientation of the long axis is given by:

$$\Phi_{0,i} = \frac{1}{2} \arctan \frac{2 \sum D_{x,i}^c}{\sum (D_{x,i}^{c^2} - D_{y,i}^{c^2})}. \quad (5.8)$$

Using the obtained ellipticity, we equalize the long and short axes of the ellipse while keeping the total area constant, thereby taking out the second moment:

$$D_{x,i}^d = \frac{\sqrt{\epsilon}}{w_i^c} \cos \Psi_i^c, \quad (5.9)$$

$$D_{y,i}^d = \frac{1}{\sqrt{\epsilon} w_i^c} \sin \Psi_i^c. \quad (5.10)$$

The results of this correction are shown in Fig. 5.1d.

Finally, the remaining higher order Fourier harmonics in  $dN/d\Psi_R^d$  distribution are corrected by:

$$\Psi_R^c = \Psi_R^d + \sum_n (A_n \cos n\Psi_R^d + B_n \sin n\Psi_R^d). \quad (5.11)$$

Requiring the vanishing of the  $n$ -th Fourier moment of the new distribution, the coefficients  $A_n$  and  $B_n$  can be evaluated from the original distribution:

$$B_n = \frac{2}{n} \langle \cos n \Psi_R^d \rangle, \quad (5.12)$$

$$A_n = -\frac{2}{n} \langle \sin n \Psi_R^d \rangle, \quad (5.13)$$

where the brackets refer to an average over events. In practice, we flatten the reaction plane distribution up to the fourth harmonic ( $n=4$ ). The orientation of the reaction plane also slightly depends on the incident angle of the beam particle. This effect was also considered and corrected for [70]. The final corrected distributions are shown in Fig. 5.1e.

The residuals of the reaction plane angle and its corrected value are shown in Fig. 5.2 for each step of the flattening procedure. The largest corrections are done during the first two steps, with the last two corrections bringing only a minimal change to the determination of the reaction plane angle in PCal4 window.

## 5.2 Fourier analysis of azimuthal distributions

The azimuthal anisotropy of particle production is studied by means of Fourier analysis of azimuthal distributions [28, 97, 12]. The azimuthal distribution with respect to the measured reaction plane orientation can be decomposed in the following way :

$$\begin{aligned} E \frac{d^3 N}{d^3 p'} &= \frac{d^3 N}{p_t dp_t dy d\phi} \\ &= \frac{1}{2\pi} \frac{d^2 N}{p_t dp_t dy} \left( 1 + \sum_{n=1}^{\infty} 2v_n^{obs} \cos n\phi \right), \end{aligned} \quad (5.14)$$

where we use a cylindrical coordinate system with rapidity  $y = \frac{1}{2} \ln \frac{E+p \cos \theta}{E-p \cos \theta}$  as the longitudinal axis, transverse momentum  $p_t = p \sin \theta$  as the transverse coordinate and  $\phi = \phi_{lab} - \Psi_1$  as the azimuthal angle of the particle taken with respect to the measured

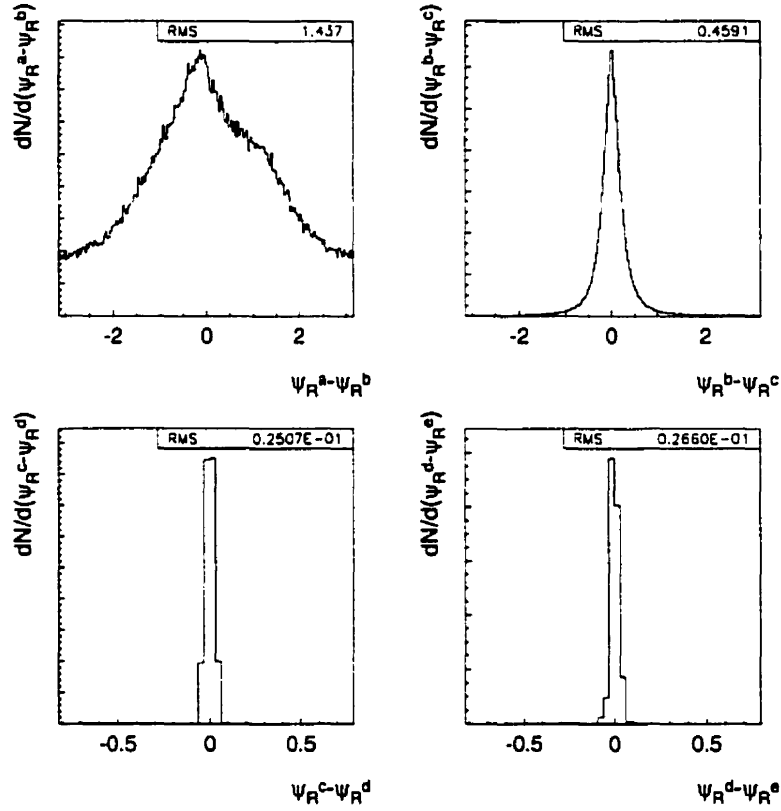


Figure 5.2: Residuals of the reaction plane angle determined in the PCal4 pseudorapidity window and its corrected value for each step of the correction procedure.

reaction plane orientation. The Fourier coefficients  $v_n^{obs}$  quantify the amplitude of the  $n$ -th harmonic of the azimuthal asymmetry and are evaluated by

$$v_n^{obs} = \langle \cos n\phi \rangle. \quad (5.15)$$

The dipole ( $v_1$ ) and the quadrupole ( $v_2$ ) coefficients in the Fourier decomposition, represent the shift (directed flow) and eccentricity (elliptic flow) of the particle azimuthal distribution and are studied as a function of rapidity, transverse momentum, and centrality of the collision.

Strong directed flow of protons and light fragments was previously measured at the AGS energy [36]. The experimental dependence of  $v_1$  on the transverse momentum is well described by a shift of the two-dimensional momentum distributions in the direction of the reaction plane [35]. The mean transverse momentum projected onto the reaction plane,  $\langle p_x \rangle$ , is about zero in the mid-rapidity region, but reaches up to 0.13 GeV/c for protons at beam/projectile rapidities.

The  $p_t$ -dependence of the  $v_1$  and  $v_2$  coefficients is illustrated in Fig. 5.3 using a simplified schematic model. The upper two plots of Fig. 5.3 show log-scaled contours of Monte Carlo simulated two-dimensional Gaussian momentum distributions with respect to the reaction plane, which is defined to be in the  $x$ -direction. We use a typical width of the proton distribution observed in 10 A· GeV Au+Au collisions of  $\sigma_{p_x, p_y} = 0.23$  GeV/c. On the left panel, the generated distribution is circular ( $\sigma_{p_x} = \sigma_{p_y}$ ) and shifted in the direction of the reaction plane. On the right panel, the generated distribution is eccentric ( $\sigma_{p_x}/\sigma_{p_y} = 1.2$ ) with respect to the reaction plane orientation, with major axis of the simulated elliptic shape lying in the reaction plane. Two plots in the middle of Fig. 5.3 show the corresponding azimuthal distributions modulated according to  $\cos \phi$  and  $\cos 2\phi$  functions. The lower panels of Fig. 5.3 show the  $p_t$ -dependence of the  $v_1$  and  $v_2$  coefficients. The amplitudes of  $v_1$  and  $v_2$  are equal to zero at  $p_t = 0$ , and rise with  $p_t$ . Except for the high  $p_t$  region,  $v_1(p_t)$ -dependence behaves linearly with  $p_t$ , whereas  $v_2(p_t)$  is well described by a quadratic dependence.

The shift of the two-dimensional momentum distribution effectively changes the circular shape of the distribution if viewed relative to the beam axis. The non-zero first moment of the distribution affects the amplitudes of higher order harmonics. This effect is illustrated in Fig. 5.4 for the second harmonic. The upper plot of Fig. 5.4 shows the  $v_2(p_t)$ -dependence for Monte Carlo simulated circular two-dimensional Gaussian momentum distributions shifted by different  $\langle p_x \rangle$  in the direction of the reaction plane. The lower plot of Fig. 5.4 shows the amplitude of the

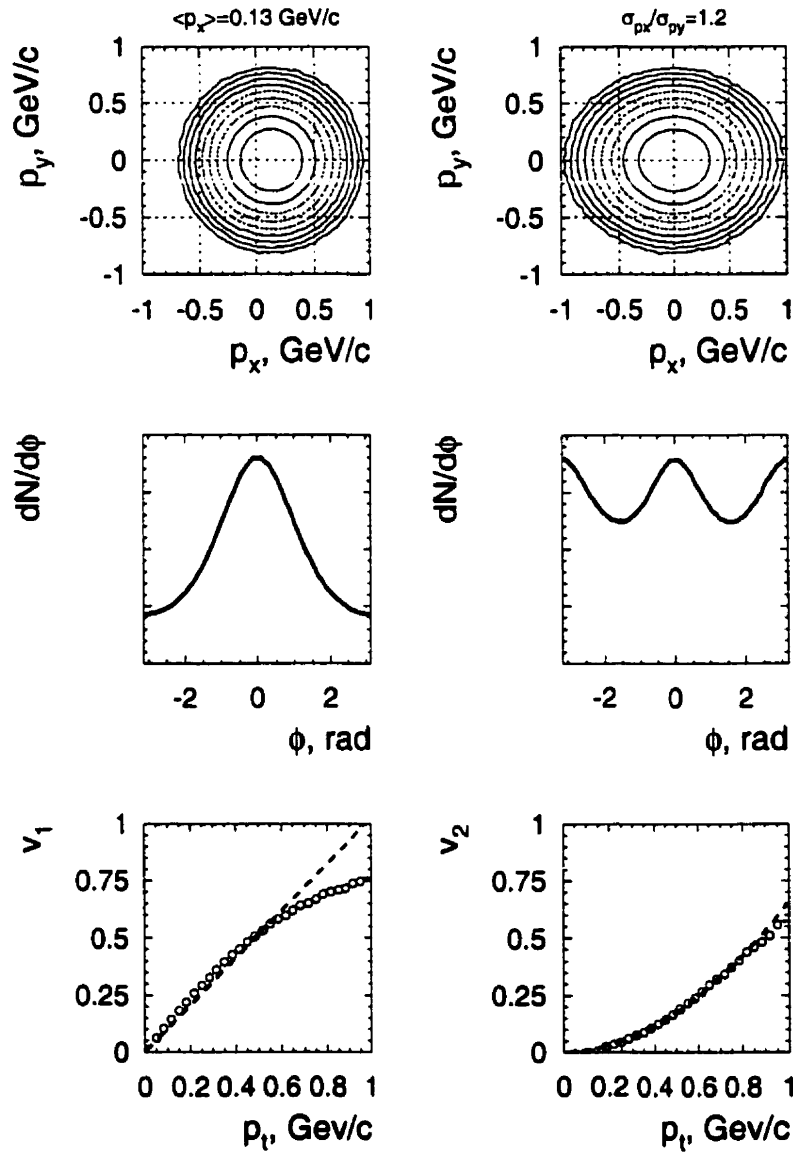


Figure 5.3: Illustration of the  $p_t$ -dependence of the  $v_1$  and  $v_2$  coefficients using a simplified schematic model

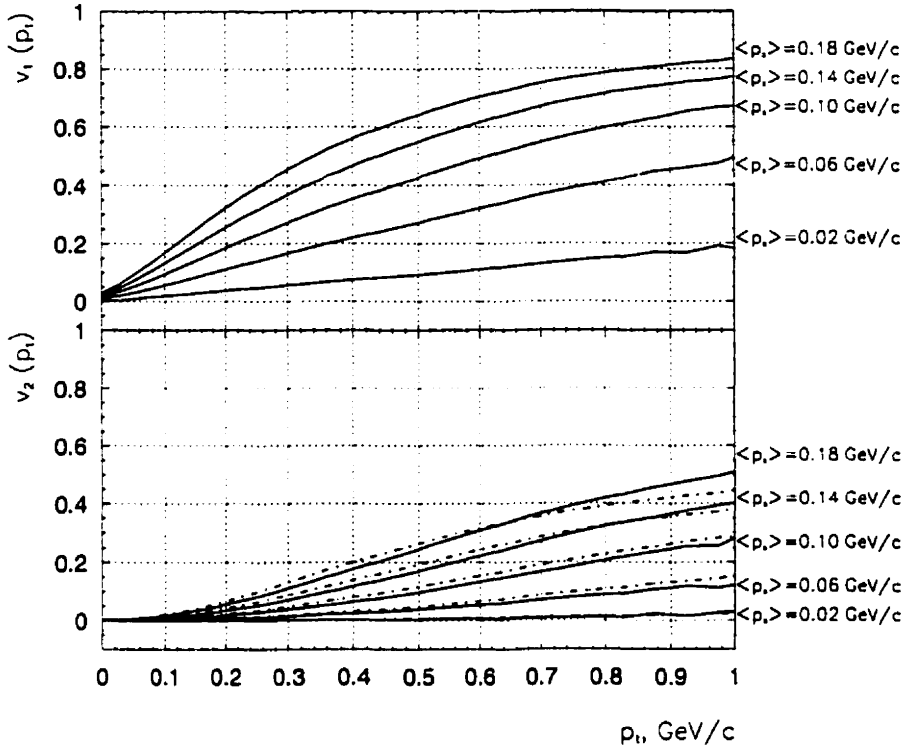


Figure 5.4:  $v_1$  and  $v_2$  as a function of  $p_t$  for Monte Carlo simulated circular two-dimensional Gaussian momentum distributions shifted by different  $\langle p_x \rangle$ . Dashed lines are parameterizations of the  $v_2(p_t)$ -dependence according to  $\frac{2}{\pi} \langle \cos \phi \rangle^2$ .

second harmonic,  $v_2$ , as a function of  $p_t$  for the same distributions. As one can see, even in the absence of the “true” elliptic deformation of the two-dimensional momentum distribution, the in-plane shift of the distribution from the origin induces a positive signal for  $v_2$ . The amplitude of this induced signal is in the first order proportional to  $\frac{2}{\pi} \langle \cos \phi \rangle^2$  (dashed lines in the lower panel of Fig. 5.4).

In order to decouple the  $v_2$ -amplitude of the “true” elliptic flow from the one induced by directed flow we propose to evaluate the second order Fourier harmonic

in the coordinate frame displaced from origin by  $\langle p_x \rangle$  in the direction of the reaction plane. In other words, we suggest to estimate the ellipticity of the 2-dimensional momentum distribution of particles relative to the reaction plane with respect to the centroid of the distribution, rather than the beam axis. To perform such an analysis, we first have to find the  $\langle p_x \rangle$ -values for each rapidity bin under study, which give us the center of the distribution in the direction of the reaction plane. Then we subtract the obtained  $\langle p_x \rangle$ -values from the measured  $p_x$ -component:

$$p'_x = p_x - \langle p_x \rangle. \quad (5.16)$$

The azimuthal angle with respect to the reaction plane in the shifted frame is then given by

$$\phi' = \arctan(p_y/p'_x). \quad (5.17)$$

The Fourier coefficients and transverse momentum are then modified accordingly:

$$v'_n = \langle \cos n\phi' \rangle, \quad (5.18)$$

$$p'_t = \sqrt{p'^2_x + p'^2_y}. \quad (5.19)$$

In Fig. 5.5 we show a simulated 2-dimensional momentum distribution deformed in the out-of-plane direction ( $\sigma_{p_x}/\sigma_{p_y} = 0.9$ ) corresponding to a negative elliptic flow, and shifted in the reaction plane by  $\langle p_x \rangle = 0.13$  GeV/c. The  $v_2$ -dependence shown on the left is calculated with respect to the beam axis. As one can see, although the elliptic deformation of the 2-dimensional momentum distribution is supposed to result in the negative values of  $v_2$ , the large in-plane shift of the distribution induces weak positive values of  $v_2$ . When the origin is placed at the center of the distribution (right side of Fig. 5.5), the effect of directed flow is canceled ( $v'_1(p'_t) \approx 0$ ), and  $v'_2(p'_t)$ -dependence provides the “true” measure of the out-of-plane ellipticity.

In practice, many experimental setups have limited acceptance in  $p_t$ . Particularly, the acceptance for positive particles in the E877 setup for the 1995 running period is

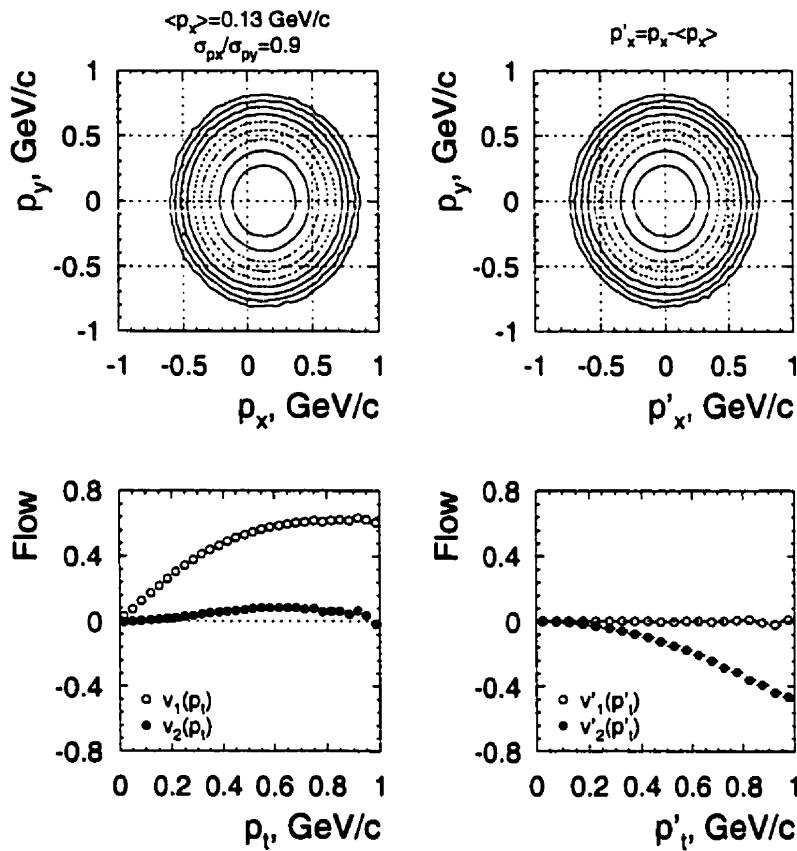


Figure 5.5: Panels on the left: Monte Carlo simulated two-dimensional Gaussian momentum distribution with out-of-plane elliptic deformation ( $\sigma_{p_x}/\sigma_{p_y} = 0.9$ ) and shifted by  $\langle p_x \rangle = 0.13 \text{ GeV/c}$  in the direction of the reaction plane, and corresponding  $v_1(p_t)$  and  $v_2(p_t)$  signals measured relative to the beam axis. Panels on the right: same distribution in the frame shifted by  $\langle p_x \rangle$  and corresponding  $v'_1(p'_t)$  and  $v'_2(p'_t)$  signals.

limited at low transverse momenta. Also, the maximum momentum cuts applied for particle identification limit the high range of the transverse momentum. The effect of the limited acceptance in the transverse momentum on  $v'_1(p'_t)$  and  $v'_2(p'_t)$  is considered

in Fig. 5.6. We show the same distribution as in Fig. 5.5, but with no acceptance

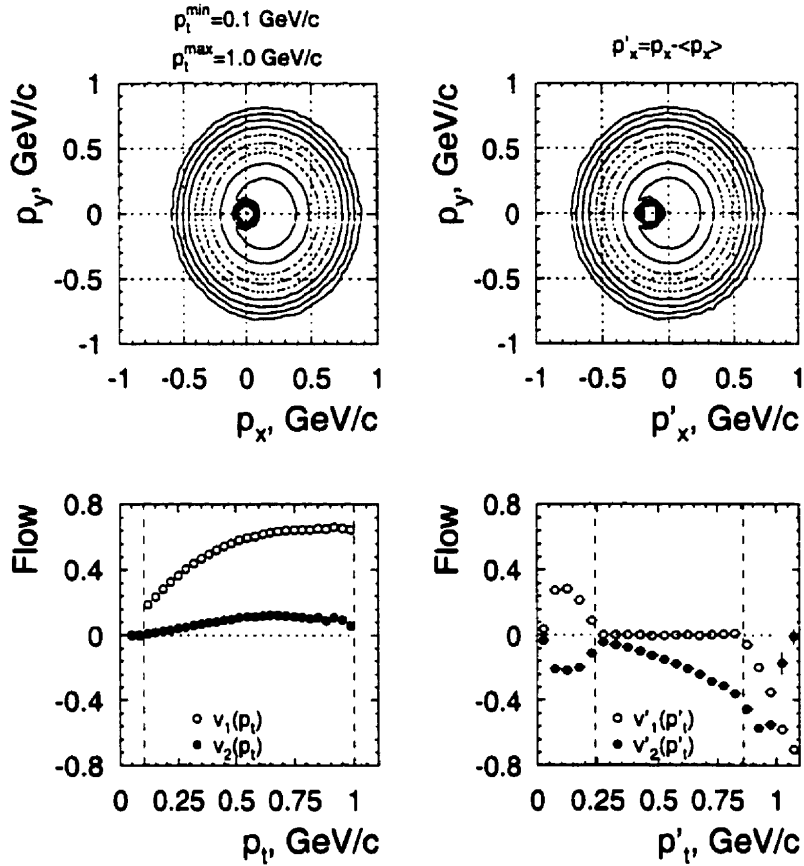


Figure 5.6: Same as Fig. 5.5, but with limited  $p_t$  acceptance.

for  $p_t < p_t^{\min} = 0.1$  GeV/c and  $p_t > p_t^{\max} = 1.0$  GeV/c. The minimum transverse momentum at which the distribution placed in the new frame is not distorted increases by  $\langle p_x \rangle$ . The distortion results in positive values of  $v'_1$  at low  $p'_t$  as the hole in the experimental acceptance is no longer centered at the origin. The maximum  $p_t$ -cut results in a similar effect at high  $p'_t$ . The range of transverse momenta where distribution is not distorted by zero acceptance at low and high  $p_t$ 's is given by

$$p_t^{\prime \min} = p_t^{\min} + \langle p_x \rangle, \quad (5.20)$$

$$p_t^{\prime \max} = p_t^{\max} - \langle p_x \rangle. \quad (5.21)$$

These limits are shown in Fig. 5.6 by dashed lines. Within this range, the first moment of the distribution in the shifted frame is equal to zero, and  $v_2'(p_t')$  is estimated correctly.

### 5.3 Reaction plane resolution

The reaction plane resolution, i.e., the accuracy with which the reaction plane orientation is determined, is evaluated by studying the correlation between reaction plane angles  $\Psi_1^{(i)}$  determined in different pseudorapidity windows  $i$ .

The true values  $v_n$  of the Fourier coefficients can be obtained from the measured values  $v_n^{obs}$  by unfolding the finite resolution of the determination of the true reaction plane angle  $\Psi_R$  [28, 34]:

$$v_n = \frac{v_n^{obs}}{|\langle \cos n(\Psi_1^{(i)} - \Psi_R) \rangle|}. \quad (5.22)$$

The brackets indicate the event average evaluated for a given pseudorapidity window and a given event centrality. As the mean cosine in the denominator is less than one, the corrected values of  $v_n$  are always larger than the measured values  $v_n^{obs}$ . The measurement of  $\Psi_1^{(i)}$  in three windows allows one to evaluate the correction factors  $\langle \cos n(\Psi_1^{(i)} - \Psi_R) \rangle$  directly from the data:

$$\begin{aligned} \cos n(\Psi_1^{(i)} - \Psi_1^{(j)}) &= \cos n(\Psi_1^{(i)} - \Psi_R) \cos n(\Psi_1^{(j)} - \Psi_R) \\ &+ \sin n(\Psi_1^{(i)} - \Psi_R) \sin n(\Psi_1^{(j)} - \Psi_R). \end{aligned} \quad (5.23)$$

Taking the event average, the sin terms vanish due to the symmetry of Au+Au colliding system with respect to the reaction plane. Assuming that the only correlation between pseudorapidity windows  $i$  and  $j$  is via the flow effect we obtain

$$\langle \cos n(\Psi_1^{(i)} - \Psi_1^{(j)}) \rangle = \langle \cos n(\Psi_1^{(i)} - \Psi_R) \rangle \langle \cos n(\Psi_1^{(j)} - \Psi_R) \rangle. \quad (5.24)$$

Combining correlations between three pseudorapidity windows  $i, j, k$ , we can deduce the inverse correction factors for the finite reaction plane resolution in window  $i$ :

$$|\langle \cos n(\Psi_1^{(i)} - \Psi_R) \rangle| = \sqrt{\frac{\langle \cos n(\Psi_1^{(i)} - \Psi_1^{(j)}) \rangle \langle \cos n(\Psi_1^{(i)} - \Psi_1^{(k)}) \rangle}{\langle \cos n(\Psi_1^{(j)} - \Psi_1^{(k)}) \rangle}}. \quad (5.25)$$

The correction factors for  $n = 1, n = 2$  estimated according to Eq. 5.25 are shown for four pseudorapidity windows in Fig. 5.7. The signs of the correction factors reflect

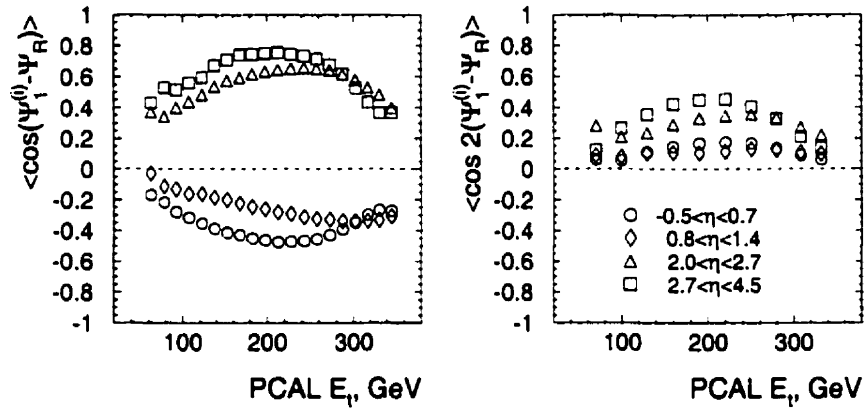


Figure 5.7: Inverse correction factors due to the finite resolution of the reaction plane angle  $\Psi_R$  measurement for the first ( $v_1$ ) and second moment ( $v_2$ ) in four different bins of pseudorapidity.

the phase shift by  $\pi$  in the angles  $\Psi_1$  at mid-pseudorapidity. The resolution in a given  $\eta$  interval is determined by the finite granularity, the energy resolution and leakage fluctuation of the detector, and the magnitude of the anisotropy in this  $\eta$  interval. The correction is smallest for semicentral collisions, where flow effects are largest. The best resolution is achieved for the most forward window ( $2.7 < \eta < 4.5$ ). The quadrupole component ( $v_2$ ) requires larger corrections.

The redundancy in the number of pseudorapidity windows (we divided the polar coverage of the calorimeters into four windows whereas only three are necessary to estimate the correction factors according to Eq. 5.25) allows to study the correlations between the correction factors obtained with different combinations of windows. These correlations are sensitive to the non-flow effects, such as shower sharing between the calorimeter cells and momentum conservation. A detailed study of these correlations has been done in [70]. The correction factors shown in Fig. 5.7 have been optimized to achieve consistent values for all possible combinations of pseudorapidity windows. The optimized factors for the correction of the first harmonic ( $v_1$ ) taken from [70] are shown as solid symbols in Fig. 5.8. For comparison, we also show the non-optimized corrections as open symbols. The non-flow correlations

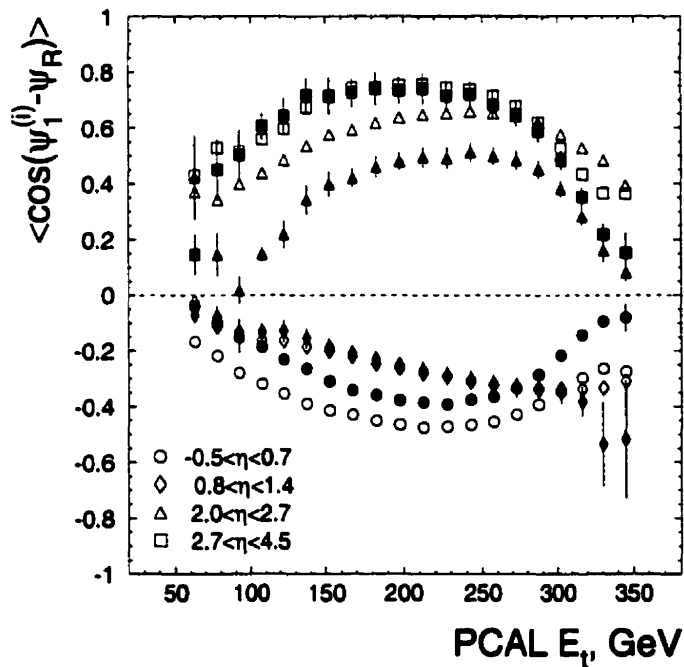


Figure 5.8: Inverse correction factors for  $v_1$ , with (solid symbols) and without (open symbols) optimization, in four different bins of pseudorapidity.

cause over-estimation of the resolution calculated according to Eq. 5.25 in the windows  $-0.5 < \eta < 0.7$  and  $2.0 < \eta < 2.7$ .

Two windows with the best resolution,  $2.0 < \eta < 2.7$  and  $2.7 < \eta < 4.5$ , can be combined into one ( $2.0 < \eta < 4.5$ ) to achieve yet a better resolution. A method for estimating the resolution of the combined window based on the resolutions obtained for each individual window is described in detail in [70]. Fig. 5.9 presents the obtained results for the  $v_1$  and  $v_2$  correction factors in the combined pseudorapidity window

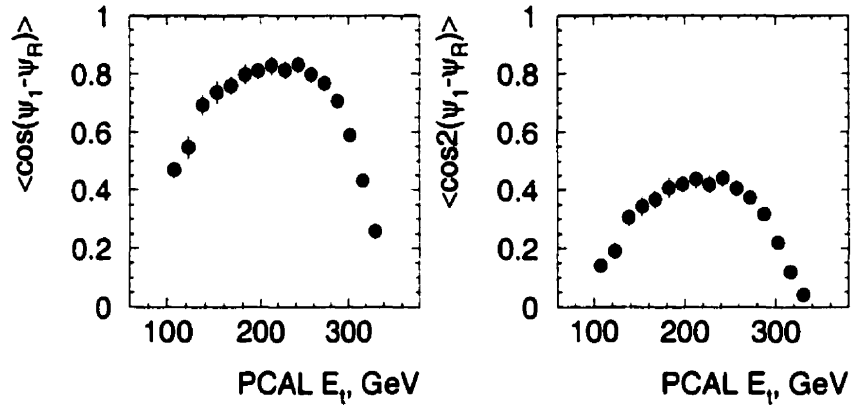


Figure 5.9: Inverse correction factors for  $v_1$  and  $v_2$  in the combined window  $2.0 < \eta < 4.5$ .

$2.0 < \eta < 4.5$ . The reaction plane orientation determined in this window is used in the further analysis of the particle azimuthal anisotropies.

## Chapter 6

# Elliptic Flow of Protons and Deuterons

In this chapter we present an analysis of proton and deuteron production with respect to the reaction plane with an emphasis on elliptic deformation of the flow tensor. The measurements cover a rapidity region  $2.0 < y < 3.4$ . We compare the experimental measurements of elliptic flow signal with the mean field and cascade codes of the Relativistic Quantum Molecular Dynamics model, combined in case of deuterons with coalescence model. We also study the influence of the transverse component of radial expansion flow on azimuthal anisotropies.

### 6.1 Experimental Results

We quantify the elliptic flow by  $v_2$ , the second coefficient in Fourier decomposition of the azimuthal particle distribution. The coefficient  $v_2$  is analyzed as a function of the transverse momentum for different rapidity bins and centralities of the collision. Four centrality bins were selected according to the transverse energy measured in the PCAL calorimeter. The selected centrality regions are presented in Table 6.1. A

simple geometrical model (see section 4.5) was used to estimate the range of impact parameter  $b$  in accordance with  $\sigma_{top}/\sigma_{geo} \approx (b/2R)^2$ . The average inverse correction factors for the finite resolution of the reaction plane are also given for  $v_1$  and  $v_2$ .

Table 6.1: Definition of the centrality regions.

Centrality	PCAL $E_t$ (GeV)	$\sigma_{top}/\sigma_{geo}$	$b$ (fm)	$v_1$ -resolution	$v_2$ -resolution
1	150 – 200	0.26 – 0.17	6 – 7	0.77	0.386
2	200 – 230	0.17 – 0.12	5 – 6	0.79	0.430
3	230 – 270	0.12 – 0.07	4 – 5	0.75	0.407
4	> 270	< 0.07	< 4	0.64	0.219

The dependence of proton  $v_2$  coefficient on the transverse momentum for different rapidity and centrality bins is presented in Fig. 6.1. The values of  $v_2(p_t)$  are corrected for the reaction plane resolution. The systematic errors are estimated by the Fourier coefficients of the  $\sin 2\phi$  term which should be zero due to symmetry. The error bars shown include both statistical and systematic error. The absence of the low  $p_t$  data is due to the 1995 experimental acceptance. The results presented in Fig. 6.1 are consistent with an independent analysis of 1994 data published in [35]. A clear positive signal is observed for all rapidities, which corresponds to an elliptically shaped distribution with the major axis lying in the reaction plane. However, the rapidity dependence of the  $v_2$ -amplitude is somewhat surprising. The amplitude of  $v_2$  increases with rapidity, and is most significant at beam rapidities. In the previous measurement of transverse energy and particle flow [34], the maximum amplitude of the in-plane elliptic flow was observed at mid-pseudorapidities, contrary to the behaviour exhibited by the data shown in Fig. 6.1.

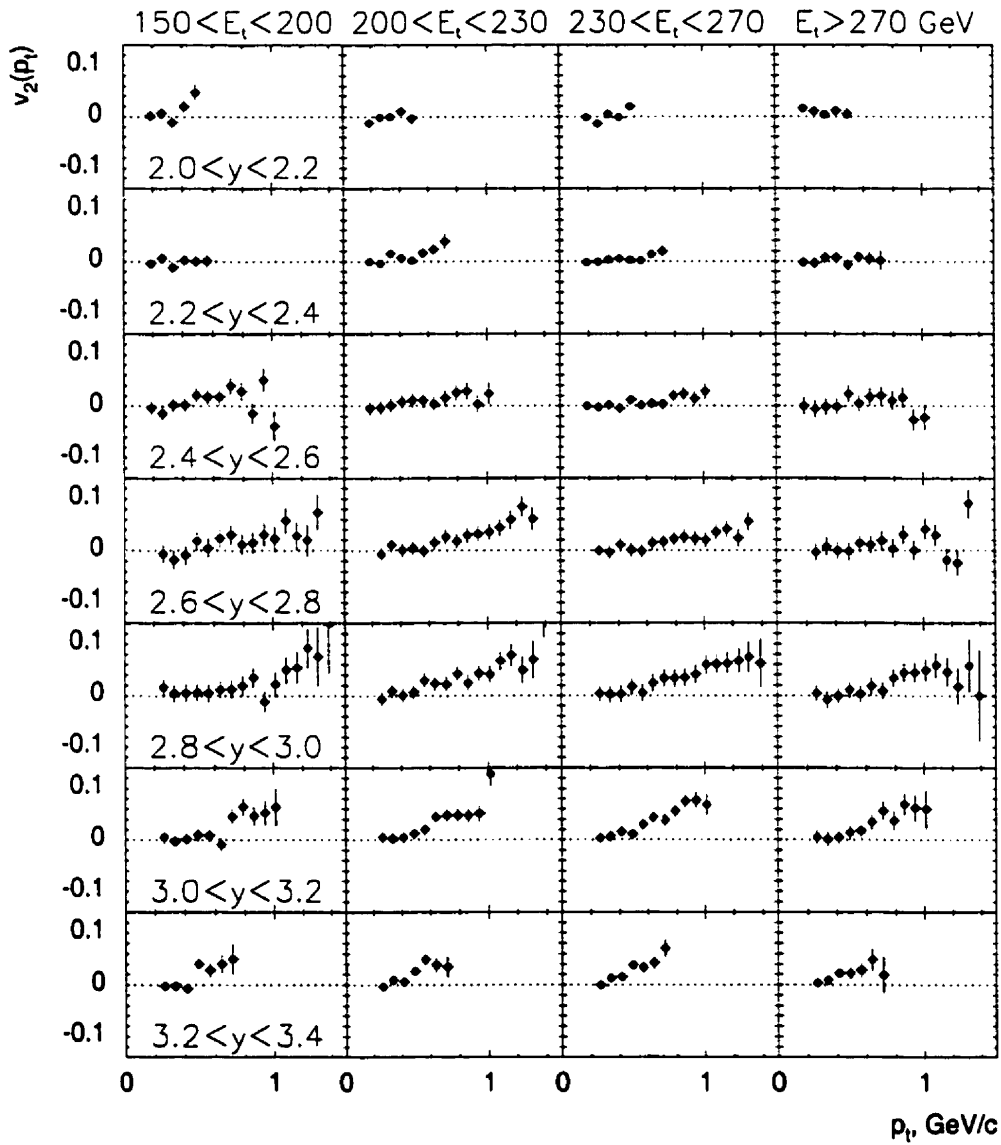


Figure 6.1:  $v_2(p_t)$  of protons for different rapidity and centrality bins.

### 6.1.1 $\langle p_x \rangle$ -subtraction

As we have seen in the previous chapter, the measured  $v_2$  values may be affected by the in-plane shift of the 2-dimensional transverse momentum distribution  $d^2N/dp_x dp_y$ , which is a result of the directed flow. This effect is particularly important for the  $v_2$  measurements away from mid-rapidity, where the influence of the directed flow is not negligible. This is illustrated in Fig. 6.2 where we show the  $d^2N/dp_x dp_y$  distributions for protons and deuterons in the rapidity bin  $3.1 < y < 3.2$ . The momentum components are given with respect to the reaction plane orientation, so that  $x$ -axis points in the direction of the reaction plane. The center circles indicate a hole in

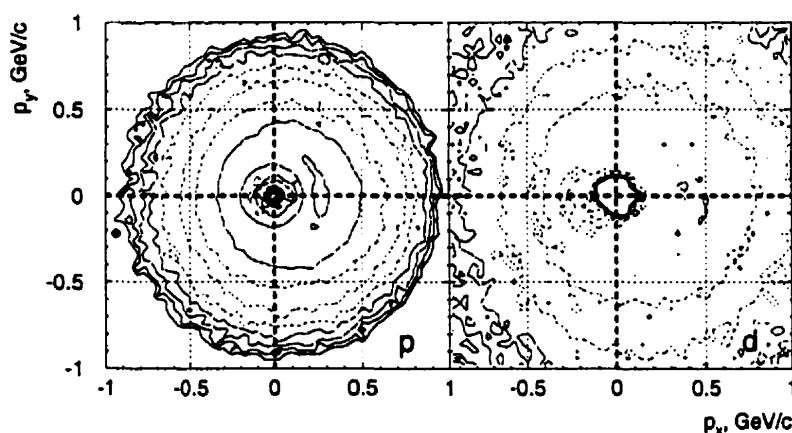


Figure 6.2: Contour plot of the  $d^2N/dp_x dp_y$  distributions for protons and deuterons in the rapidity bin  $3.1 < y < 3.2$  for centrality region  $200 < E_t < 230$  GeV.

the experimental acceptance at low  $p_t$ , which is larger for heavier deuterons. Distributions for both particles are shifted in the reaction plane, which is the evidence of strong directed flow. The standard procedure for the calculation of  $v_2$  is to analyze it in the frame centered at the beam axis. The interpretation of the results is then far from straightforward, as the amplitude of  $v_2$  will depend not only on the ellipticity

of the event, but also on the shift of the distribution due to directed flow. As was demonstrated in the previous chapter, such a shift results in a positive  $v_2$  signal even in the absence of elliptic deformation.

To analyze the “true” ellipticity of the event, we estimate the  $v_2$  coefficient in the frame shifted in the direction of the reaction plane by an amount corresponding to the strength of the directed flow, that is by the mean transverse momentum in the reaction plane  $\langle p_x \rangle$ . In the framework of a transversely moving thermal source, this transformation would correspond to analyzing the elliptic deformation of the flow tensor in the rest frame of the source which is boosted along the  $p_x$  axis with anisotropic transverse velocity  $\beta_x$ . It has been shown that both parameterizations describe the behaviour of  $v_1$  on  $p_t$  very well [35].

The strength of directed flow varies with rapidity. The rapidity dependence of  $\langle p_x \rangle$  with the average estimated in the experimental acceptance is presented in Fig 6.3 for protons and deuterons. It is a typical “S-shaped” curve with maxima at projectile/target rapidities. The rapid decrease of  $\langle p_x \rangle$  towards mid-rapidity reflects the quickly narrowing  $p_t$  acceptance of the spectrometer. Deuterons exhibit larger values of  $\langle p_x \rangle$ . As one can see, starting from rapidities around  $y = 2.4$  the directed flow is not negligible and should be taken into account when evaluating the elliptic deformation of the flow tensor. The values of  $\langle p_x \rangle$  are estimated in the experimental acceptance in  $\Delta y = 0.1$  rapidity bins and four centrality bins for each particle.

From now on, we introduce primed symbols to denote quantities evaluated in the coordinate system shifted by  $\langle p_x \rangle$ :

- transverse momentum projected in the reaction plane:  $p'_x = p_x - \langle p_x \rangle$
- azimuthal angle with respect to the reaction plane:  $\phi' = \arctan\left(\frac{p_y}{p'_x}\right)$
- transverse momentum:  $p'_t = \sqrt{p'^2_x + p^2_y}$

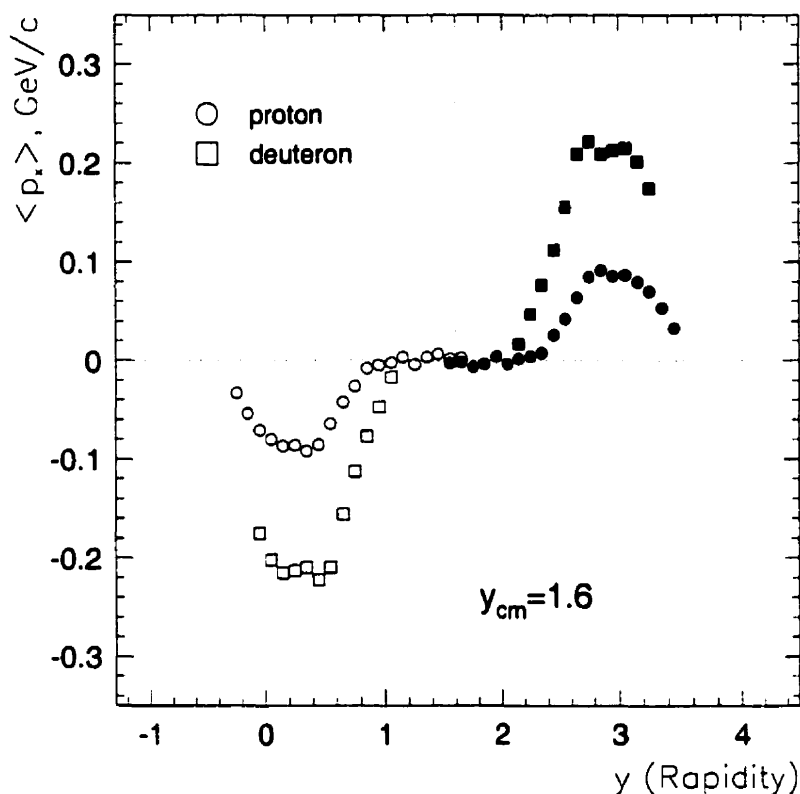


Figure 6.3: Mean transverse momentum in the reaction plane estimated in the experimental acceptance for centrality region  $200 < E_t < 230$  GeV. The open points are obtained by reflection around mid-rapidity  $y = 1.6$ .

- transverse mass:  $m'_t = \sqrt{p_t'^2 + m^2}$
- Fourier coefficients quantifying flow:  $v'_n = \langle \cos n\phi' \rangle$

The effect of the  $\langle p_x \rangle$ -subtraction on the directed flow signal is illustrated in Fig. 6.4, where we show the dependences  $v_1(p_t)$  and  $v'_1(p'_t)$  for protons as open and solid circles for various rapidity and centrality bins. As expected, after subtracting  $\langle p_x \rangle$  the directed flow is canceled:  $v'_1(p'_t) \approx 0$  for all rapidity bins and collision centralities.

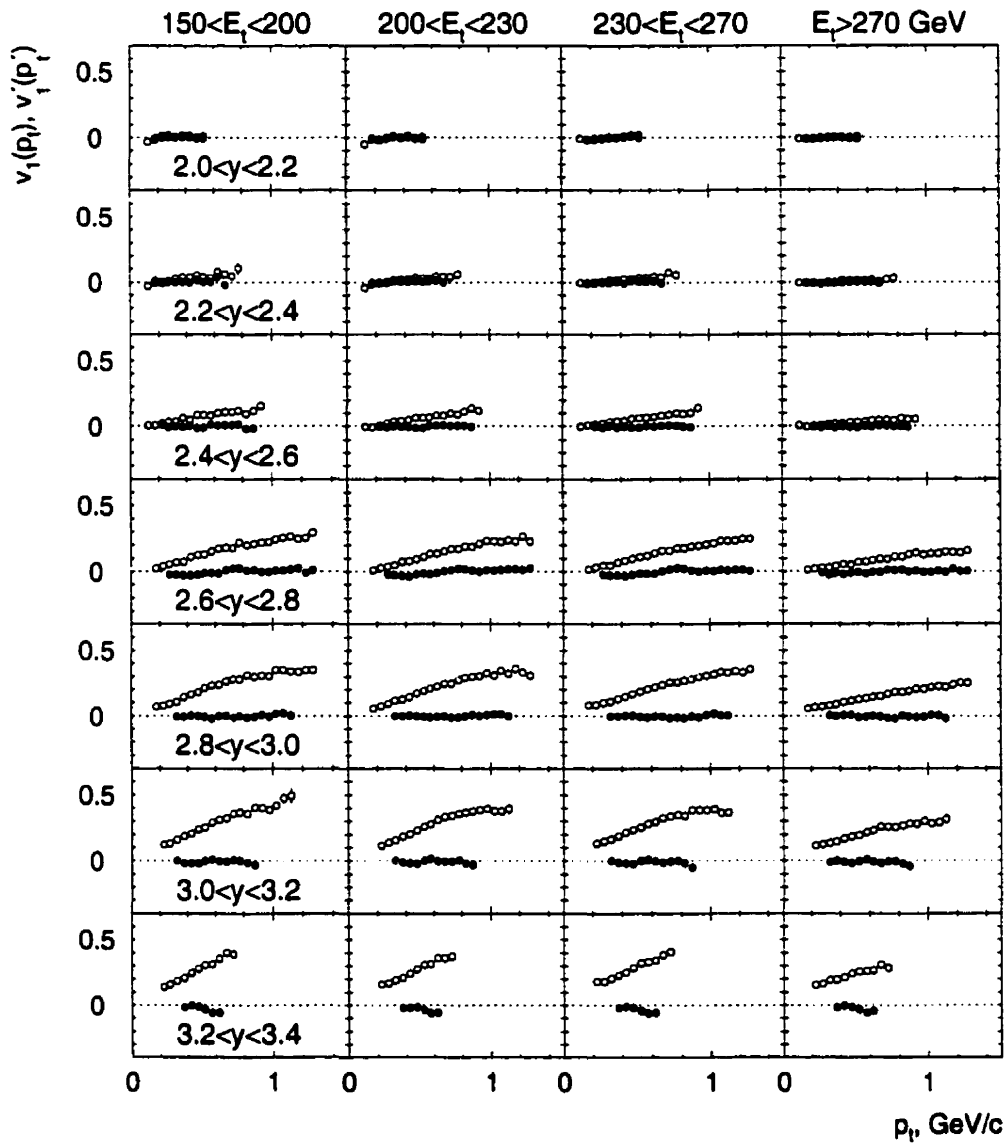


Figure 6.4:  $v_1(p_t)$  (open circles) and  $v_1'(p_t)$  (solid circles) of protons for various rapidity bins and collision centralities.

The effective  $p_t$ -coverage has decreased at low and high transverse momenta. This effect was considered in the previous chapter and is due to the hole in the experimental acceptance at low  $p_t$  on one side, and the maximum momentum cut on the other.

### 6.1.2 Elliptic Flow of Protons and Deuterons

In this section we present the results of the Fourier analysis of the proton and deuteron azimuthal distributions in the frame shifted by the measured  $\langle p_x \rangle$  in the direction of the reaction plane. The  $v'_2$  coefficient is first studied as a function of the transverse momentum  $p'_t$  for different rapidity and centrality bins, and then we investigate the rapidity dependence  $v'_2(y)$  of the elliptic flow signal.

#### $v'_2$ as a function of $p_t$

The dependence of  $v'_2$  on the transverse momentum is presented in Fig. 6.5 as solid circles. For comparison, we also show the  $v_2(p_t)$ -dependence as open circles. In the region where  $\langle p_x \rangle$  is small ( $2.0 < y < 2.4$ ) the two measurements are consistent with each other. At higher rapidities, the amplitude of  $v'_2$  is getting smaller than that of  $v_2$ . In rapidity bin  $2.6 < y < 2.8$ ,  $v'_2 \approx 0$  for all transverse momenta. The  $p_t$ -dependence of  $v'_2$  is less pronounced than that of  $v_2$ , but clear negative values of  $v'_2$  are observed in the high  $p_t$  region at rapidities  $y > 2.8$ . Larger amplitudes are observed for more peripheral collisions. Similar results shown in Fig. 6.6 are obtained for deuterons. The magnitudes of both  $v_2(p_t)$  and  $v'_2(p'_t)$  are larger for deuterons than for protons.  $v'_2(p'_t) \approx 0$  for rapidity bin  $2.4 < y < 2.6$ , compare to  $2.6 < y < 2.8$  for protons. It should be noted, that the deuteron sample in the region  $2.6 < y < 3.0$  contains an admixture of protons which is estimated to be no more than 15-20%. Given that protons exhibit a similar flow signal, the relative errors in the final results due to deuteron misidentification in that region are about 5%.

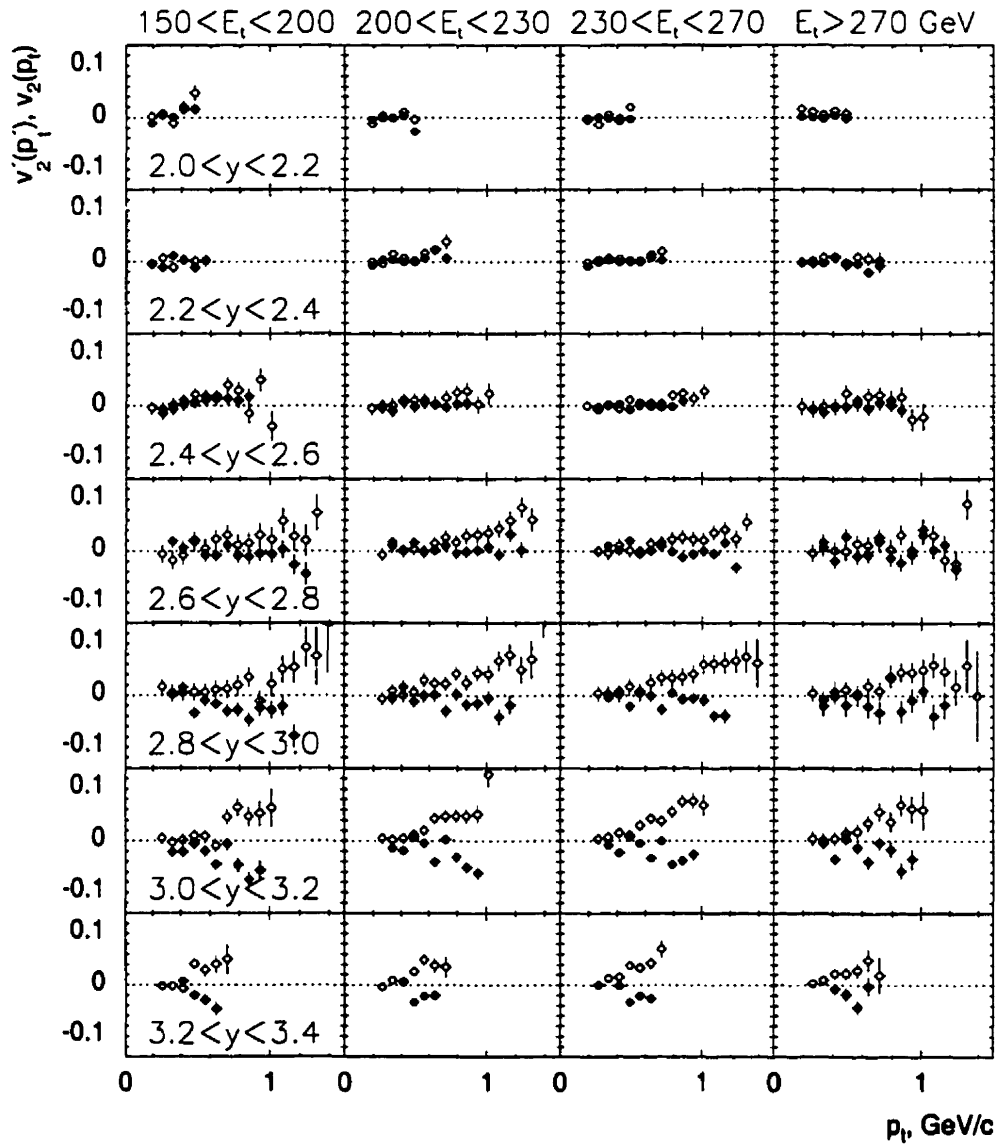


Figure 6.5:  $v'_2(p'_t)$  (solid circles) and  $v_2(p_t)$  (open circles) of protons for various rapidity bins and collision centralities.

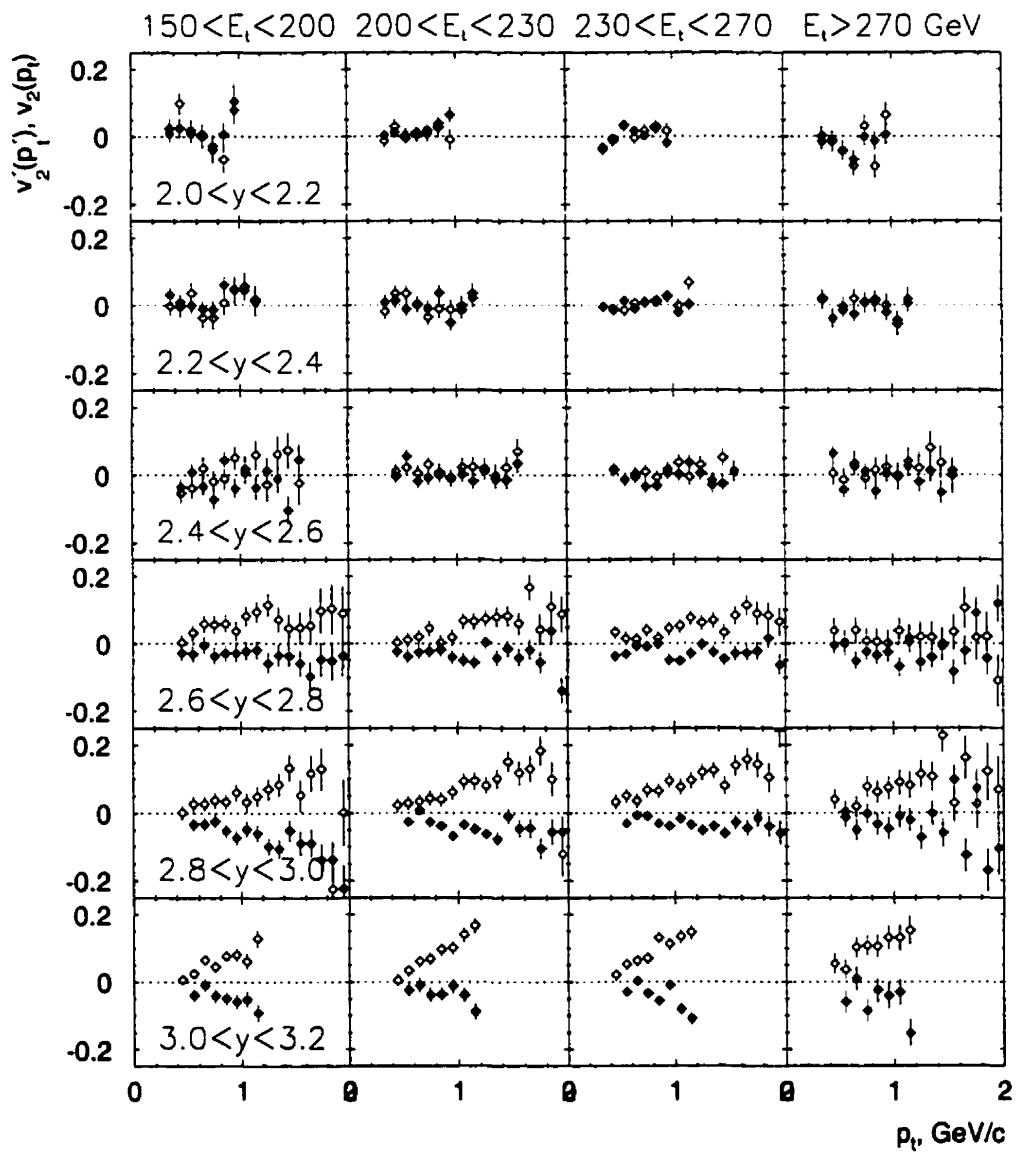


Figure 6.6:  $v'_2(p'_t)$  (solid circles) and  $v_2(p_t)$  (open circles) of deuterons for various rapidity bins and collision centralities.

The error bars shown for  $v'_2(p'_t)$ -dependence represent statistical errors and systematic errors estimated by the Fourier coefficients of the  $\sin 2\phi'$  term. Other sources of systematic errors include: i) possible particle misidentification ( $\sim 5\%$ ); ii) the uncertainty in the determination of the reaction plane resolution ( $\sim 15\text{-}20\%$  for all particle species); iii) the uncertainty in correction for finite detector occupancy (3-5% at the low  $p_t$  region and negligible at  $p_t > 0.6 - 0.8$  GeV/c).

These results indicate that the orientation of the major axis of the elliptic deformation of the flow tensor depends on rapidity, with in-plane preferential emission observed at rapidities closer to mid-rapidity, and out-of-plane emission observed near the projectile rapidity for all collision centralities.

### $\langle v'_2 \rangle$ as a function of $y$

The experimental acceptance provides us with a limited range in the transverse momentum for both protons and deuterons. In order to quantitatively study the dependence of  $\langle v'_2 \rangle$  on rapidity, we need to compensate for the missing  $p_t$ -coverage. The mean  $v'_2$  at a fixed rapidity is given by

$$\langle v'_2 \rangle = \frac{1}{N_0} \int \frac{d^2 N}{dp'_x dp'_y} \frac{p'^2_x - p'^2_y}{p'^2_x + p'^2_y} dp'_x dp'_y \quad (6.1)$$

$$= \frac{1}{N_0} \int \frac{d^2 N}{p'_t dp'_t d\phi'} \cos 2\phi' p'_t dp'_t d\phi' \quad (6.2)$$

$$= \frac{1}{N'_0} \int \frac{dN'}{dp'_t} v'_2(p'_t) dp'_t \quad (6.3)$$

The  $d^2 N/dp'_x dp'_y$  distribution of protons has been shown to be well described by a thermal distribution with its center shifted from origin due to directed flow [35]:

$$d^2 N/dp'_x dp'_y \propto m'_t \exp\left(-\frac{m'_t}{T_B}\right). \quad (6.4)$$

where  $T_B$  is the inverse slope parameter. The proton inverse slope parameters  $T_B$  for various rapidities have been determined before [98] and are summarized in Table 6.2.

Table 6.2: Inverse slope parameters  $T_B$  of protons (from [98]).

Rapidity	$T_B$ (MeV)	Rapidity	$T_B$ (MeV)
2.2	$225.75 \pm 6.51$	2.8	$130.52 \pm 0.28$
2.3	$216.73 \pm 2.82$	2.9	$117.54 \pm 0.29$
2.4	$190.08 \pm 1.87$	3.0	$102.75 \pm 0.32$
2.5	$171.26 \pm 0.84$	3.1	$85.42 \pm 0.39$
2.6	$151.78 \pm 0.44$	3.2	$86.67 \pm 1.43$
2.7	$139.81 \pm 0.30$	3.3	$47.72 \pm 0.84$

In order to parameterize the elliptic shape of the above distribution we introduce an ellipticity parameter  $\varepsilon$ :

$$d^2 N / dp'_x dp_y \propto \sqrt{p_x'^2 + \varepsilon^2 \cdot p_y^2 + m^2} \exp\left(-\frac{\sqrt{p_x'^2 + \varepsilon^2 \cdot p_y^2 + m^2}}{T_B}\right). \quad (6.5)$$

The parameter  $\varepsilon$  quantifies the amplitude of the elliptic deformation of  $d^2 N / dp'_x dp_y$  distribution in the  $y$ -direction compare to the  $x$ -direction. It is equal to unity in the absence of the elliptic deformation. The values of  $\varepsilon$  larger than unity imply a preferred in-plane emission, and  $\varepsilon < 1$  corresponds to the out-of-plane elliptic flow.

Using the inverse slope parameters  $T_B$  determined from the proton  $m_t$ -spectra, we can describe the proton  $v_2'(p'_t)$ -dependence with parameterization given in Eq. 6.5. The results of such calculations are shown in Fig. 6.7. In general, the parameterization describes the data quite well with reasonable values of  $\chi^2$ . The fit is not quite stable in the rapidity bins  $2.0 < y < 2.2$  and  $2.2 < y < 2.4$  due to the small  $p_t$ -coverage and weak signal. The extracted values of proton ellipticity parameter  $\varepsilon$  for different rapidities and collision centralities are presented in Table 6.3. The errors on the fit parameter  $\varepsilon$  are large for rapidities  $2.0 < y < 2.2$ , so we do not use this bin in further

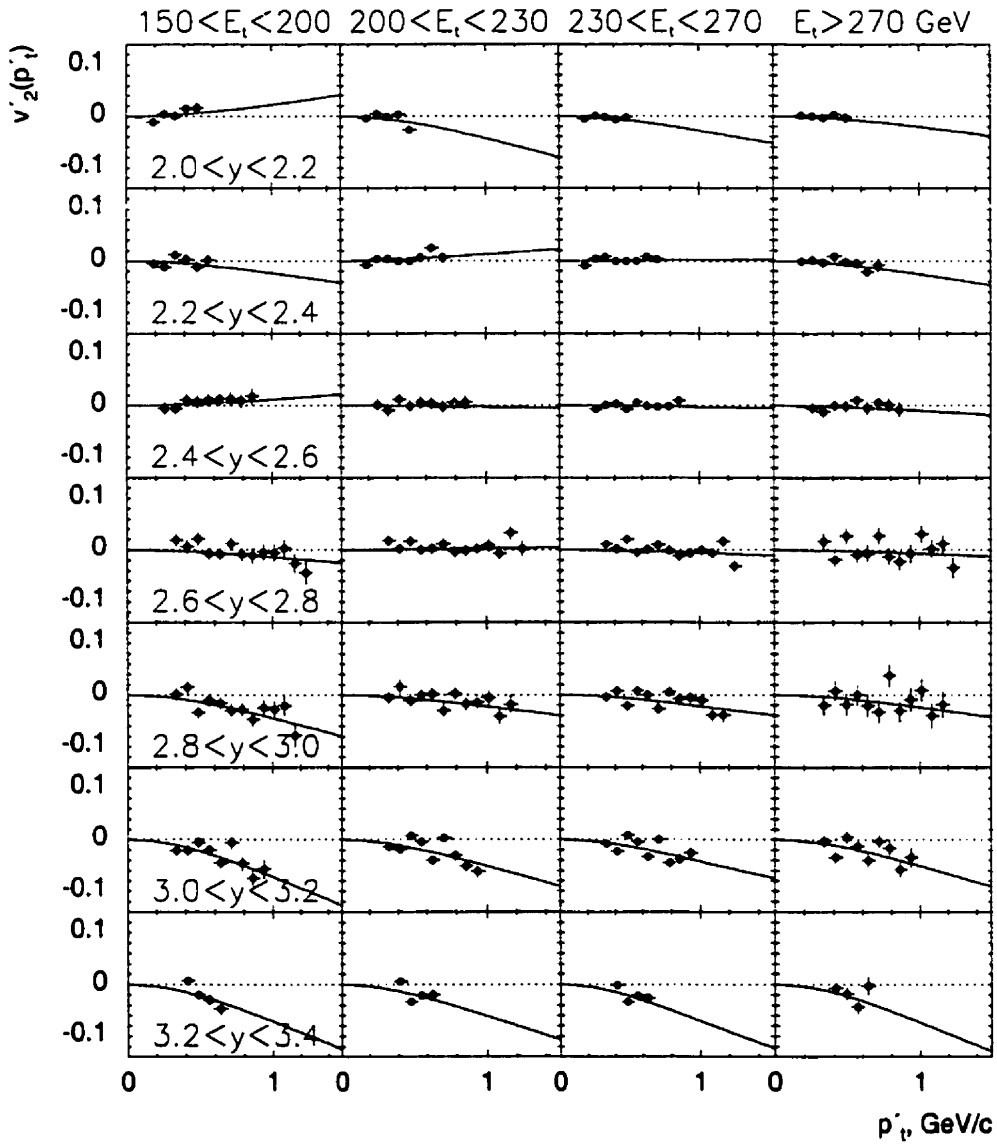


Figure 6.7: Fit of  $v_2'(p_t')$  of protons by a parameterization given in Eq. 6.5.

Table 6.3: Ellipticity parameter  $\varepsilon$  of protons for different rapidities and collision centralities. The errors include the uncertainty in the effective slope parameters used for the spectra extrapolation.

$y$	Ellipticity parameter $\varepsilon$			
	$150 < E_t < 200$	$200 < E_t < 230$	$230 < E_t < 270$	$E_t > 270$ GeV
2.1	$1.085 \pm 0.042$	$0.943 \pm 0.031$	$0.968 \pm 0.025$	$0.999 \pm 0.040$
2.3	$0.993 \pm 0.026$	$1.030 \pm 0.012$	$1.010 \pm 0.007$	$0.978 \pm 0.015$
2.5	$1.023 \pm 0.010$	$1.007 \pm 0.010$	$1.003 \pm 0.006$	$1.000 \pm 0.010$
2.7	$0.992 \pm 0.005$	$1.007 \pm 0.004$	$0.998 \pm 0.003$	$0.999 \pm 0.006$
2.9	$0.973 \pm 0.004$	$0.988 \pm 0.004$	$0.988 \pm 0.003$	$0.990 \pm 0.006$
3.1	$0.968 \pm 0.004$	$0.977 \pm 0.003$	$0.981 \pm 0.003$	$0.979 \pm 0.005$
3.3	$0.984 \pm 0.004$	$0.986 \pm 0.003$	$0.983 \pm 0.003$	$0.985 \pm 0.005$

analysis. The errors include the uncertainty in the effective slope parameters used for the spectra extrapolation. We observe  $\varepsilon > 1$  for rapidities closer to center-of-mass rapidity, and  $\varepsilon < 1$  for protons emitted near projectile rapidities. The amplitude of the elliptic deformation also depends on centrality, with larger deformation observed for more peripheral collisions.

Having extracted the values of  $\varepsilon$ , we can combine the extrapolated particle spectra with obtained  $v'_2(p'_t)$ -dependence to estimate the average  $v_2$  in a given rapidity window. In Fig. 6.8 we present the dependence of  $v'_2$  of protons on rapidity for different centralities of the collision. The amplitude of the Fourier coefficient  $v_2$  for protons estimated in the frame shifted by  $\langle p_x \rangle$  in the direction of the reaction plane depends on rapidity. A change in sign of the proton elliptic flow signal when studied as a function of rapidity is observed. Positive values of  $v'_2$  are measured at the rapidities

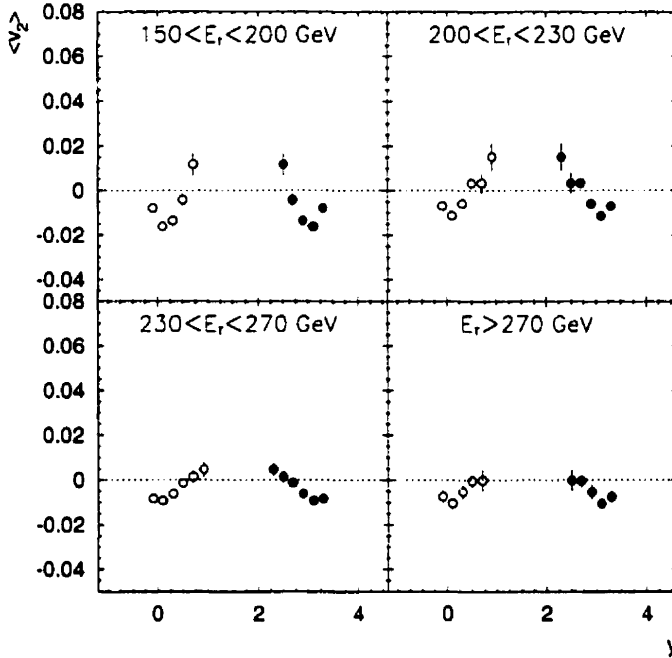


Figure 6.8:  $v_2'$  of protons as a function of rapidity for different collision centralities. The open circles are obtained by reflecting the solid circles around  $y_{cm} = 1.6$ .

close to  $y_{cm}$ , and negative values of  $v_2'$  are measured at projectile/target rapidities. The overall change in the magnitude over the studied rapidity region is maximum for more peripheral collisions ( $\Delta v_2' \approx 0.03$ ). The data also indicate that the shape of  $v_2'(y)$ -dependence is flatter for more central events.

The determination of the mean  $v_2'$  for deuterons is complicated due to non-thermal shape of the deuteron spectra. Deuteron transverse momentum spectra were analyzed in [99]. At beam rapidities deuteron spectra were found to be approximately thermal

with an inverse slope parameter  $T_B$  of about 80 MeV for centralities corresponding to  $150 < E_t < 230$  GeV region, and with slightly lower parameters  $T_B = 60$  MeV (50 MeV) for  $230 < E_t < 270$  GeV ( $E_t > 270$  GeV) centrality regions. Using the deuteron spectra, we can fit the  $v'_2(p'_t)$ -dependence of beam rapidity deuterons with Eq. 6.5. The results of such fit are shown in Fig. 6.9. The comparison of the mean  $v'_2$

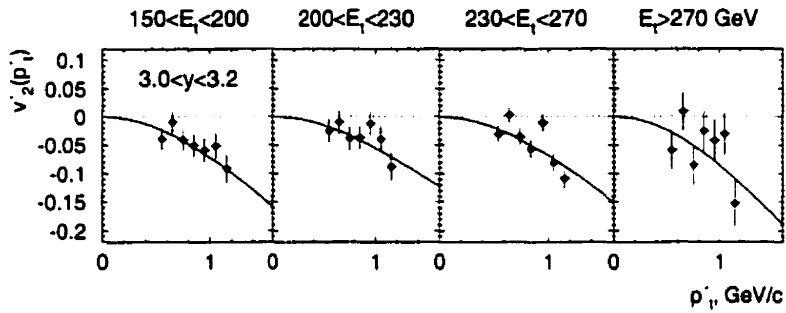


Figure 6.9: Fit of  $v'_2(p'_t)$  of deuterons by a parameterization given in Eq. 6.5.

of beam rapidity protons and deuterons is done in Table 6.4 for different centralities. The values of  $v'_2$  of deuterons are about 1.5 times larger than those of protons.

Table 6.4:  $v'_2$  of protons and deuterons in the rapidity region  $3.0 < y < 3.2$  for different collision centralities.

	$v'_2$ in $3.0 < y < 3.2$ bin			
	$150 < E_t < 200$	$200 < E_t < 230$	$230 < E_t < 270$	$E_t > 270$ GeV
protons	$-0.016 \pm 0.002$	$-0.011 \pm 0.002$	$-0.009 \pm 0.001$	$0.011 \pm 0.002$
deuterons	$-0.022 \pm 0.004$	$-0.016 \pm 0.004$	$-0.016 \pm 0.002$	$-0.015 \pm 0.004$

## 6.2 Discussion

At ultra-relativistic energies, elliptic flow develops in two stages. Early in the collision, the mechanism is similar to that at lower energies. The cold spectator nucleons block the path of participant hadrons emitted from the collision zone. Matter in central rapidity region escapes preferentially orthogonal to the reaction plane, resulting in negative elliptic flow. At a later stage, the spectator nucleons leave the reaction region. The almond-shaped geometry of expanding participant region favors in-plane preferential emission and hence positive elliptic flow. The orientation of the final azimuthal asymmetry thus depends on the ratio between the passage time for removal of shadowing due to spectators and the expansion time. The passage time of projectile and target nuclei of equal mass is given by:

$$t_{\text{passage}} \sim \frac{2R_A}{\gamma\beta_{cm}}, \quad (6.6)$$

where  $R_A$  is the nuclear radius,  $\gamma$  is the Lorentz factor, and  $\beta_{cm}$  is the center-of-mass velocity. The passage time for the low energy collisions is quite long ( $\sim 15.6$  fm/c for Au+Au collisions at 1 A·GeV). At the AGS-SPS energies, it shrinks with the Lorentz factor  $\gamma$ , and for the heaviest systems at the AGS and SPS, the passage times are about 5.4 fm/c at 12 A·GeV and 1.4 fm/c at 160 A·GeV [79]. On the other hand, the characteristic time for the development of expansion depends on the pressure built up in the compression stage  $p$  compared to the energy density  $\epsilon$  [80]:

$$t_{\text{expansion}} \sim \frac{R_A}{\sqrt{\partial p / \partial \epsilon}}. \quad (6.7)$$

Elliptic flow measurements reflect the ratio  $t_{\text{passage}}/t_{\text{expansion}}$  and can therefore be used as a probe for the parameters of the EOS.

Up to now, elliptic flow has been mainly studied in the central rapidity region. An emphasis has been put on the measurements and calculations of the excitation

function, as it is predicted to be sensitive to the stiffness of the equation of state. On the other hand, rapidity dependence of elliptic flow may provide another probe for the reaction dynamics. At the Bevalac energies, the squeeze-out effect extends quite far towards projectile and target spectators and rapidity dependence of elliptic flow is essentially flat at these energies [71]. At higher energies, elliptic flow exhibits stronger dependence on rapidity. In Fig. 6.10 the dependence of proton elliptic flow

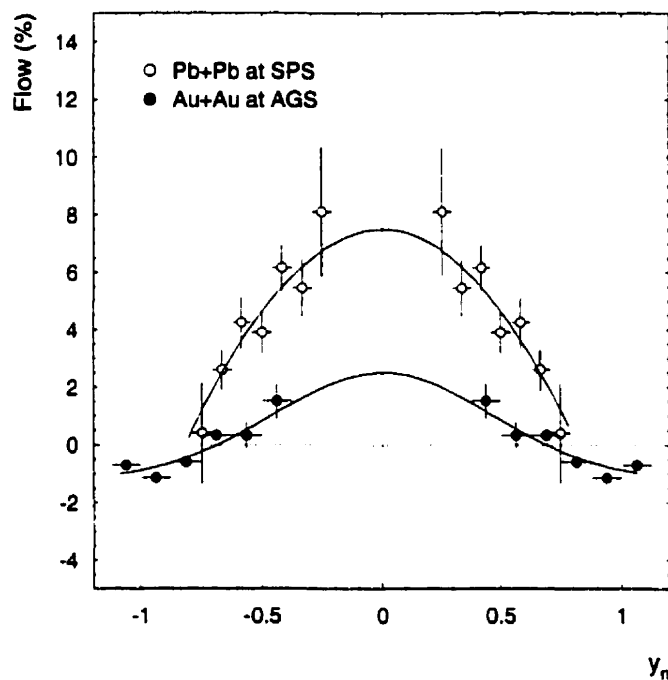


Figure 6.10: Elliptic flow of protons as a function of normalized rapidity for 158 A·GeV Pb+Pb collisions (open circles) and 11.5 A·GeV/c Au+Au collisions (solid circles). The points are reflected around mid-rapidity. The curves are to guide the eye.

signal on normalized rapidity  $y_n = (y - y_{cm})/y_{cm}$  is compared for 158 A·GeV Pb+Pb data measured by NA49 collaboration [41] and our 11.5 A·GeV/c Au+Au data. El-

liptic flow is larger at SPS energies in mid-rapidity region, and of similar amplitude at rapidities close to projectile/target rapidities. The measurements of NA49 collaboration are not corrected for directed flow, but its influence is significantly lower at SPS energies. The maximum amplitude of directed flow at these energies is about 10% [41], whereas at the AGS it may reach up to 50% (see [35] and Fig. 6.4). The data also indicate that the shape of  $v_2(y)$ -dependence is narrower at higher energies.

The trend exhibited by experimental data may be qualitatively understood as the following. A weak dependence of elliptic flow on rapidity at low (Bevalac) energies is a consequence of the long passage time. The spectator nucleons stay near the participant region long enough to block all the particles emitted from the participant region. At high (SPS) energies, the spectators leave the participant region after a short time. The emitted particles do not interact with the spectator nucleons and acquire positive elliptic flow which reflects the geometry of the participant region. Particles with higher longitudinal velocities are less sensitive to the pressure build-up in the hot central zone which results in a decrease of in-plane elliptic flow with rapidity. The AGS is in the range where initial squeeze-out due to shadowing by spectators competes with later developed in-plane flow. In the central region, the pressure gradients are largest and initial squeeze-out transforms into in-plane elliptic flow. Particles with high longitudinal velocities are closer to spectators and experience more effective blocking. The result is a change of sign of elliptic deformation from the in-plane flow for mid-rapidity particles to the out-of-plane flow for beam/target rapidity particles.

Another interesting feature of the data is the change in shape of the rapidity dependence of elliptic flow. Our data indicate that the dependence is flatter for more central collisions. On the other hand, it is narrower for higher beam energies. Since elliptic flow is sensitive to the difference of the early and late pressures, the dependence of the elliptic flow on rapidity may be useful in studying the transient

pressure in the reaction.

### 6.2.1 RQMD comparison

One of the semi-classical transport models widely used in describing relativistic heavy ion collisions is the Relativistic Quantum Molecular Dynamics (RQMD) [50, 51]. RQMD is constructed as a Monte-Carlo code which generates complete events for a given system and beam energy. It combines the classical propagation of all hadrons with the string and resonance excitations. The model includes a finite formation time for produced particles, rescattering of secondaries and modified dispersion relations for baryons. RQMD may be run in two modes. In *mean field* mode, the effective masses of baryons are generated by introducing Lorentz-invariant quasi-potentials into the mass-shell constraints for the momenta which simulate the effect of mean fields. There are no such potential-type interactions in *cascade* mode of RQMD.

A total of  $\sim 63,000$  Au+Au events with initial beam momentum of  $11.5 \text{ A}\cdot\text{GeV}/c$  were simulated using the RQMD v2.3 event generator. The RQMD was run in cascade mode for  $\sim 43,000$  events, and in mean field mode for  $\sim 20,000$  events. The generated events were divided into four centrality bins based on a transverse energy cut that simulated the centrality definition in the experiment.

RQMD treats the reaction products as unbound, including the projectile and target. As a result, the calculated proton sample contains a large number of particles in the beam rapidity region, which come from the target and projectile spectators and introduce unphysical distortions to the final particle distributions. The bulk of such spectator nucleons can be removed from the analysis by restricting the sample to the nucleons that had at least one interaction during the reaction. This is illustrated in Fig. 6.11, where we compare  $dN/dy$  distribution in the RQMD v2.3 cascade calculation for the sample of all protons present in the model and the proton distribution

after removing the non-interacting spectator protons. In the present analysis, the

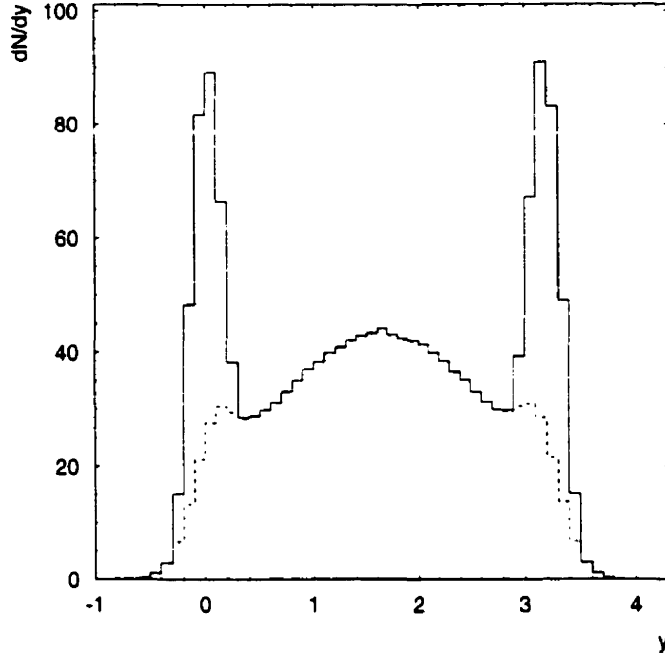


Figure 6.11: RQMD 2.3 (Cascade) rapidity distributions of participant and spectator protons for  $\sigma_{top}/\sigma_{geo}=7\%$ . The solid histogram is the total proton distribution, and the dashed histogram is the proton distribution after removing the non-interacting spectator protons.

non-interacting protons were removed from the calculated sample.

The mean field mode of RQMD v2.3 has been shown to describe the experimental dependence of  $\langle p_x \rangle$  on rapidity rather well [35]. In our analysis, we first estimate the  $\langle p_x \rangle$ -values in  $\Delta y=0.1$  rapidity bins and centrality regions corresponding to the ones chosen for the data. Then, we analyze the second coefficient in the Fourier expansion of the particle azimuthal distributions in the frame shifted by  $\langle p_x \rangle$  in the direction of the reaction plane.

The results of the calculations of the RQMD v2.3 model run in cascade mode are compared with the experimental data for protons in Fig. 6.12. The calculated values of  $v'_2$  rise almost linearly with transverse momentum. The amplitude of elliptic flow signal is larger for more peripheral collisions. The model predicts the maximum in-plane flow for rapidities close to mid-rapidity. The calculated flow signal smoothly decreases with rapidity and is almost absent at beam rapidities. Contrary to the experiment, no change of sign of  $v'_2$  with rapidity is seen in the calculation. The model seems to over-predict the experimental values of  $v'_2$  in all rapidities bins.

The proton experimental  $v'_2(p'_t)$ -dependence is also compared with calculations of the RQMD v2.3 model run in mean field mode (Fig. 6.13). Similar to the cascade mode calculations, the maximum in-plane flow is observed at rapidities close to mid-rapidity and more peripheral events. However, the magnitude of the in-plane flow is smaller compared to the cascade mode, and similar to the experimental data, the flow is almost absent at rapidities around  $y = 2.7$ . Negative values of  $v'_2$  are observed for rapidities  $y > 2.8$  for all centrality regions. The  $p_t$ -dependence at those rapidities seems to be somewhat different than that of the experimental data, with fast decrease to negative  $v'_2$ 's in the low  $p_t$  region, and constant or rising  $v'_2$ 's at higher transverse momenta. The overall agreement with the data is better for the mean field version of the RQMD, compared to the cascade calculations.

A clearer picture of the rapidity dependence of the calculated elliptic flow signal is obtained by plotting the mean values of  $v'_2$  as a function of rapidity. In Fig. 6.14 we compare the experimental data to the calculations of RQMD v2.3 run in cascade and mean field modes. Both codes predict in-plane elliptic flow in the mid-rapidity region of the order of 2%, with smaller magnitude observed for more central collisions. However, the predicted functional dependence of  $v'_2$  on rapidity is different. Cascade calculations exhibit smoother dependence on rapidity, with almost no negative values of  $v'_2$  predicted at beam/target rapidities. Mean field calculations, on the other hand,

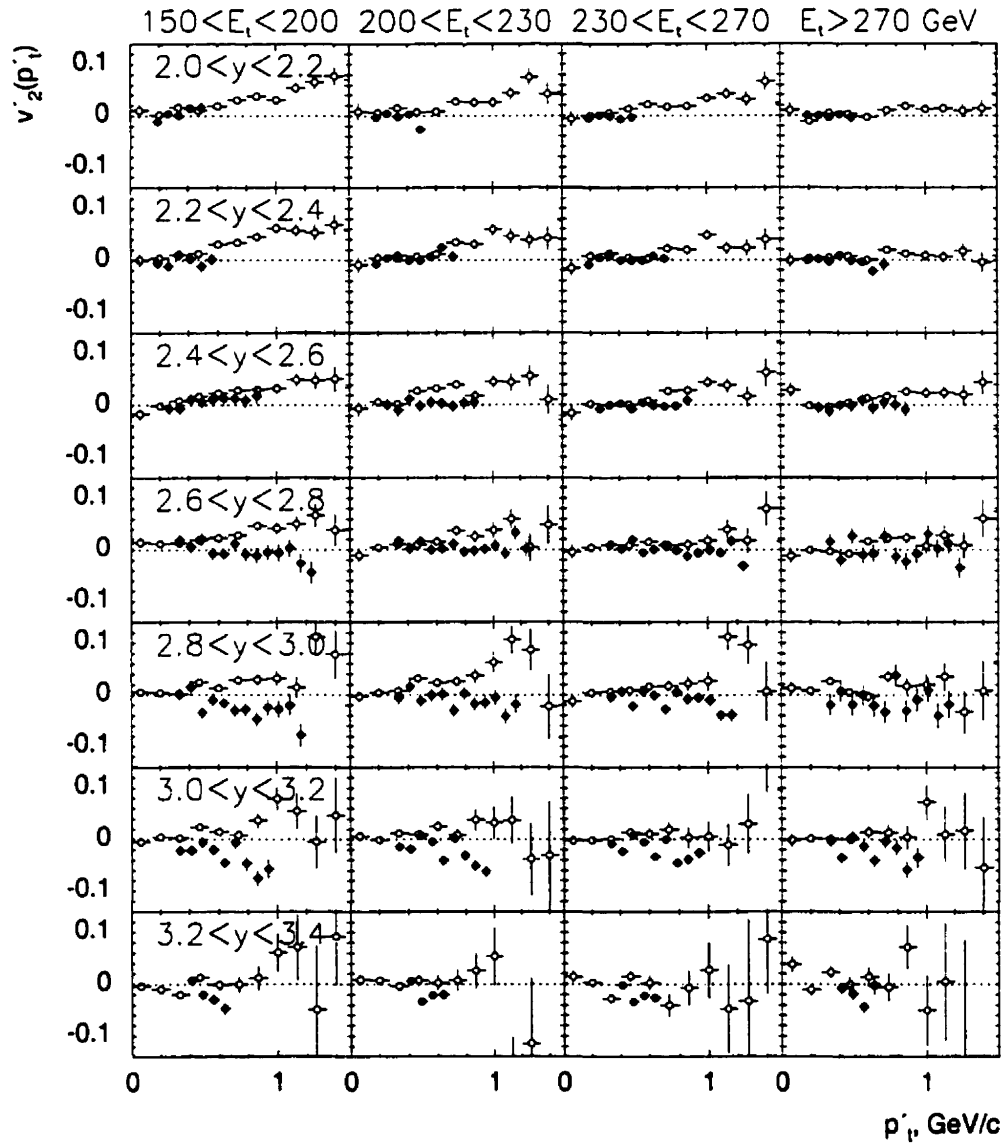


Figure 6.12: Comparison of proton  $v_2'(p'_t)$  data (solid circles) with calculations of RQMD v2.3 run in cascade mode (open circles).

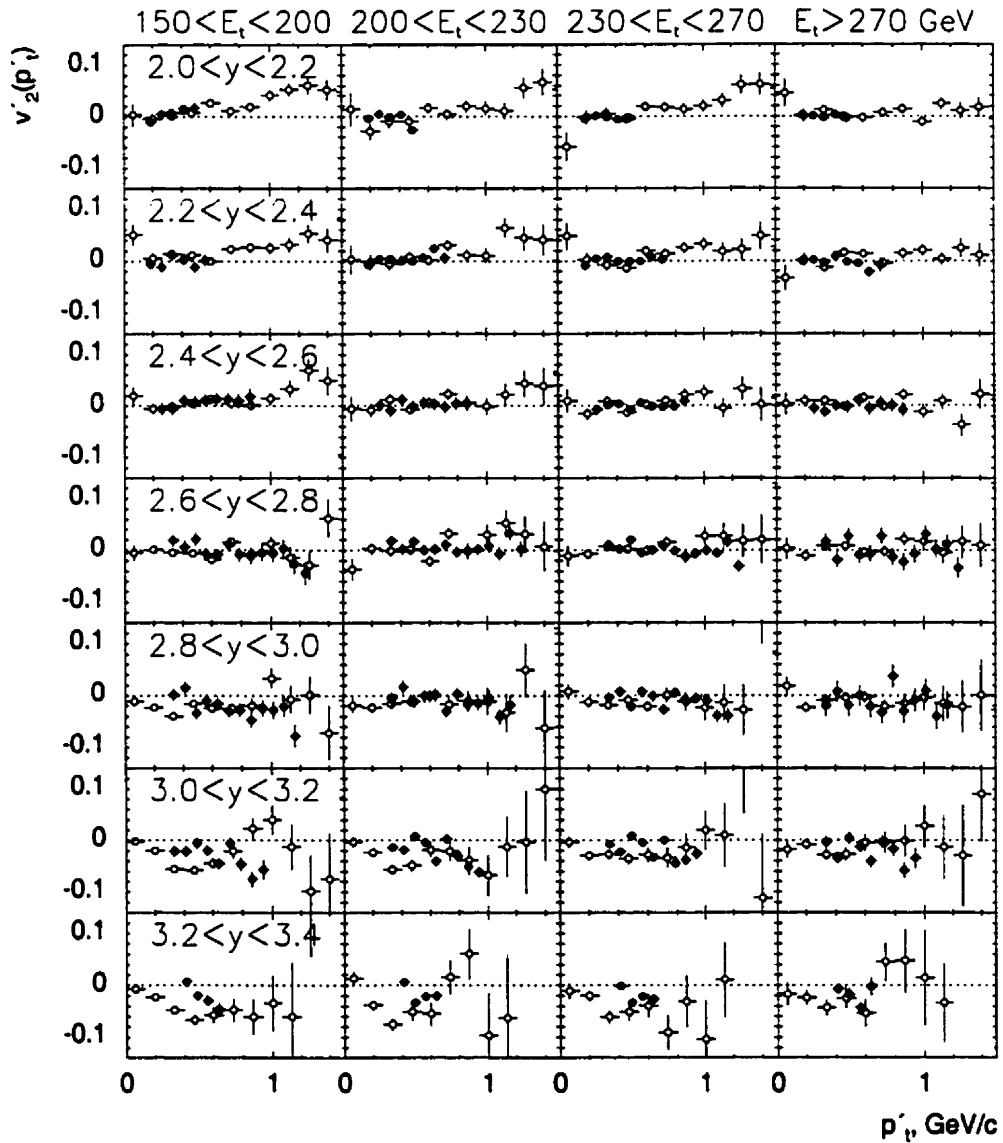


Figure 6.13: Comparison of proton  $v_2'(p_t')$  data (solid circles) with calculations of RQMD v2.3 run in mean field mode (open circles).

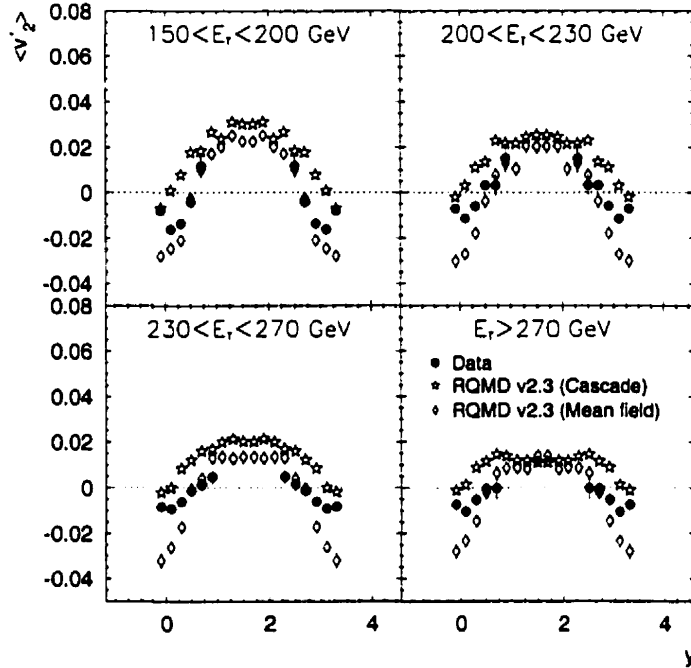


Figure 6.14: Comparison of proton  $v'_2(y)$  data (solid circles) with calculations of RQMD v2.3 run in cascade mode (open stars) and same model run in mean field mode (open diamonds). Both the data and the calculations are reflected around  $y_{cm} = 1.6$ .

more closely follow the data, especially for more peripheral events. The dependence is essentially flat for rapidities  $0.8 < y < 2.4$ , but falls off at higher rapidities, and crosses zero at  $y \approx 2.7 - 2.8$  ( $0.4 - 0.5$ ) with negative values of  $v_2 \approx -0.03$  observed at beam/target rapidities. The  $v'_2(y)$ -dependence flattens out with centrality, following the behaviour shown by the data.

### 6.2.2 Coalescence afterburner

The RQMD does not contain the formation of nuclear bound states (e.g., deuterons) dynamically. The formation probability of composite particles can be calculated from the nucleon distributions at freeze-out. The phase space coalescence approach [100, 101] is based on projecting a final nucleon phase space distribution on cluster wave function via the Wigner-function method. A coalescence afterburner program considers all possible pairs of neutrons ( $i_n$ ) and protons ( $j_p$ ) generated by the RQMD. The number of deuterons is given by

$$dN_d = \frac{1}{2} \frac{3}{4} \left\langle \sum_{i_n, j_p} \rho_d^W(\Delta \mathbf{x}, \Delta \mathbf{p}) \right\rangle d^3(p_{i_n} + p_{j_p}), \quad (6.8)$$

where  $\rho_d^W$  is the Wigner density of the Hulthén deuteron wave function. The distance vectors in position  $\Delta \mathbf{x}$  and momentum  $\Delta \mathbf{p} = \frac{1}{2}(\mathbf{p}_{i_n} - \mathbf{p}_{j_p})$  space are taken at equal time in the two-nucleon rest frame (c.m.s) immediately after both nucleons have frozen out. The factors  $\frac{1}{2}$  and  $\frac{3}{4}$  take into account isospin projection and spin averaging.

The nucleons generated by the RQMD v2.3 in cascade and mean field modes were fed into the coalescence afterburner and the resultant phase space distribution of deuterons was analyzed with respect to the reaction plane using the same method as before.  $v'_2(p'_t)$  of deuterons calculated by the coalescence model combined with the cascade RQMD is compared to the data in Fig. 6.15. The results of such comparison are very similar to those obtained for protons. Positive values of calculated  $v'_2$  are observed for almost all rapidity bins and centralities. The amplitude of elliptic flow signal is smaller for higher rapidities and larger for more peripheral collisions.

A different behaviour is observed for deuterons constructed using nucleons from the mean field version of the RQMD (Fig. 6.16). The calculation shows a change of sign of elliptic flow characteristic to the experimental data for both protons and

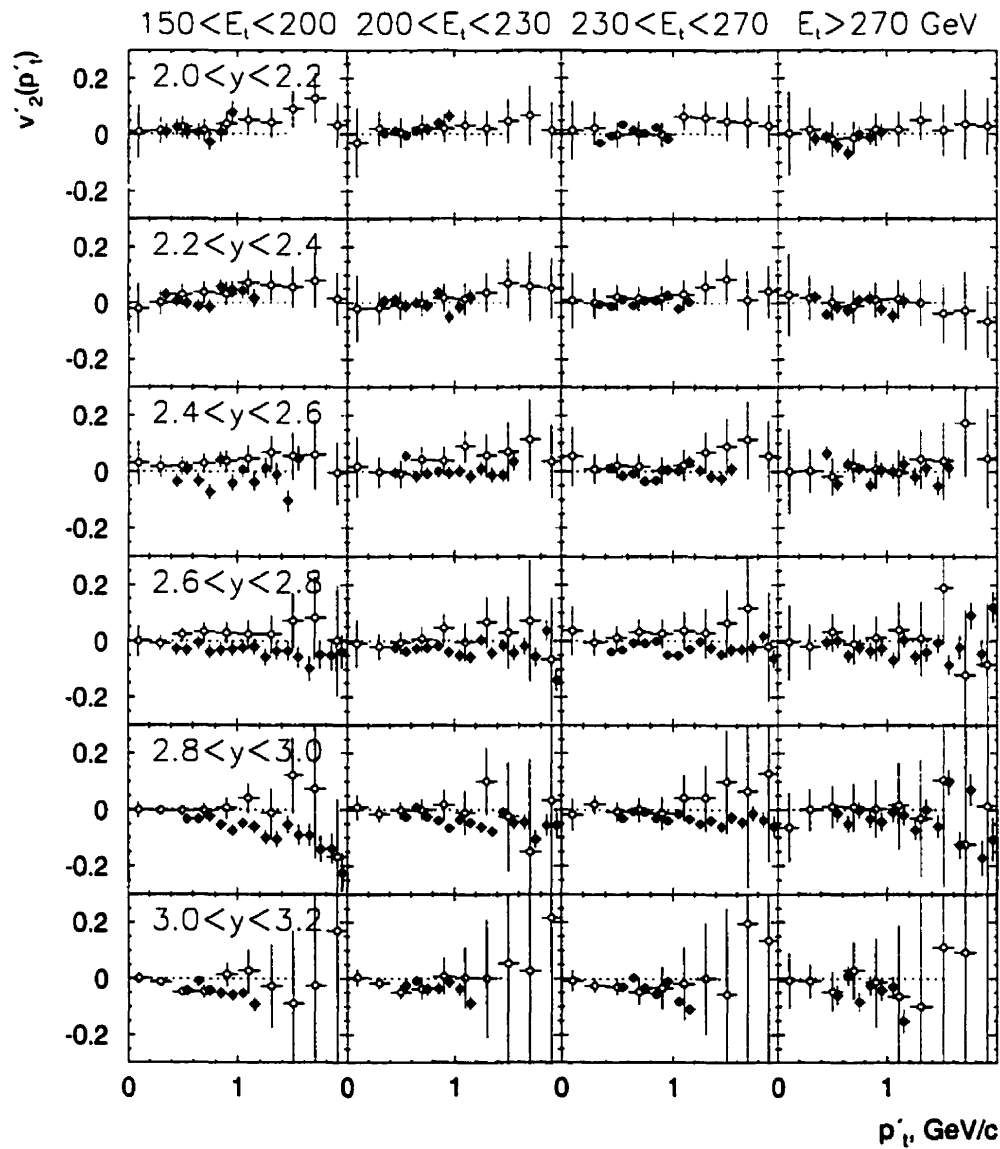


Figure 6.15: Comparison of deuteron  $v_2'(p_t')$  data (solid circles) with calculations of coalescence model combined with the RQMD v2.3 event generator run in cascade mode (open circles).

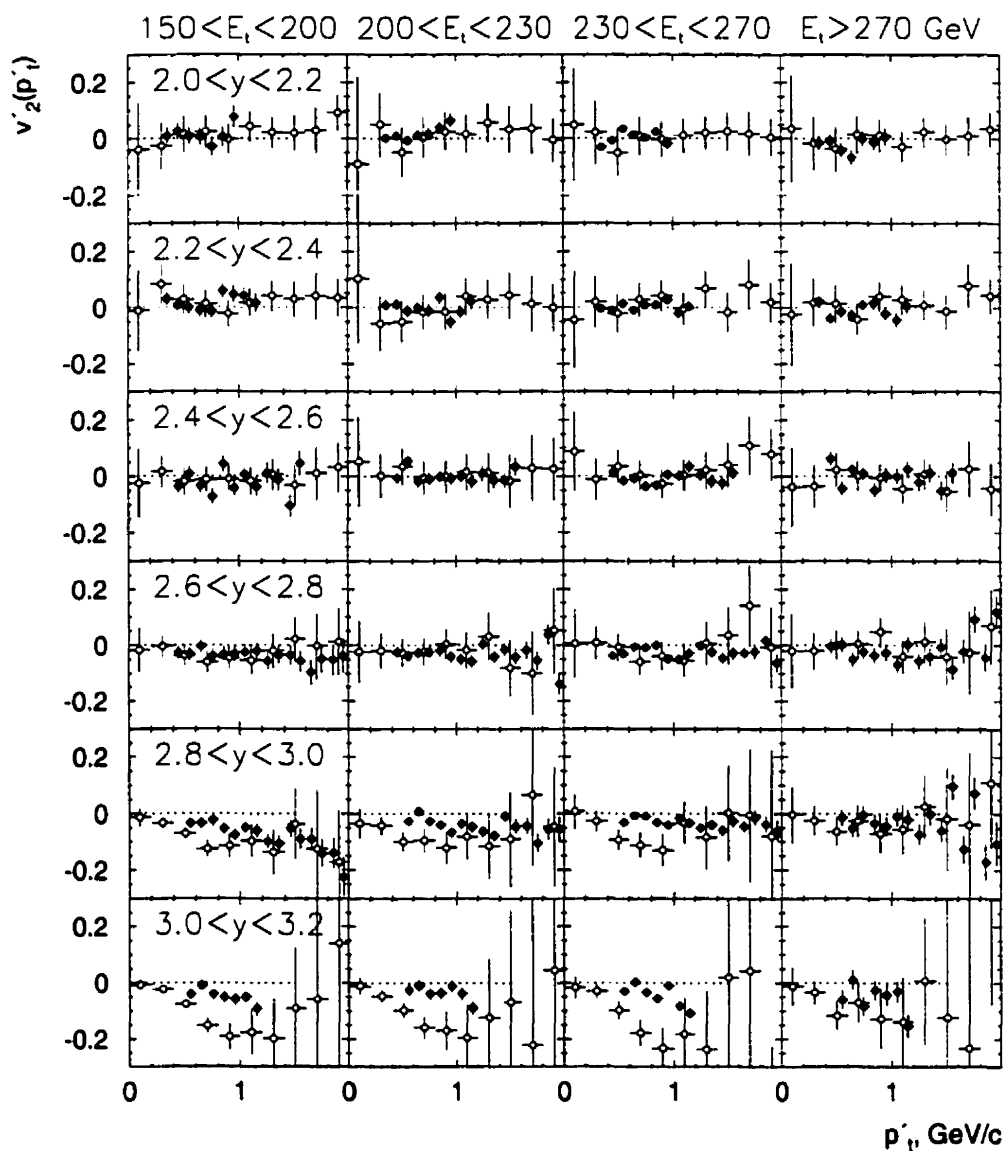


Figure 6.16: Comparison of deuteron  $v_2'(p_t')$  data (solid circles) with calculations of coalescence model combined with the RQMD v2.3 event generator run in mean field mode (open circles).

deuterons. It seems to over-predict the amplitude of out-of-plane flow in the beam rapidity region.

The rapidity dependence of the deuteron elliptic flow signal is shown in Fig. 6.17 for coalescence model combined with cascade and mean field modes of RQMD. In

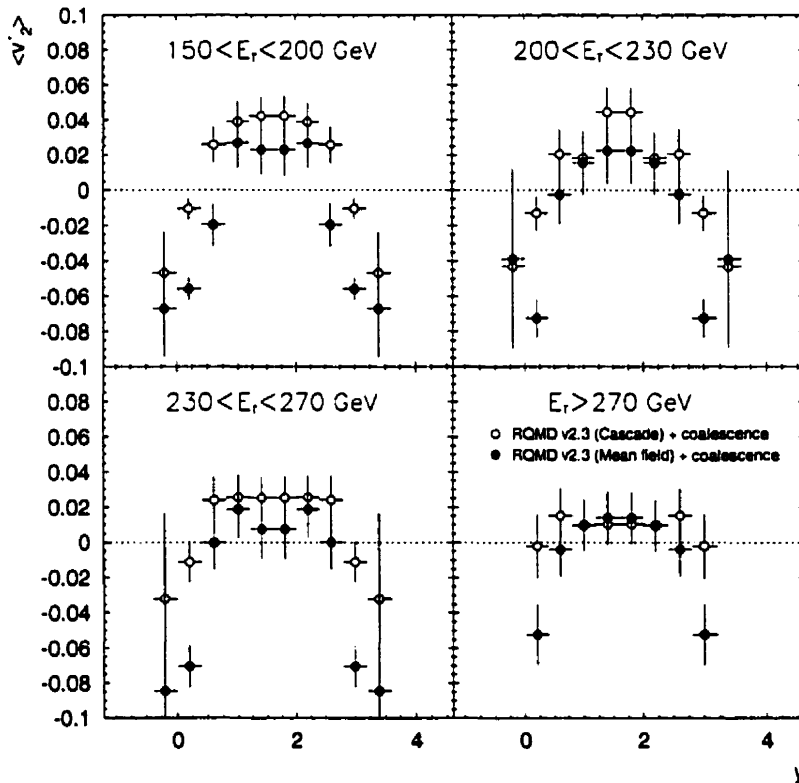


Figure 6.17:  $v_2'(y)$  for deuterons as calculated by the coalescence model combined with RQMD v2.3 run in cascade mode (open circles) and mean field mode (solid circles).

the mid-rapidity region, the amplitude of predicted elliptic flow signal of deuterons is approximately equal to that of protons. At the beam/projectile rapidities, however,

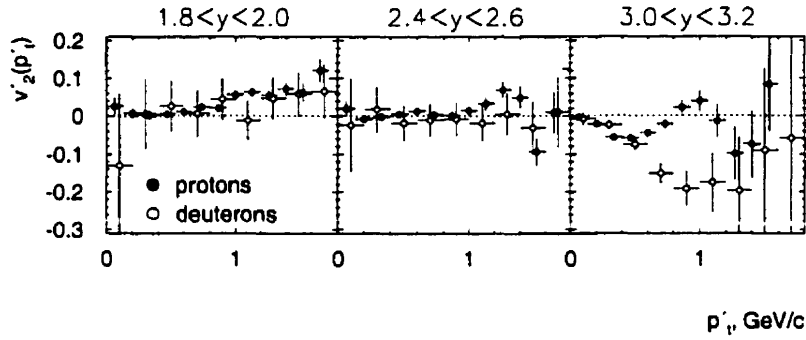


Figure 6.18:  $v_2'(p_t)$  of protons (open circles) and deuterons (solid circles) in the coalescence model combined with RQMD (mean field) v2.3 event generator.

elliptic flow of deuterons is about two times larger than that of protons, similar to the behaviour observed for the directed flow calculations [36].

The calculated transverse momentum dependence of  $v_2'$  of protons and deuterons obtained from the mean field RQMD event generator is shown in Fig. 6.18 for three rapidity bins and centrality region  $150 < E_t < 200$  GeV. As one can see, in the rapidity bins  $1.8 < y < 2.0$  and  $2.4 < y < 2.6$  the model exhibits an approximately linear dependence of  $v_2'$  on  $p_t'$  similar to that of experimental data. The elliptic flow of deuterons is of approximately equal magnitude as the proton signal. At beam rapidity  $3.0 < y < 3.2$ , however, the model shows a different dependence, with initial decrease of  $v_2'$ -values up to  $p_t' \approx 0.3$  GeV/c for protons and  $p_t' \approx 0.8$  GeV/c for deuterons, and subsequent rise at higher transverse momentum. The amplitude of the deuteron elliptic flow signal is larger than that of protons at high transverse momenta. This peculiar behaviour may be explained by considering the  $p_t$ -dependence of the calculated directed flow signal. In Fig. 6.19 we show the transverse momentum dependence of the first Fourier coefficient  $v_1$  quantifying the directed flow for protons and deuterons as calculated by the same model. Directed flow is absent

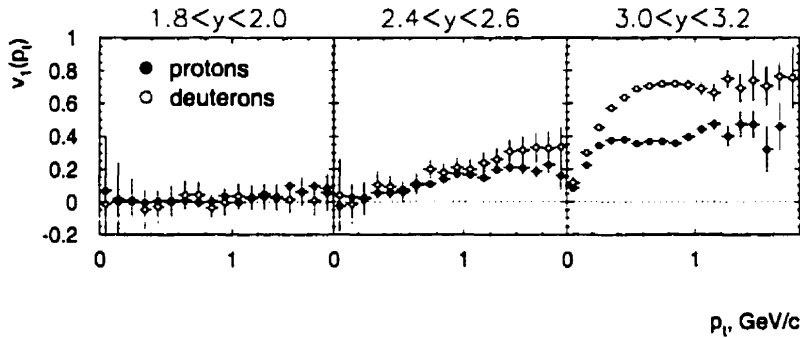


Figure 6.19:  $v_1(p_t)$  of protons (open circles) and deuterons (solid circles) in the coalescence model combined with RQMD v2.3 event generator.

in the rapidity bin  $1.8 < y < 2.0$  and does not affect the elliptic flow component. At rapidities  $2.4 < y < 2.6$ ,  $v_1$  depends linearly on the transverse momentum, in accordance with the experimental data and the transversely moving thermal source model [35]. This linear dependence allows to decouple the directed flow component from the elliptic flow measurements by performing an analysis in the frame shifted by  $\langle p_x \rangle$ . In the beam rapidity region  $3.0 < y < 3.2$ , the mean field version of the RQMD v2.3 event generator predicts a rapid rise of  $v_1$  in the low  $p_t$  region, and rather flat  $v_1(p_t)$ -dependence for high transverse momenta. This behaviour is very different from a linear dependence seen in the data (see Fig. 6.4 and Fig. 2.9). The over-prediction of negative values of  $v_2'$  in the low  $p_t'$  region compared to the data may come from the over-prediction of the amount of directed flow present in the model. In addition, due to flatness of the directed flow signal at high transverse momenta it is difficult to decouple the directed and elliptic flow components.

In summary, the Relativistic Quantum Molecular Dynamics model explains general features exhibited by the experimental data. The mean field mode of the RQMD has been found to provide a better overall description of the experimental data com-

pared to the pure cascade mode. However, an improvement in describing the functional dependences of directed and elliptic flows is needed.

### 6.2.3 Elliptic flow and collective expansion

The influence of the radial collective flow expansion on the elliptic flow was first considered for Au+Au collisions at 600 A·MeV [102]. The transverse mass and rapidity distributions of the particles emitted into mid-rapidity were analyzed in a model where a radial flow velocity  $\beta_r$  is superimposed on a locally thermalized velocity distribution according to the blast-wave scenario [19]. Instead of fitting the emitted particles globally, the spectra were fitted for particles emitted into bins in the azimuthal angle  $\phi'$  relative to the reaction plane. The upper panel of Fig. 6.20 taken from [102] shows deuteron transverse mass spectra at  $\phi' = 0^\circ$  and  $\phi' = 90^\circ$  fitted with Eq. 2.5. In the lower panel the fitted values for  $\beta$  and  $T$  of deuterons are shown as a function of emission angle relative to the reaction plane,  $\phi'$ , for three different multiplicity bins. The apparent temperatures  $T$  were found to be independent of the azimuthal angle, whereas the radial flow velocity was shown to modulate with azimuthal angle with a functional form  $\beta_r(\phi') = \beta_0 - \Delta\beta \cos 2\phi'$ . Larger radial flow velocities were found for the out-of-plane emission of the particles. The term “in-plane retardation” of the radial expansion was introduced.

In this section we perform a similar analysis of the proton  $m_t$  spectra in Au+Au collisions at 11.5 A·GeV/c. The radially symmetric parameterization of Eq. 2.5 is valid only for low (Bevalac) energies. At the AGS energies, the longitudinal and transverse radial expansions are treated separately, thus we study the transverse expansion velocity as a function of the azimuthal angle using a phenomenological approach described in section 2.1.4.

In the frame shifted in the direction of the reaction plane by  $\langle p_x \rangle$ , the transverse

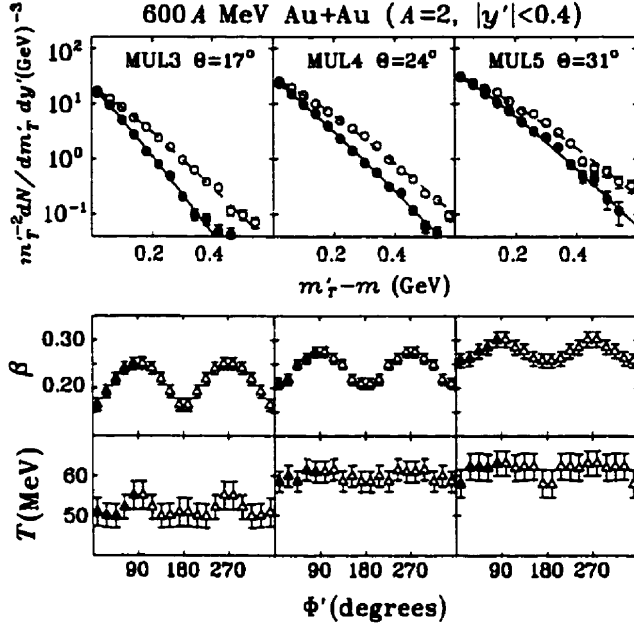


Figure 6.20: Deuteron mass spectra at  $\phi' = 0^\circ$  and  $\phi' = 90^\circ$  fitted with Eq. 2.5 (upper panel) and fit parameters  $\beta, T$  over the complete range of  $\phi'$  (lower panel). The open symbols shown in the lower panel were generated by reflection of the closed symbols. (From [102]).

mass spectrum of particles getting a boost from the radial flow is given by

$$\frac{dN}{m_t' dm_t'} \sim \int_0^R r dr m_t' I_0 \left( \frac{p_t' \sinh \rho}{T_B} \right) K_1 \left( \frac{m_t' \cosh \rho}{T_B} \right), \quad (6.9)$$

where  $\rho = \tanh^{-1} \beta_t(r)$  is the boost angle. We choose the velocity profile  $\beta_t(r)$  of the linear form:

$$\beta_t(r) = \beta_t^{max} \left( \frac{r}{R} \right), \quad (6.10)$$

where  $R$  is the freeze-out radius of the system, and  $\beta_t^{max}$  is the maximum surface velocity. The freeze-out radius of the system can be determined by the Hanbury-Brown-Twiss interferometry. The analysis of the three-dimensional proton-proton

correlation function using the E877 data [103] estimated the transverse proton source size to be 4.75 fm. Similar to the results of [102], we find that when  $T_B$  is used as a free parameter, it shows little or no variation with the azimuthal angle. On the other hand, in such phenomenological analysis the transverse spectra may be described by a wide range of  $(T_B, \beta_t)$  pairs [23]. We decided to constrain the temperatures at values given by a simple thermal model:

$$T_B(y) = \frac{T}{\cosh(y - y_{cm})}, \quad (6.11)$$

where  $T$  is the source temperature, which was chosen to be 130 MeV. The surface velocity  $\beta_t^{max}$  and normalization constant are then the only free parameters in the fitting of the transverse mass spectra with Eq. 6.9.

In order to obtain better statistics, the particle's azimuthal angles with respect to the reaction plane spanning over the full azimuth of  $360^\circ$  were folded in into a single quadrant. This quadrant was divided into the three bins:  $0^\circ < \phi' < 30^\circ$ ,  $30^\circ < \phi' < 60^\circ$ , and  $60^\circ < \phi' < 90^\circ$ . Fig. 6.21 presents proton transverse mass spectra in centrality region  $150 < E_t < 200$  GeV for three rapidity intervals and particles emitted into three bins in the azimuthal angle  $\phi'$ . Also shown are the results of the the  $\chi^2$ -minimized fit using Eq. 6.9. As one can see, the obtained parameters  $\beta_t^{max}$  slightly depend on the the reaction plane orientation.

Fig. 6.22 presents the average transverse expansion velocity  $\langle \beta_t \rangle$  plotted as a function of the azimuthal angle  $\phi'$  relative to the reaction plane for three rapidity intervals and different collisions centralities. The average transverse expansion velocity  $\langle \beta_t \rangle$  assuming a linear velocity profile is equal to the half of the maximum surface velocity  $\beta_t^{max}$ . The first three independent points have been reflected three times over the full azimuth and the dependence have been fitted with the form  $\langle \beta_t(\phi') \rangle = \beta_0 - \Delta\beta \cos 2\phi'$ . Similar to the results obtained for the Bevalac energies, the transverse expansion velocity is found to modulate with the orientation of the reaction plane. The shape of

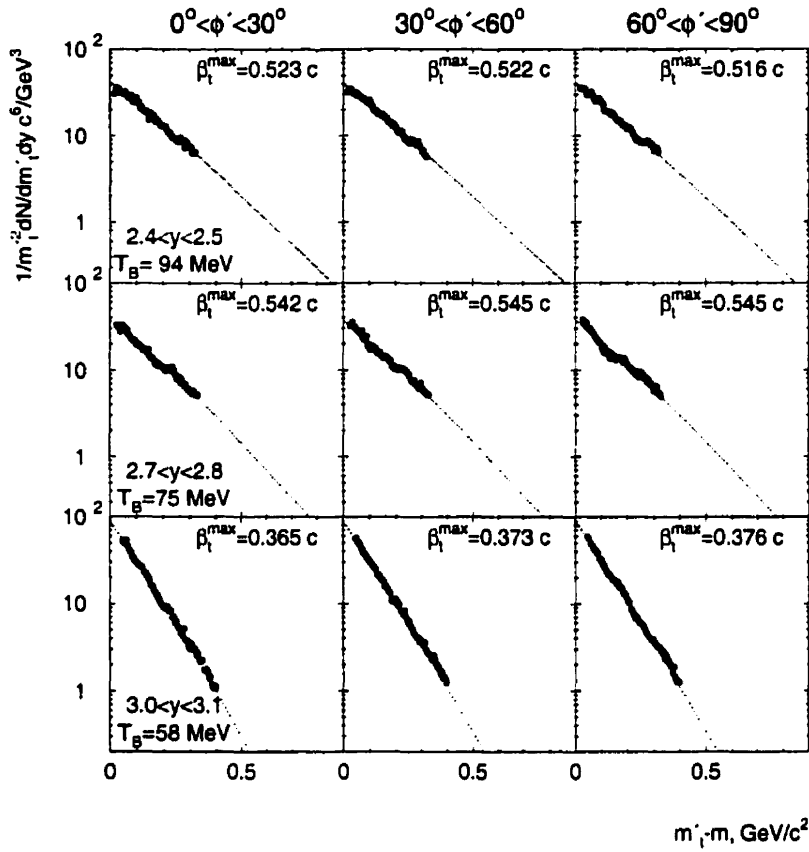


Figure 6.21: Proton transverse mass spectra in centrality region  $150 < E_t < 200 \text{ GeV}$  for three rapidity intervals and particles emitted into three bins in the azimuthal angle  $\phi'$  relative to the reaction plane. The spectra are fitted with Eq. 6.9.

the dependence depends on rapidity. In  $2.4 < y < 2.5$  rapidity region, the maximum transverse expansion velocity is observed for the particles emitted in the direction of the reaction plane. For protons emitted at rapidities close to the beam rapidity ( $3.0 < y < 3.1$ ), the dependence of the transverse expansion velocity on the azimuthal angle is the opposite of that measured in  $2.4 < y < 2.5$  rapidity region: the maximum velocity is observed for the particles emitted out-of-plane. In  $2.7 < y < 2.8$  rapidity

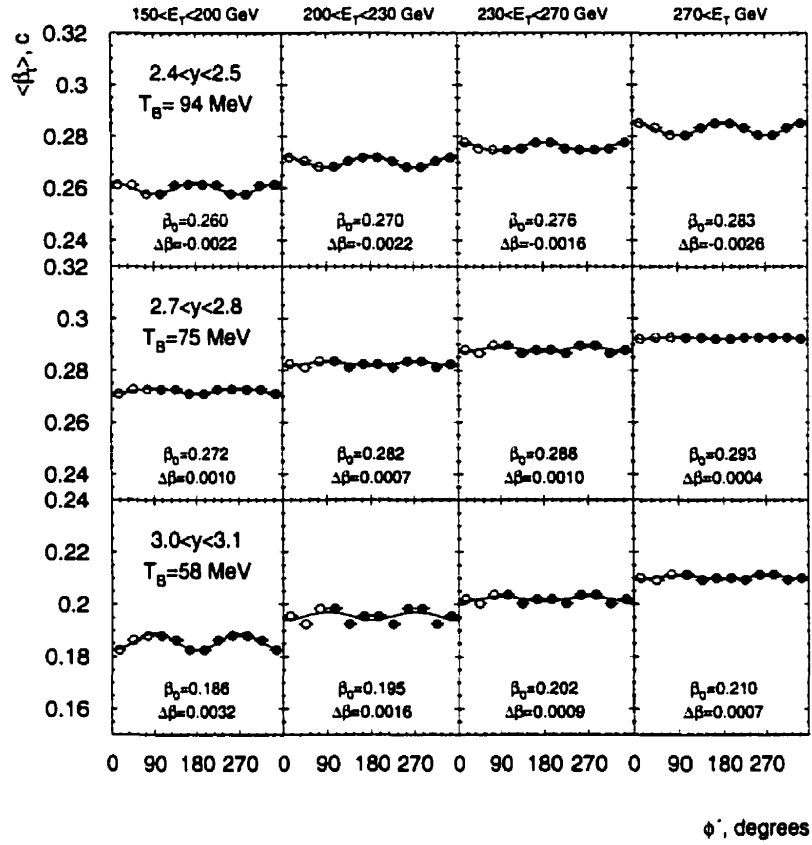


Figure 6.22: Average transverse expansion velocity  $\langle \beta_t \rangle$  as a function of the azimuthal angle  $\phi'$  relative to the reaction plane for three rapidity intervals and different collision centralities. The solid circles are obtained by reflection of the open circles. The dependence is fitted with the form  $\langle \beta_t(\phi') \rangle = \beta_0 - \Delta\beta \cos 2\phi'$ .

region the transverse expansion velocity is essentially independent of the azimuthal angle  $\phi'$ . The mean of the transverse expansion velocity  $\beta_0$  taken over the azimuthal angle increases with centrality but decreases with rapidity, with the minimum observed in the beam rapidity region for the most peripheral collisions. The amplitude of the sinusoidal modulation of the expansion velocity  $\Delta\beta$  decreases with centrality.

It is negative in  $2.4 < y < 2.5$  rapidity region, around zero at  $2.7 < y < 2.8$ , and positive in the beam rapidity region  $3.0 < y < 3.1$ .

The results of this analysis put the elliptic flow measurements into an interesting perspective. The average transverse expansion velocity  $\langle \beta_t \rangle \approx 0.27$  observed at  $2.4 < y < 2.5$  for the velocity profile assumed in Eq. 6.10 implies expansion times of the order of 8 fm/c. As the passage time of the projectile and target is shorter ( $\sim 5$  fm/c) than the expansion time, the transverse expansion proceeds relatively unhindered with maximum velocities observed in the direction of the reaction plane, where the pressure gradients are largest. In the beam rapidity region, the observed transverse expansion velocities are of the same order ( $\langle \beta_t \rangle \approx 0.2$  and  $t_{\text{expansion}} \approx 11$  fm). On the other hand, the emission of particles takes place closer to the spectators in the longitudinal direction. The rescattering of emitted particles in the reaction plane on the cold spectator matter causes a slower in-plane collective expansion compared to the out-of-plane direction, resulting in a squeeze-out effect. The effect should be larger for heavier fragments as their momentum-space density follows the power law relative to the observed nucleon density. The dependence of the expansion velocity on the orientation of the reaction plane also could explain why the elliptic flow depends on the transverse momentum of the emitted particles.

# Chapter 7

## Elliptic Flow of Charged Pions and Kaons

In this chapter we present the measurements of the azimuthal anisotropies of charged pions and kaons produced in Au+Au collisions at 11.5 A· GeV/c. Directed and elliptic components of the flow tensor will be studied as a function of transverse momentum, rapidity, and collision centrality. Similar to proton and deuteron data, we compare the experimental measurements with the mean field and cascade versions of the Relativistic Quantum Molecular Dynamics model.

### 7.1 Experimental Results on Flow of Pions

Directed flow of charged pions in Au+Au collisions at the AGS has been previously measured by the E877 collaboration [35]. The pion directed flow has been found to be very small (of the order of 1/20 in comparison to the proton signal), but significant, and of opposite direction than that of nucleons. It is illustrated in Fig. 7.1, where we show the mean value of the proton and negative pion transverse momentum projected onto the reaction plane  $\langle p_x \rangle$ , with the average estimated in the experimental

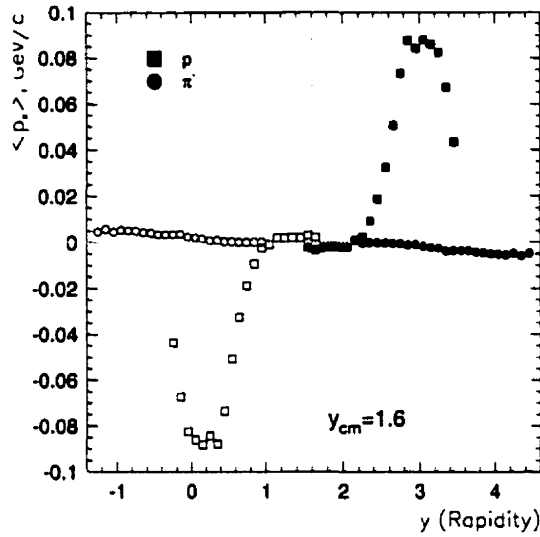


Figure 7.1: Mean transverse momentum in the reaction plane of protons (squares) and negative pions (circles) estimated in the experimental acceptance for centrality region  $200 < E_t < 230$  GeV. The open points are obtained by reflection around mid-rapidity  $y_{cm} = 1.6$ .

acceptance. The values of  $\langle p_x \rangle$  for pions are small and negative in contrast to the large positive  $\langle p_x \rangle$  observed for protons in the forward hemisphere. The maximum  $\langle p_x \rangle$  for pions is observed at very forward rapidities; it reaches about 5 MeV/c.

In the previous chapter, in order to estimate the “true” ellipticity of the proton and deuteron azimuthal distributions, we used a reference frame with an origin displaced along the direction of the reaction plane by  $\langle p_x \rangle$ . This method is applicable in the framework of a thermalized source moving in the transverse plane. For pions, the dependence of directed flow on transverse momentum is very different from that of protons. In Fig. 7.2 we show  $v_1$ , the amplitude of the first harmonic in the Fourier decomposition of the azimuthal particle distribution, as a function of transverse momentum for different rapidity bins and collision centralities for positive and

negative pions. According to the magnetic field polarity selected for the 1995 running

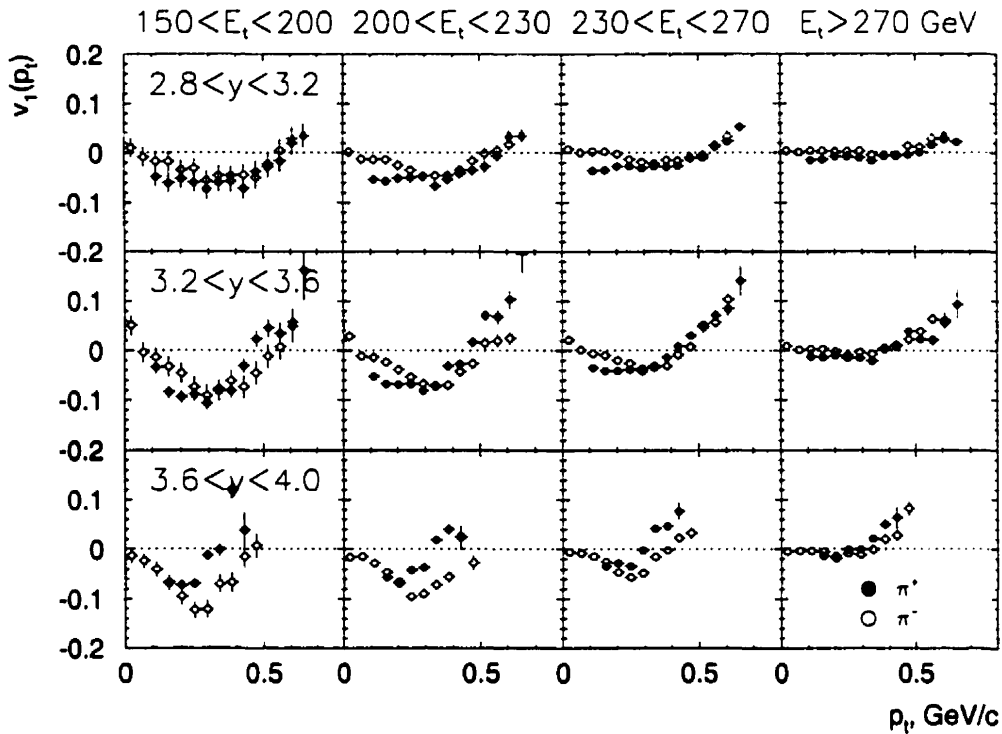


Figure 7.2:  $v_1(p_t)$  of positive (solid circles) and negative (open circles) pions for different rapidity and centrality bins.

period, negative pions have complete  $p_t$ -coverage, whereas experimental acceptance for positive pions is limited at low transverse momenta (see Fig. 4.15). Charged pions of low  $p_t$  are characterized by a weak directed flow in the direction opposite to protons; at higher transverse momenta pions start to flow in the same direction as protons. The directed flow signals of positive and negative pions are different in the low  $p_t$  region, and at higher  $p_t$ 's for very forward rapidities. This behaviour implies that the physics of pion flow is different from that of a moving source alone. The

measured azimuthal asymmetry is a superposition of different effects: absorption in nuclear matter, Coulomb interaction with co-moving protons, resonance production, and sideward motion of the source. The complexity of the pion flow data does not allow to decouple the directed and elliptic flow components by the method used for protons; on the other hand, the smallness of the pion directed flow amplitude is of advantage as its influence on the elliptic flow measurements is much less significant. For pions, we quantify elliptic flow by  $v_2$ , the quadrupole coefficient in the Fourier decomposition of the “raw” (not shifted) azimuthal distribution.

The results on elliptic flow of positive and negative pions are presented in Fig. 7.3. The error bars shown represent statistical errors combined with systematic errors estimated from  $\sin 2\phi$  term in the Fourier expansion. Positive and negative pions exhibit a similar behaviour within experimental uncertainties. On general, weak positive values of  $v_2$  are measured in almost all rapidity bins, with larger signal observed for more peripheral collisions. The observed positive values of  $v_2$  correspond to an elliptically shaped distribution with the major axis lying in the reaction plane. This orientation of the elliptic component of pion flow is perpendicular to what was measured at lower beam energies [104, 105].

Fig. 7.4 and Fig. 7.5 compare transverse momentum dependence of  $v_1$  and  $v_2$  signals for positive and negative pions, respectively. Elliptic flow component exhibits weaker dependence on  $p_t$  than directed flow. However, there is an indication that elliptic flow is increasing with the transverse momentum. The amplitudes of  $v_1$  and  $v_2$  are maximal for more peripheral collisions, reaching -5% and 2%, respectively.

The evaluation of the mean values of  $v_1$  and  $v_2$  in a given rapidity interval for positive pions is difficult due to the hole in the experimental acceptance of positive particles at low transverse momenta. On the other hand, relatively large  $p_t$ -acceptance for negative pions at rapidities forward of 2.6 allows to evaluate the mean values of  $v_1$  and  $v_2$  at a given rapidity interval without any extrapolation to the high- $p_t$  region.

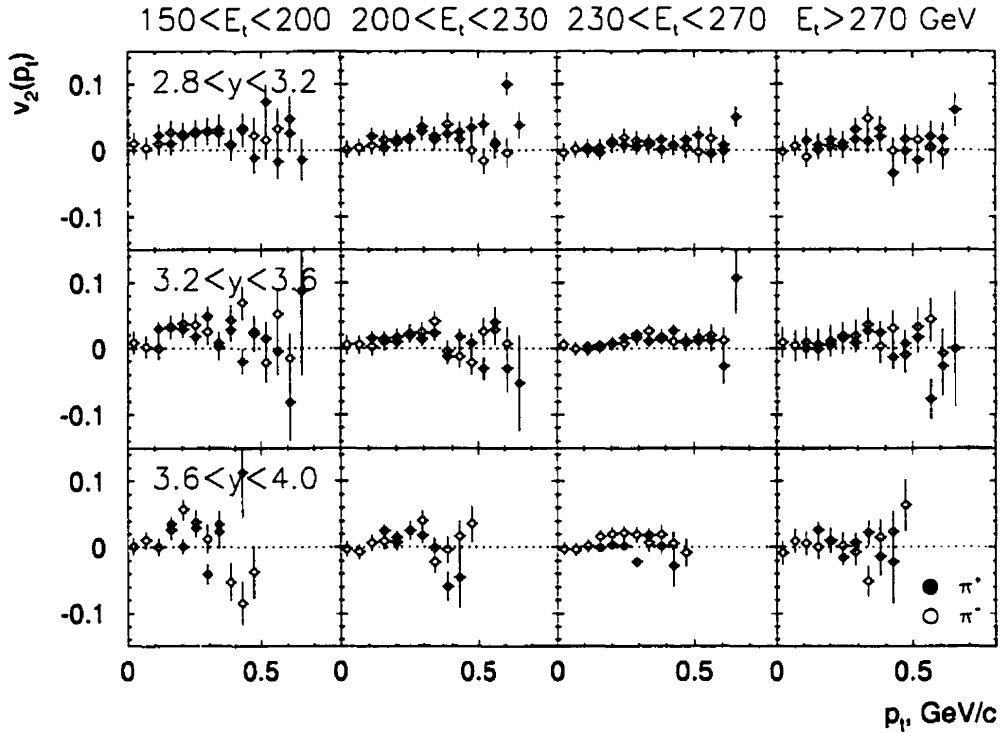


Figure 7.3:  $v_2(p_T)$  of positive (solid circles) and negative (open circles) pions for different rapidity and centrality bins.

The averages can be estimated by convoluting the experimental values of  $v_1(p_T)$  and  $v_2(p_T)$  with the spectra corrected for the detector occupancy and acceptance. The rapidity dependence of directed and elliptic flow amplitudes is presented in Fig. 7.6 for negative pions with reflection about mid-rapidity. In reflection, the signs of the  $v_1$ -values are reversed in the backward hemisphere, but not the  $v_2$ -values. Directed flow exhibits characteristic S-shaped curves for all centralities, with larger signal observed for more peripheral collisions. Elliptic flow is essentially independent of rapidity, and also maximal for semi-central events. The amplitude of the directed flow does not

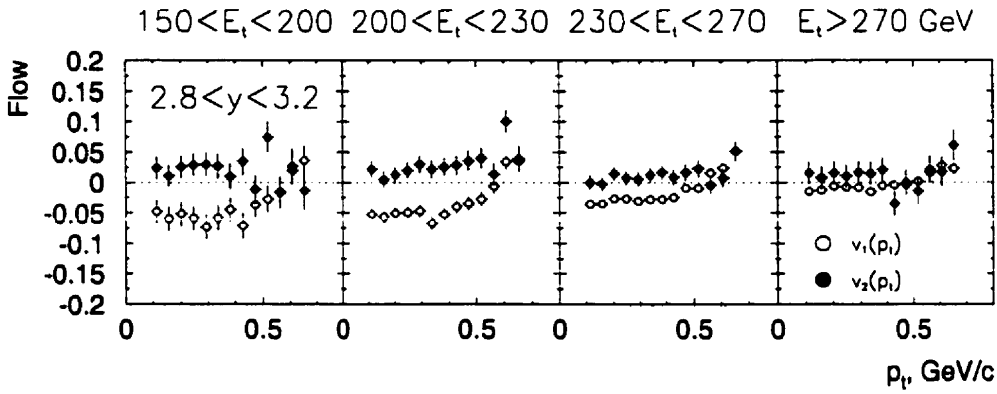


Figure 7.4:  $v_1(p_T)$  (open circles) and  $v_2(p_T)$  (solid circles) of positive pions for rapidity bin  $2.8 < y < 3.2$  and different collision centralities.

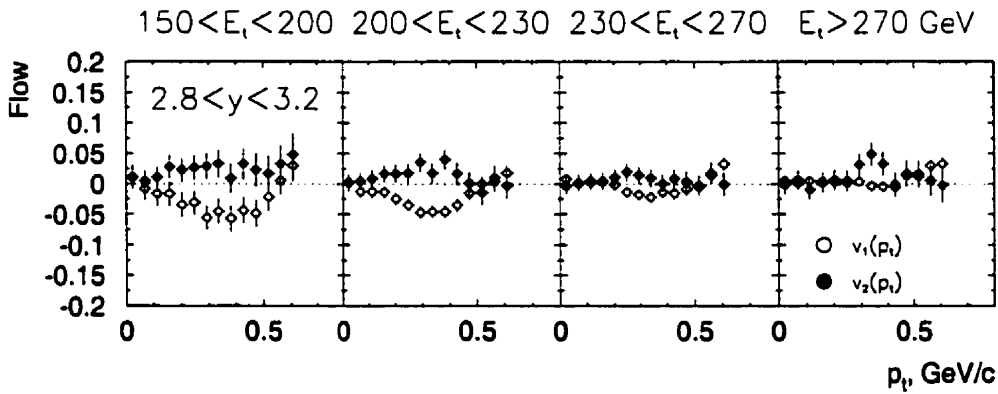


Figure 7.5:  $v_1(p_T)$  (open circles) and  $v_2(p_T)$  (solid circles) of negative pions for rapidity bin  $2.8 < y < 3.2$  and different collision centralities.

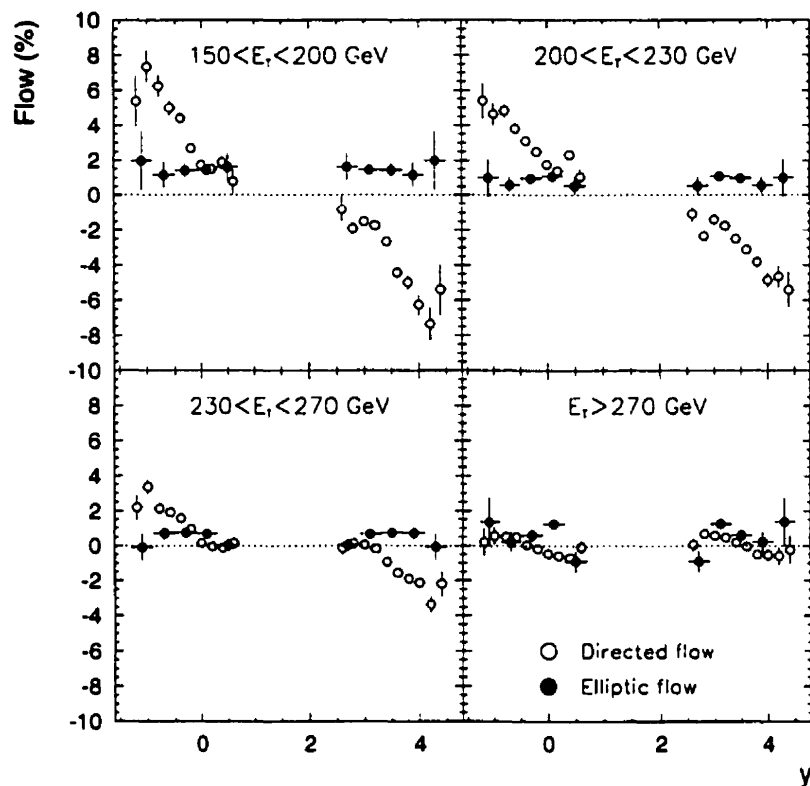


Figure 7.6: Rapidity dependence of directed (open circles) and elliptic (solid circles) flow of negative pions for different collision centralities. The points below mid-rapidity ( $y_{cm} = 1.6$ ) are reflected from the measurements in the forward hemisphere.

seem to strongly affect the measurements of elliptic flow.

## 7.2 Discussion

Collective flow of produced particles, such as pions and kaons, has a different nature than that of nucleons and fragments. Azimuthal anisotropies in the emission patterns

of pions are caused mainly by the pion final-state interaction. Pions are produced either directly from nucleon-nucleon collisions ( $NN \rightarrow NN\pi$ ) or from the decay of resonances, such as  $N^*$ ,  $\Delta$ ,  $\Lambda$ , etc. Due to their small mass, pions created in  $NN$  collisions are not expected to show considerable flow effects if flow is represented by a common velocity superimposed on the thermal motion. On the other hand, since flow behaviour of baryon resonances is similar to that of nucleons, pions produced as decay products of resonances would have a certain flow velocity as a result of momentum conservation. Because of the large pion-nucleon cross section, pion flow signals are also strongly affected by the processes of absorption ( $\pi NN \rightarrow \Delta N \rightarrow NN$ ) and scattering ( $\pi N \rightarrow \Delta \rightarrow \pi N$ ). The rescattering off the cold spectator matter is predicted to result in an anti-flow of pions with respect to nucleons [106, 107].

Experimental measurements of pion azimuthal emission patterns have been performed in a wide energy range, spanning from LBL/SIS energies [81, 104, 62, 105] to AGS [35] and SPS [41]. A characteristic “S-curve” signature of directed flow as a function of rapidity persists at all energies. A directed anti-flow (negative flow) is observed for low  $p_t$  pions, and a positive directed flow is measured for high  $p_t$  pions. The anti-flow for the low  $p_t$  pions is interpreted as a result of strong pion absorption on nucleons, or so-called “shadowing” effect. As the pion-nucleon elastic and total cross sections fall off at higher  $p_t$ , the sideward motion of the source gives rise to positive directed flow, observed also for nucleons.

As for elliptic flow, a strong squeeze-out effect is observed at the LBL/SIS energies. It is illustrated in Fig. 7.7 (from [105]), where the dependence of elliptic flow parameter  $P_2$  on the transverse momentum is shown for positive and negative pions produced in semicentral  $^{209}\text{Bi}+^{209}\text{Bi}$  collisions at 400, 700, and 1000 A·MeV. The elliptic flow parameter  $P_2$  is equal to  $2v_2$  in our notation. The values of  $P_2$  plotted in Fig. 7.7 are not corrected for the reaction plane resolution. As one can see, a much stronger anisotropy is observed at the SIS energy compare to the AGS with

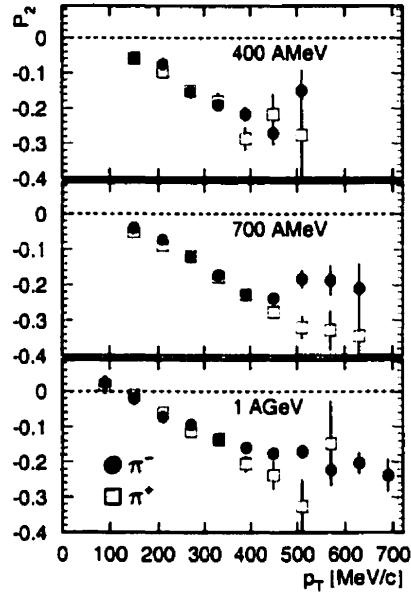


Figure 7.7: Elliptic flow parameter  $P_2$  for mid-rapidity  $\pi^+$  and  $\pi^-$  as a function of the transverse momentum measured for semicentral  $^{209}\text{Bi}+^{209}\text{Bi}$  collisions at 400, 700, and 1000 A·MeV (from [105]).

an out-of-plane preferential emission of pions. According to transport calculations, the preferential emission perpendicular to the reaction plane is caused by rescattering and absorption in the spectator fragments [108]. The pronounced out-of-plane emission of high-energy pions indicate that they freeze-out while spectators are still close to the participant zone.

A different situation is observed at the AGS energy. A weak (about 1-2%) in-plane elliptic flow of pions is developed in semi-central collisions. The measurements of pion elliptic flow at the SPS energy [41] show similar results (2-3% in-plane flow). The shadowing due to spectator matter is of less importance at higher energies as the passage times are much shorter. The interaction with co-moving participant nucleons,

on the other hand, may become a factor. It is interesting that pions show about the same amount of elliptic flow as protons at rapidities close to the mid-rapidity. On the other hand, the  $v_2(y)$ -dependence of pions emitted in the forward rapidity interval shows little variation with rapidity, whereas proton elliptic flow signal exhibits a more pronounced rapidity dependence with a squeeze-out observed at forward (near projectile) rapidities. The difference in the observed rapidity behaviour of the proton and pion elliptic flow may be due to the difference in relative location of the pion and proton sources in space and/or time. The relative space time asymmetries in pion and proton emission in non-central high energy heavy ion collisions were studied using non-identical particle correlation functions [109]. It was shown that in the framework of the Relativistic Quantum Molecular Dynamics model, the proton and pion effective sources are shifted with respect to each other in the reaction plane. A recent analysis of the experimental data at the AGS energy [103] has shown that sources of protons and pions are separated by 5 fm in the reaction plane, and proton source is located 10 fm more forward than the sources of pions in the longitudinal direction. Such a separation could result in a less effective screening of the pions by nucleons and an absence of the squeeze-out effect for pions at the ultra-relativistic energies.

The results on directed flow of positive and negative pions are compared to the predictions of the Relativistic Quantum Molecular Dynamics elsewhere [70]. The model qualitatively reproduces the observed  $v_1(p_t)$ -dependence, but over-predicts the amplitude of directed flow. In Fig. 7.8 we compare the measurements of elliptic flow of negative pions with the RQMD v2.3 run in cascade mode. The pure cascade calculations show a remarkable agreement with the experimental data with no apparent difference seen between the data and calculations within experimental and statistical uncertainties. The measurements of elliptic flow of negative pions are also compared with the RQMD event generator run in mean field mode (Fig. 7.9). The introduction

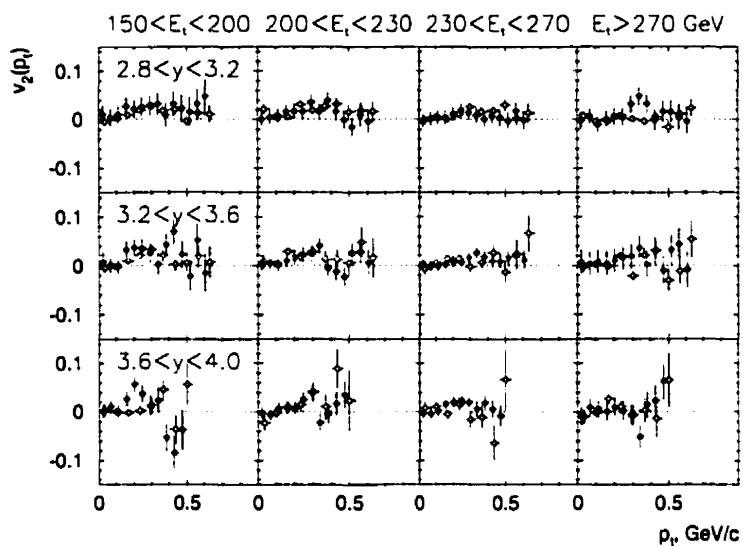


Figure 7.8: Comparison of  $\pi^- v_2(p_t)$  data (solid circles) with calculations of RQMD v2.3 run in cascade mode (open circles).

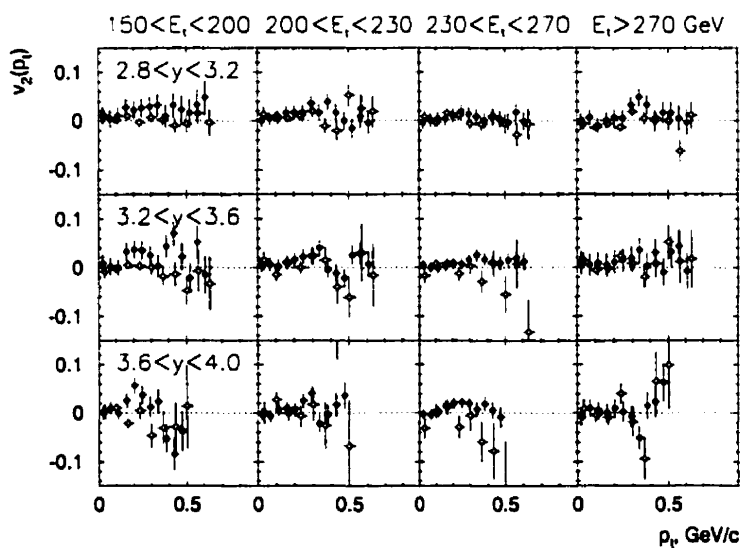


Figure 7.9: Comparison of  $\pi^- v_2(p_t)$  data (solid circles) with calculations of RQMD v2.3 run in mean field mode (open circles).

of the mean field potential into the calculations lessens the amount of elliptic flow, showing a clear disagreement with the data in most peripheral centrality bin. The results for positive pions are similar to those obtained for negative pions.

In Fig. 7.10 we compare the rapidity dependence of the measured mean  $v_2$  of negative pions to the calculations of RQMD v2.3 run in cascade and mean field modes. The calculations predict an in-plane elliptic flow of pions at mid-rapidity,

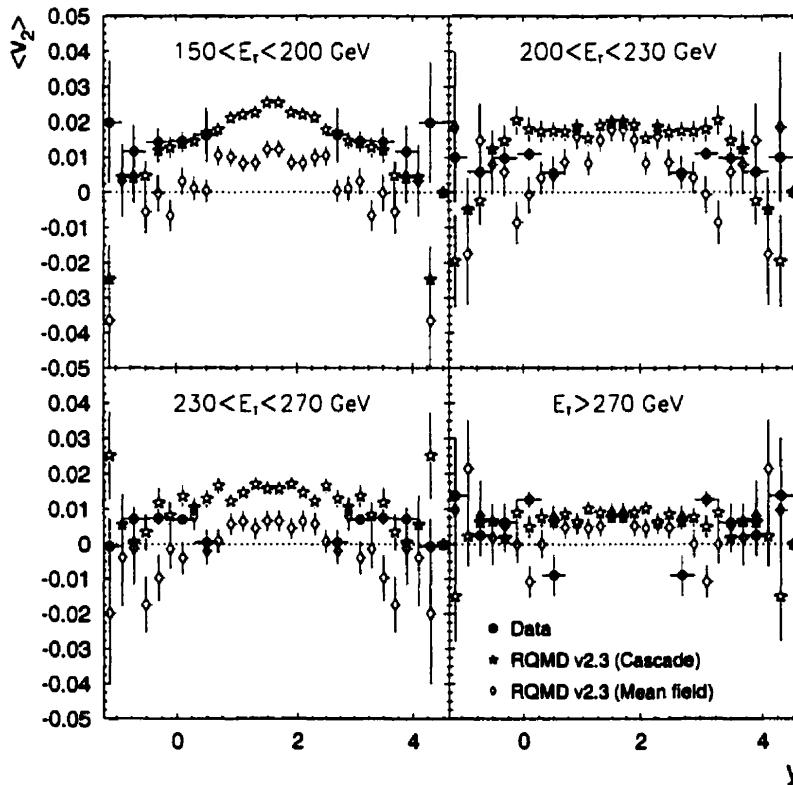


Figure 7.10: Comparison of  $\pi^- v_2(y)$  data (solid circles) with calculations of RQMD v2.3 run in cascade mode (open stars) and same model run in mean field mode (open diamonds). Both the data and the calculations are reflected around  $y_{cm} = 1.6$ .

with about 2% deformation in case of cascade calculations and in the order of 1% deformation for mean field calculations. Similar to  $v_2(p_t)$ -dependence, the cascade mode of the RQMD provides a better agreement with the data compared to the mean field mode. The opposite has been seen in the comparison of the proton elliptic flow data and calculations.

### 7.3 Kaon identification

Whereas pions are produced copiously in high energy heavy ion collisions, the production cross sections of kaons, especially anti-kaons, are much lower. Because of their low yield compare to other particles, kaons are more difficult to identify. As flow signals are very sensitive to contamination between particle species, a thorough separation of particles and rejection of background are needed to obtain a clean sample of kaons. The upgrade of the E877 experimental setup with two high-resolution upstream tracking detectors (VTXA and VTXB) allows us to confirm track  $x$ -coordinates before the analyzing magnet and reject false or misidentified tracks. The effect of using vertex chamber information is illustrated in Fig. 7.11. The contour plot of momentum versus mass squared is presented with and without requiring a confirmation from vertex detectors. On this plot, the pions and kaons are separated according to their measured mass and momentum. The mass resolution depends on momentum, and is better at low momenta. Requiring a confirmation from vertex detectors drastically improves the rejection of the background tracks and allows to better separate the pions from kaons. The effects of different vertex cuts have been studied in detail. As position resolution of vertex detectors is momentum-dependent, a parameterization of the detector response as a function of momentum has been performed. More details on this procedure can be found in [98, 70]. The parameterized resolutions of the vertex detectors  $\sigma_{vtxa}, \sigma_{vtxb}$  are used to require a

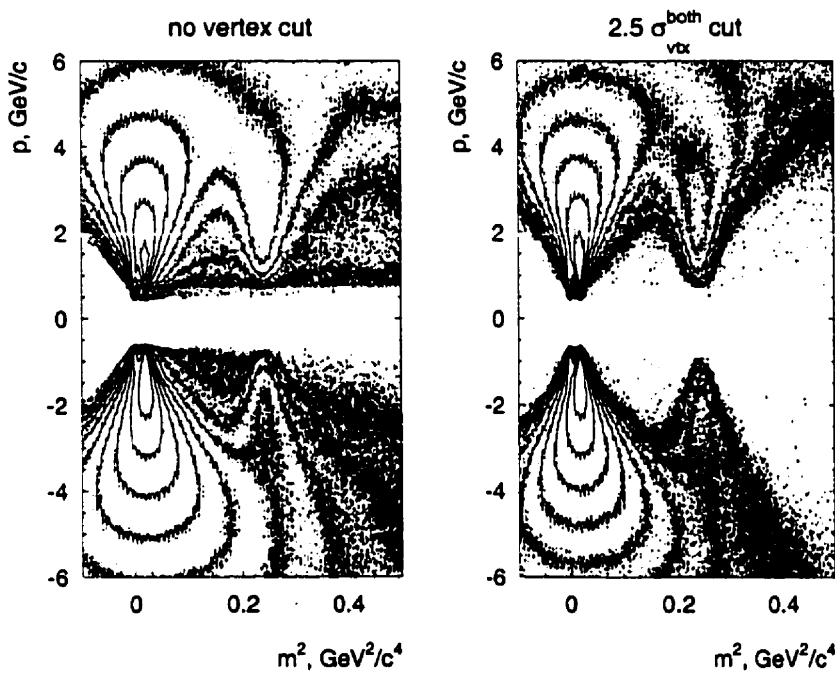


Figure 7.11: Momentum versus mass squared contour plot without vertex chamber confirmation (left panel) and with  $2.5\sigma_{vtx}^{both}$  cut applied to confirm the tracks (right panel).

match of the  $x$ -coordinates of the track before and after the magnet within a certain window. In the present analysis, we require an  $x$ -coordinate of the track to be within  $2.5\sigma$  of the  $x$ -position measured in both vertex detectors. The results of this cut are presented in Fig. 7.12, where we show the mass squared distributions of positive and negative kaons for different momentum windows. At low particle momenta, the major source of background is “false” tracks. At high particle momenta, the kaon sample is contaminated by the tail of the pion distribution. In order to limit the pion contamination, we apply a maximum momentum cut for kaon identification of  $p_{max} = 3.5$  GeV/c. In addition, we also require that the measured mass squared  $m^2$

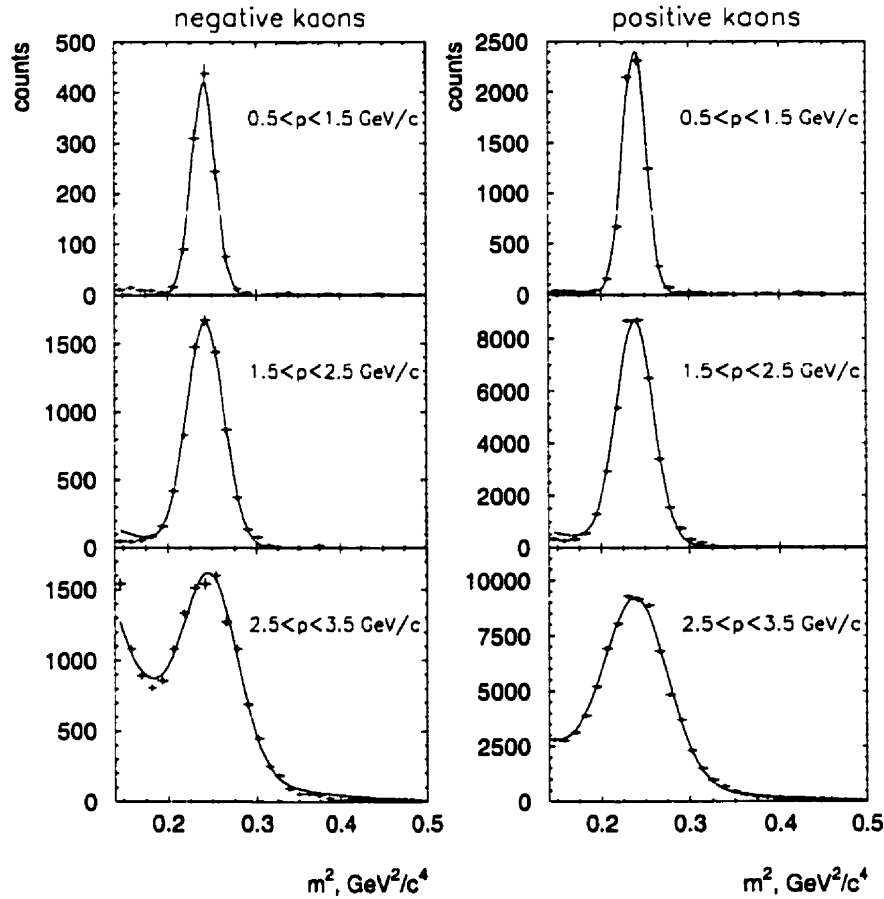


Figure 7.12: Mass squared distributions for negative and positive kaons in different momentum windows.

was  $3.5 \sigma$  away from the mean of mass squared of pions. The total background is estimated to be in the order of 5% in the  $0.5 < p < 2.5$  region and less than 15 % in the  $2.5 < p < 3.5$  region.

The acceptance of positive and negative kaons in  $(p_t, y)$ -space is shown in Fig. 7.13. The polarity setting of the magnetic field in 1995 results in a hole in the experimental acceptance for positive kaons at low  $p_t$ . An analysis of  $\sim 146,000 K^+$  and  $\sim 28,000 K^-$

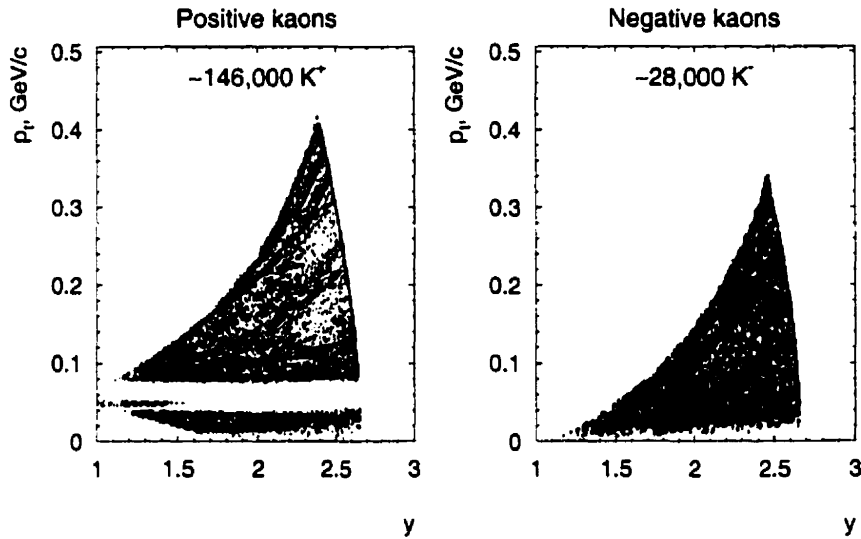


Figure 7.13: Acceptance plots for positive and negative kaons.

produced in Au+Au collisions at 11.5 GeV/c is presented below.

## 7.4 Experimental Results on Flow of Kaons

Similar to pions, directed flow of kaons is very small and does not effect the measurements of the elliptic component. The dependence of the first Fourier coefficient,  $v_1$ , on transverse momentum is presented in Fig. 7.14. The directed flow of both positive and negative kaons is weak. The positive kaons are characterized by negative values of  $v_1$  for all rapidity and centrality bins. The large statistical uncertainties in the  $v_1(p_t)$ -dependence of  $K^-$  does not allow to draw a definite conclusion about a sign of their directed flow. In the window with the best combination of statistics and signal, rapidity bin  $2.3 < y < 2.7$  and centrality bin  $230 < E_t < 270$  GeV,  $v_1$  of  $K^-$  is negative and smaller than  $v_1$  of  $K^+$  in the mid- $p_t$  range.

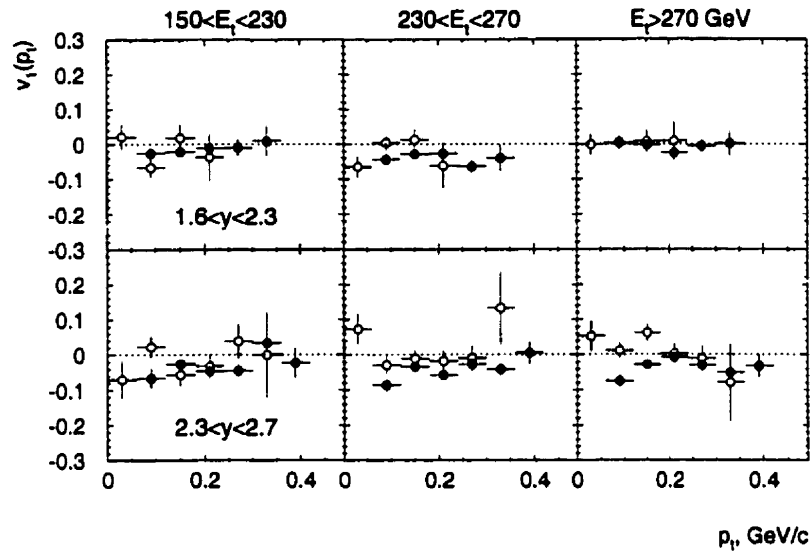


Figure 7.14:  $v_1(p_t)$  of positive (solid circles) and negative (open circles) kaons for different rapidity and centrality bins.

The dependence of the amplitude of elliptic flow with transverse momentum is presented in Fig. 7.15 for both types of kaons. The measured  $v_2$ -values for both  $K^+$  and  $K^-$  are consistent with zero within experimental uncertainties, except perhaps, the window with rapidity  $1.6 < y < 2.3$  and centrality  $150 < E_t < 230$  GeV, where negative values of  $v_2$  are observed for  $K^-$  and positive values of  $v_2$  are measured for  $K^+$ .

We also estimated the directed and elliptic flow signal of kaons averaged over the  $p_t$ -acceptance of the spectrometer. The left panel of Fig. 7.16 shows the azimuthal angular distribution with respect to the reaction plane for  $K^+$  measured in the transverse momentum range  $0.06 < p_t < 0.4$  GeV/c for rapidity bin  $2.3 < y < 2.7$  and centrality bin  $230 < E_t < 270$  GeV. The distribution is normalized to unity and not corrected for the reaction plane resolution. The azimuthal distribution of particles

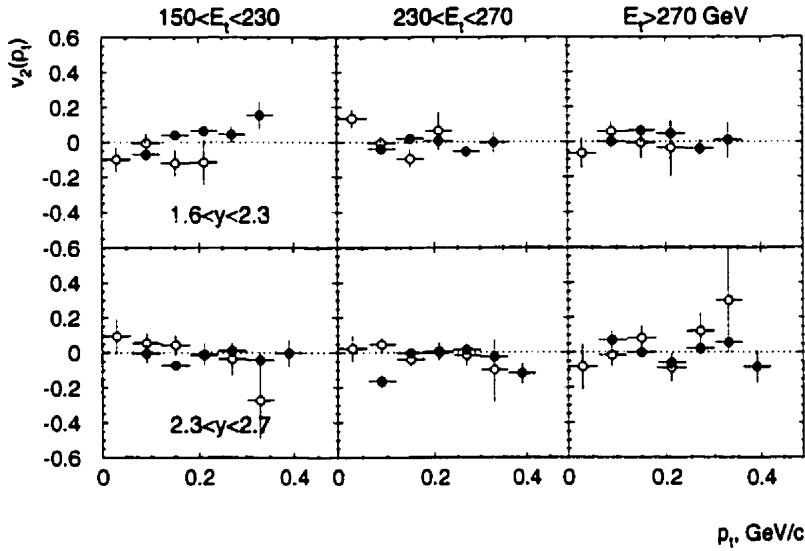


Figure 7.15:  $v_2(p_t)$  of positive (solid circles) and negative (open circles) kaons for different rapidity and centrality bins.

can be parameterized by

$$\frac{dN}{d\phi} = 1 + 2v_1 \cos \phi + 2v_2 \cos 2\phi, \quad (7.1)$$

where  $\phi$  is the azimuthal angle of particle with respect to the reaction plane. The fit of the above expression to the distribution shown in the left panel of Fig. 7.16 gives average values  $v_1 = -0.032 \pm 0.004$  and  $v_2 = -0.006 \pm 0.004$ . As cosine-like functions have to be symmetric about  $0^\circ$ , we can double the statistics by averaging the measurements in the  $[-\pi; 0]$  and  $[0; \pi]$  regions. The solid points in the right panel of Fig. 7.16 show the average of the measurements in  $[-\pi; 0]$  and  $[0; \pi]$  regions of the azimuthal angle. The open points in the same figure are obtained by reflection of the solid points about zero. The fitting of the obtained distribution with Eq. 7.1 results in similar values of  $v_1$  and  $v_2$ , but smaller statistical uncertainties.

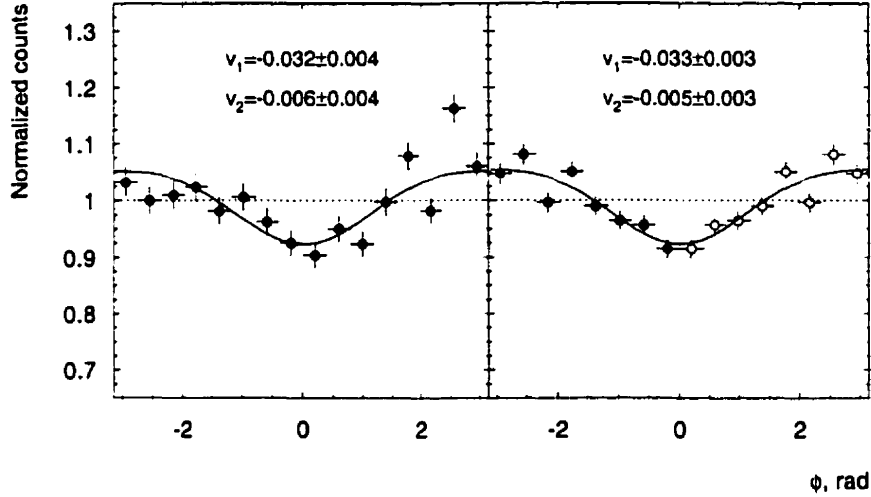


Figure 7.16: Azimuthal distributions of positive kaons in the transverse momentum range  $0.06 < p_t < 0.4$  GeV/c for rapidity bin  $2.3 < y < 2.7$  and centrality bin  $230 < E_t < 270$  GeV. The left panel shows the raw distribution, whereas the panel on the right shows the distribution of  $\phi$ 's folded in into a  $[-\pi; 0]$  range (solid points) and reflected around zero (open points). The solid lines are the fits using Eq. 7.1.

We performed this procedure for each rapidity and centrality bin. The results are shown in Fig. 7.17 and Fig. 7.18 for  $K^+$  and  $K^-$  measured in the transverse momentum range  $0.06 < p_t < 0.4$  GeV/c. For  $K^+$ , negative values of  $v_1$ -coefficient are observed in all rapidity and centrality bins. For  $v_2$ , the most significant signal is observed in the most peripheral centrality bin, with positive  $v_2 = 0.016 \pm 0.004$  measured for rapidities close to mid-rapidity ( $1.6 < y < 2.3$ ), and negative  $v_2 = -0.012 \pm 0.004$  measured in the  $2.3 < y < 2.7$  region. These values are not corrected for the reaction plane resolution. In this particular centrality bin, the measured values of  $v_2$  need to be multiplied by a factor of  $\sim 2.5$  to obtain the true values of  $v_2$ .

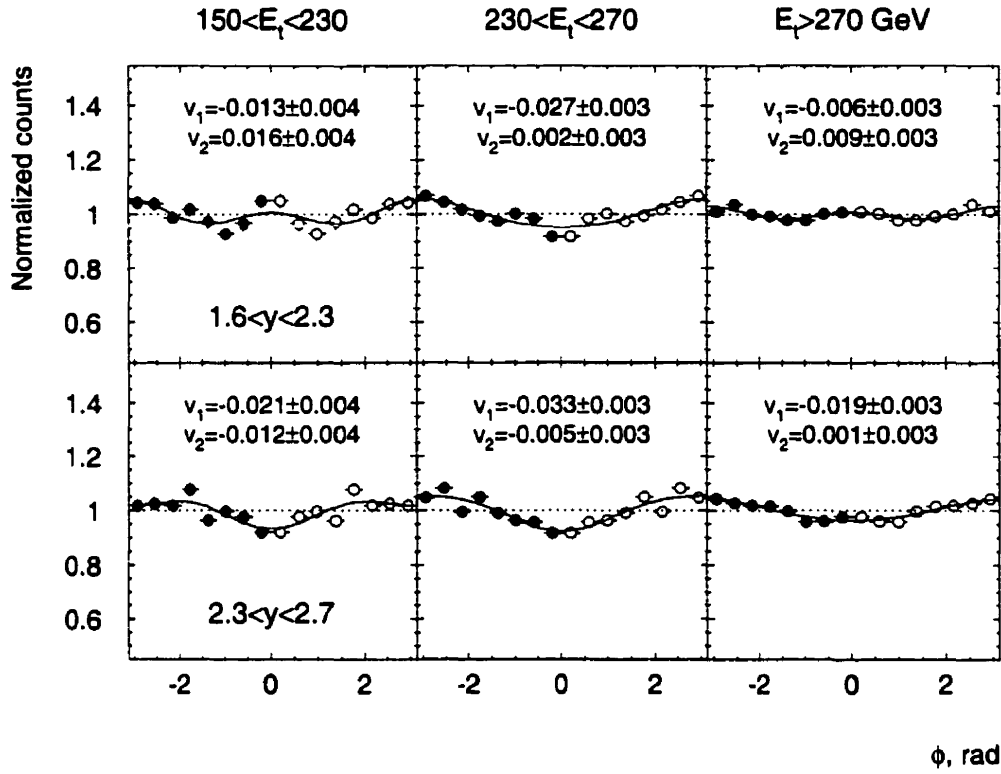


Figure 7.17: Azimuthal distributions of positive kaons in the transverse momentum range  $0.06 < p_t < 0.4$  GeV/c for different rapidity and centrality bins. The open points are obtained by reflection of the solid points. The solid lines are the fits using Eq. 7.1.

For  $K^-$ , significant amplitudes of  $v_1$  and  $v_2$  are only observed for  $150 < E_t < 230$  centrality bin and rapidities close to mid-rapidity  $1.6 < y < 2.3$ . Taking into account the reaction plane resolution, the corrected values for this window are  $v_1 = -0.037 \pm 0.015$  and  $v_2 = -0.051 \pm 0.029$ .

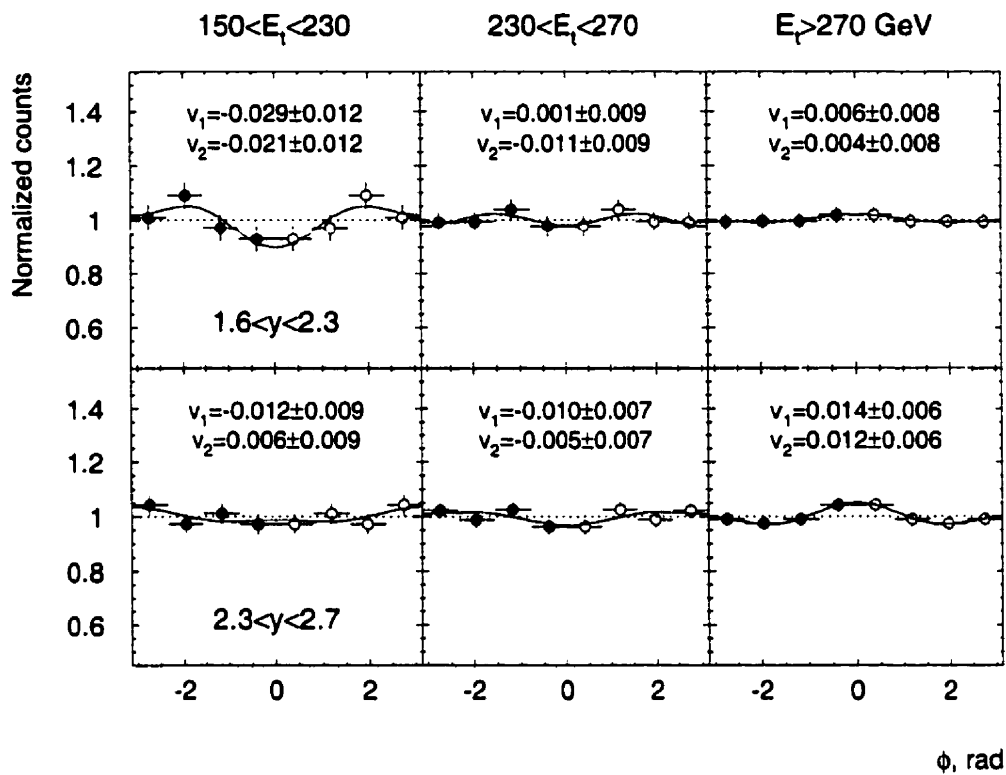


Figure 7.18: Azimuthal distributions of negative kaons in the transverse momentum range  $0.06 < p_t < 0.4$  GeV/c for different rapidity and centrality bins. The open points are obtained by reflection of the solid points. The solid lines are the fits using Eq. 7.1.

## 7.5 Discussion

Kaons carry distinctly different information than protons or pions. Positive kaons have a lower cross section of interaction with nuclear matter than pions, and their flow signal should be less influenced by absorption and scattering effects. Theoretical studies show that flow measurements for  $K^+$  are sensitive probes of kaon properties

in dense hadronic matter [63]. Kaons are mainly produced from baryon-baryon collisions. The baryon transverse flow results in a large asymmetry of baryon density distribution in the reaction plane. Kaons moving in this medium thus develop an opposite asymmetry due to their interaction with baryons through the mean field potential [110]. The azimuthal distributions of negative kaons are sensitive to the both absorption and mean-field potential effects [111].

Experimental measurements of kaon flow signal are especially interesting but difficult to obtain due to the low production cross sections, particularly for  $K^-$ . The directed flow of  $K_s^0$  and  $K^+$  has been measured for Ni+Ni collisions at 1.93 A·GeV by the FOPI collaboration [66]. No evidence for directed flow of kaons has been seen at this energy, which was interpreted as a signature for a weakly repulsive in-medium kaon-nucleon potential [63]. An anisotropic azimuthal emission of  $K^+$  mesons has been recently found by the KaoS collaboration in Au+Au collisions at 1 A·GeV [82]. A large elliptic deformation of the flow tensor has been seen for  $K^+$  mesons with major axis lying in the direction perpendicular to the reaction plane.

At the AGS energy, the experimental measurements show that positive kaons experience weak directed anti-flow. The predictions of Relativistic Quantum Molecular Dynamics model run in cascade and mean field modes for  $K^+$  and  $K^-$  directed flow dependence on rapidity for centralities corresponding to  $150 < E_t < 200$  GeV bin are shown in Fig. 7.19. The model predicts positive directed flow for  $K^+$  if mean field potentials are included into the calculations. The pure cascade version of the RQMD, on the other hand, predicts weak negative values of  $v_1$  for rapidities between mid-rapidity and beam rapidity, consistent with the experimental data. Both modes of the RQMD model predict strong anti-flow of  $K^-$ . On the contrary, the experimental data show no or very weak anti-flow.

Predictions of the RQMD model for elliptic flow of  $K^+$  and  $K^-$  are shown in Fig. 7.20. Both cascade and mean field modes of the RQMD predict for  $K^+$  and  $K^-$

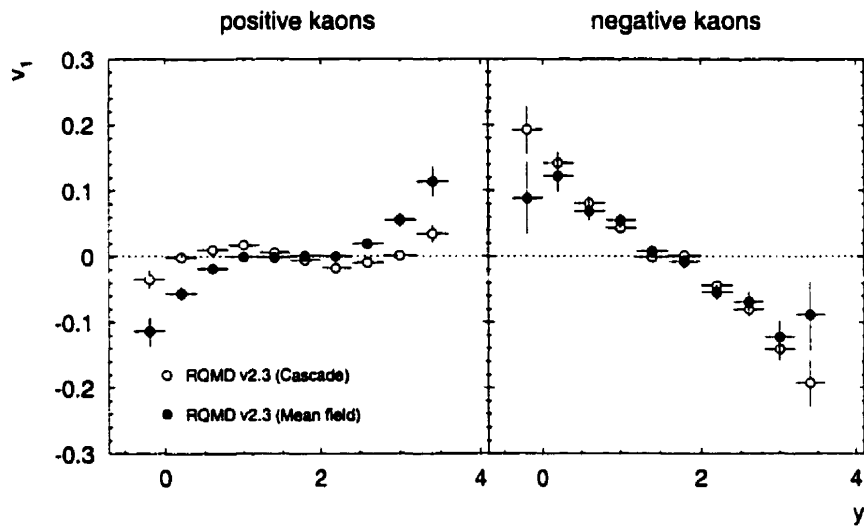


Figure 7.19:  $v_1(y)$  for  $K^+$  (left panel) and  $K^-$  (right panel) as calculated by the RQMD v2.3 run in cascade mode (open circles) and mean field mode (solid circles).

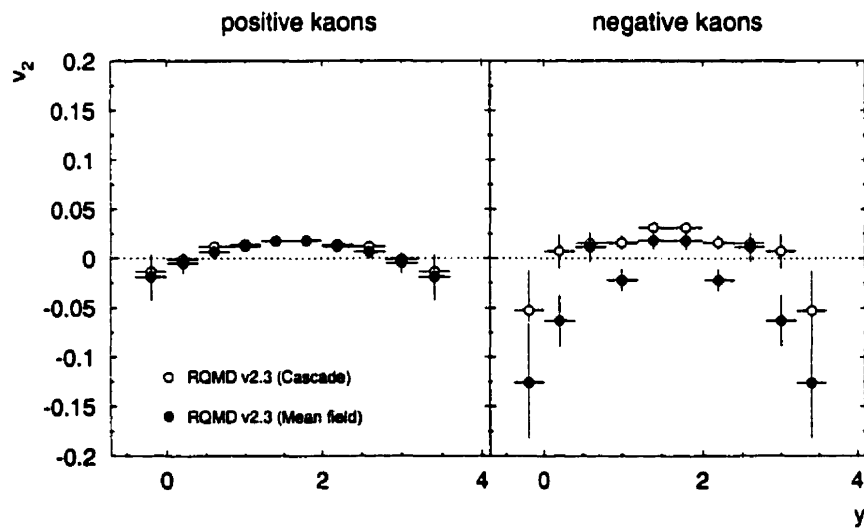


Figure 7.20:  $v_2(y)$  for  $K^+$  (left panel) and  $K^-$  (right panel) as calculated by the RQMD v2.3 run in cascade mode (open circles) and mean field mode (solid circles).

positive (in-plane) elliptic flow at mid-rapidity and negative (out-of-plane) elliptic flow at beam rapidity. The experimental data exhibit a similar trend for  $K^+$ , and opposite to that for  $K^-$ .

# Chapter 8

## Conclusions

In this thesis, the anisotropies in the azimuthal distributions of identified particles with respect to the reaction plane have been studied as a function of particle rapidity, particle transverse momentum and collision centrality in Au+Au collisions at 11.5 A·GeV/c. The orientation of the reaction plane is determined using an azimuthal anisotropy in distribution of transverse energy measured by the E877 calorimeters. A robust procedure required to flatten the reaction plane distribution has been developed. A Fourier expansion method is used to quantify the anisotropy in particle production relative to the reaction plane. A new development of the method has been proposed for decoupling the elliptic component of the asymmetry from the directed component for the analysis of nucleon and fragment transverse flow.

Elliptic flow has been predicted to be very sensitive to the pressure at maximum compression. A collective out-of-plane emission (negative elliptic flow) of protons and light fragments has been observed at the Bevalac energies. A transition from out-of-plane to in-plane elliptic flow has been predicted to take place in the energy range  $E=2-8$  GeV, as the passage time for removal of the shadowing due to the projectile and target spectators decreases with higher beam energy. Using a new technique for

analyzing the elliptic flow signal, we have demonstrated that the observed rapidity dependence of the proton elliptic flow at the AGS exhibits similar behaviour, with in-plane elliptic flow measured for mid-rapidity region, and out-of-plane elliptic flow measured at the projectile/target rapidities. The rapidity dependence of elliptic deformation of the flow tensor may provide a good probe for the study of the transient pressure in the collision.

The proton elliptic flow data have been compared to the predictions of the RQMD v2.3 model. It has been shown that the model explains general features exhibited by the experimental data, but a better quantitative description of the data is needed. Similar to directed flow, the mean field mode of the RQMD provides a better overall description of the elliptic flow data compared to the pure cascade mode.

We have also measured the elliptic flow signal of deuterons. It has been shown that the amplitude of deuteron elliptic flow is larger in the beam rapidity region compared to that of protons. This trend is consistent with predictions of the coalescence model of deuteron production including volume effects.

The physics responsible for the pion azimuthal asymmetries is different from the compressional effects governing the directed and elliptic flow effects of nucleons. The pion emission is correlated to the reaction dynamics through the pion-nucleon interaction which is sensitive to the density and momentum dependence of the nucleon optical potential. A strong squeeze-out effect (negative elliptic flow) is observed for pions produced at the LBL/SIS energies. At the AGS energy, our analysis shows that a weak in-plane elliptic of pions develops in semi-central collisions. The observed effect is attributed to the less effective screening of pions by the cold spectator nucleons at higher incident energies. The separation of effective pion and proton sources in space and/or time may also be a factor. The comparison of the experimental data to the predictions of the RQMD model shows that, contrary to what has been seen for protons, the cascade calculation provide a better description of the data compared

to the predictions of the model run in mean field mode.

The measurement of the azimuthal anisotropies in kaon production is especially interesting as it is predicted to be sensitive to the properties of the kaon potential in the dense nuclear medium. No signal of directed flow of positive kaons has been seen in low energy nuclear collisions. We have observed a weak negative directed flow of  $K^+$  at the AGS energy. The RQMD model predicts a similar effect for the pure cascade calculations, whereas the mean field mode of the model predicts a weak positive directed flow. Both cascade and mean field modes of the RQMD predict strong anti-flow of  $K^-$ , while the experimental data show no or little effect.

A strong out-of-plane emission of  $K^+$  in Au+Au collisions at 1 A·GeV has been recently reported by the KaoS collaboration. Cascade and mean field modes of the RQMD predict positive (in-plane) elliptic flow at mid-rapidity and negative (out-of-plane) elliptic flow at beam rapidity for both  $K^+$  and  $K^-$ . The obtained experimental results indicate a similar trend for  $K^+$ , but opposite to that for  $K^-$ .

In summary, the collective flow of particles and fragments is a very useful tool for the exploration of in-medium properties of dense and highly excited baryonic matter produced with heavy ions at the AGS. The presented comprehensive measurements of elliptic flow for particles of different kinds provide new constraints on theory. Further theoretical developments are needed to account for the full set of flow observations in nuclear collisions.

# Bibliography

- [1] E. Shuryak, *The QCD vacuum, hadrons and the superdense matter* (World Scientific, Singapore, 1988).
- [2] J. W. Harris and B. Müller, *The search for the quark - gluon plasma*, Annual Review of Nuclear and Particle Science **46**, 71 (1996).
- [3] J. Stachel, *Tests of thermalization in relativistic nucleus-nucleus collisions*, Nuclear Physics A **610**, 509 (1996), presented at 12th International Conference on Ultrarelativistic Nucleus-Nucleus Collisions (Quark Matter 96), Heidelberg, Germany, 20-24 May 1996.
- [4] J. W. Harris, *Relativistic heavy ion physics and the relativistic heavy ion collider*, in proceedings of *Lake Louise Winter Institute: Quantum Chromodynamics, Lake Louise, Alberta, Canada, February 15-21, 1998*, (World Scientific, Singapore, 1998).
- [5] L. Landau, *On the multiparticle production in high-energy collisions*, Izvestia Akademii Nauk SSSR, Ser. Fiz. **17**, 51 (1953).
- [6] G. Chapline, M.H.Johnson, E.Teller, and M. Weiss, *Highly excited nuclear matter*, Physical Review D **8**, 4302 (1973).

- [7] W. Scheid, H. Müller, and W. Greiner, *Nuclear shock waves in heavy-ion collisions*, Physical Review Letters **32**, 741 (1974).
- [8] M. Sobel, H. Bethe, P. Siemens, and J. Bondorf, *Shock waves in colliding nuclei*, Nuclear Physics A **251**, 502 (1975).
- [9] H. Gustafsson *et al.*, *Collective flow observed in relativistic nuclear collisions*, Physical Review Letters **52**, 1590 (1984).
- [10] R. Renfordt *et al.*, *Stopping power and collective flow of nuclear matter in the reaction Ar + Pb at 0.8-GeV/u*, Physical Review Letters **53**, 763 (1984).
- [11] W. Reisdorf and H. Ritter, *Collective flow in heavy-ion collisions*, Annual Review of Nuclear and Particle Science **47**, 663 (1997).
- [12] A. Poskanzer and S. Voloshin, *Methods for analyzing anisotropic flow in relativistic nuclear collisions*, Physical Review C **58**, 1671 (1998).
- [13] J.-Y. Ollitrault, *Flow systematics from SIS to SPS energies*, Nuclear Physics A **638**, 195 (1998), presented at 13th International Conference on Ultrarelativistic Nucleus-Nucleus Collisions (Quark Matter 97), Tsukuba, Japan, 1-5 Dec 1997.
- [14] M. Lisa *et al.*, *Radial flow in Au+Au collisions at  $E=(0.25-1.15)$  A GeV*, Physical Review Letters **75**, 2662 (1995).
- [15] S. Jeong *et al.*, *Collective motion in selected central collisions of Au on Au at 150A MeV*, Physical Review Letters **72**, 3468 (1994).
- [16] T. Abbott *et al.*, *Charged hadron distributions in central and peripheral Si + A collisions at 14.6-A/GeV/c*, Physical Review C **50**, 1024 (1994).
- [17] N. Xu *et al.*, *Hadron distributions - recent results from the CERN experiment NA44*, Nuclear Physics A **610**, 175 (1996), presented at 12th International

- Conference on Ultrarelativistic Nucleus-Nucleus Collisions (Quark Matter 96), Heidelberg, Germany, 20-24 May 1996.
- [18] G. Westfall *et al.*, *Nuclear fireball model for proton inclusive spectra from relativistic heavy-ion collisions*, *Physical Review Letters* **37**, 1202 (1976).
- [19] P. J. Siemens and J. O. Rasmussen, *Evidence for a blast wave from compressed nuclear matter*, *Physical Review Letters* **42**, 880 (1979).
- [20] K. S. Lee and U. Heinz, *Collective flow model for the pion transverse momentum spectra from relativistic nuclear collisions at CERN*, *Zeitschrift Für Physik C* **43**, 425 (1989).
- [21] K. S. Lee, U. Heinz, and E. Schnedermann, *Search for collective transverse flow using particle transverse momentum spectra in relativistic heavy ion collisions*, *Zeitschrift Für Physik C* **48**, 525 (1990).
- [22] J. Bjorken, *Highly relativistic nucleus-nucleus collisions: The central rapidity region*, *Physical Review D* **27**, 140 (1983).
- [23] E. Schnedermann, J. Sollfrank, and U. Heinz, *Thermal phenomenology of hadrons from 200-A/GeV S+S collisions*, *Physical Review C* **48**, 2462 (1993).
- [24] P. Braun-Munzinger, J. Stachel, J. Wessels, and N. Xu, *Thermal equilibration and expansion in nucleus-nucleus collisions at the AGS*, *Physics Letters B* **344**, 43 (1995).
- [25] J. Cugnon, J. Knoll, C. Riedel, and Y. Yari, *Event by event emission pattern analysis of the intranuclear cascade*, *Physics Letters B* **109**, 167 (1982).
- [26] M. Gyulassy, K. Frankel, and H. Stocker, *Do nuclei flow at high-energies?*, *Physics Letters B* **110**, 185 (1982).

- [27] P. Danielewicz and G. Odyniec, *Transverse momentum analysis of collective motion in relativistic nuclear collisions*, Physics Letters B **157**, 146 (1985).
- [28] S. Voloshin and Y. Zhang, *Flow study in relativistic nuclear collisions by Fourier expansion of azimuthal particle distributions*, Zeitschrift Für Physik C **70**, 665 (1996).
- [29] H. H. Gutbrod, A. M. Poskanzer, and H. G. Ritter, *Plastic Ball experiments*, Reports on Progress in Physics **52**, 1267 (1989).
- [30] M. Partlan *et al.*, *Fragment flow in Au + Au collisions*, Physical Review Letters **75**, 2100 (1995).
- [31] P. Crochet *et al.*, *Onset of nuclear matter expansion in Au + Au collisions*, Nuclear Physics A **624**, 755 (1997).
- [32] J. Barrette *et al.*, *Observation of anisotropic event shapes and transverse flow in ultrarelativistic Au+Au collisions*, Physical Review Letters **73**, 2532 (1994).
- [33] J. Barrette *et al.*, *Directed flow and particle production in Au + Au collisions from experiment E877 at the AGS*, Nuclear Physics A **590**, 259 (1995), presented at 11th International Conference on Ultrarelativistic Nucleus-Nucleus Collisions (Quark Matter 95), Monterey, CA, 9-13 Jan 1995.
- [34] J. Barrette *et al.*, *Energy and charged particle flow in 10.8-A/GeV/c Au + Au collisions*, Physical Review C **55**, 1420 (1997).
- [35] J. Barrette *et al.*, *Proton and pion production relative to the reaction plane in Au + Au collisions at AGS energies*, Physical Review C **56**, 3254 (1997).
- [36] J. Barrette *et al.*, *Directed flow of light nuclei in Au + Au collisions at AGS energies*, e-print: nucl-ex/9805006, submitted to Physical Review C.

- [37] S. Voloshin *et al.*, *Anisotropic flow of identified particles in Au + Au collisions at AGS energy*, Nuclear Physics A **630**, 455 (1998), presented at 13th International Conference on Ultrarelativistic Nucleus-Nucleus Collisions (Quark Matter 97), Tsukuba, Japan, 1-5 Dec 1997.
- [38] H. Liu *et al.*, *Collective flow and particle spectra in relativistic heavy ion collisions*, Nuclear Physics A **630**, 549 (1998), presented at 6th International Conference on Nucleus-Nucleus Collisions (NN 97), Gatlinburg, TN, 2-6 Jun 1997.
- [39] H. Liu *et al.*, *Collective flow in Au+Au collisions between 2-8 A GeV at AGS*, Nuclear Physics A **638**, 451 (1998), presented at 13th International Conference on Ultrarelativistic Nucleus-Nucleus Collisions (Quark Matter 97), Tsukuba, Japan, 1-5 Dec 1997.
- [40] C. Ogilvie *et al.*, *Au + Au reactions at the AGS: Experiments E866 and E917*, Nuclear Physics A **630**, 57 (1998), presented at 6th International Conference on Nucleus-Nucleus Collisions (NN 97), Gatlinburg, TN, 2-6 Jun 1997.
- [41] H. Appelshauser *et al.*, *Directed and elliptic flow in 158-GeV / nucleon Pb + Pb collisions*, Physical Review Letters **80**, 4136 (1998).
- [42] T. C. Awes and the WA98 Collaboration, *Collective flow as a probe of heavy ion reaction dynamics*, Nuclear Physics A **630**, 499 (1998), presented at 6th International Conference on Nucleus-Nucleus Collisions (NN 97), Gatlinburg, TN, 2-6 Jun 1997.
- [43] M. Aggarwal *et al.*, *Directed flow in 158-A/GeV Pb-208 + Pb-208 collisions*, e-print: nucl-ex/9807004, submitted to Physical Review Letters.
- [44] G. Bertsch and S. D. Gupta, *A guide to microscopic models for intermediate energy heavy ion collisions*, Phys. Rev. **160**, 189 (1988).

- [45] J. Aichelin, '*Quantum*' molecular dynamics: A dynamical microscopic  $n$  body approach to investigate fragment formation and the nuclear equation of state in heavy ion collisions, *Phys. Rev.* **202**, 233 (1991).
- [46] Y. Pang, T. Schlagel, and S. Kahana, *Cascade for relativistic nucleus collisions*, *Physical Review Letters* **68**, 2743 (1992).
- [47] B. Blaettel, V. Koch, and U. Mosel, *Transport theoretical analysis of relativistic heavy ion collisions*, *Reports on Progress in Physics* **56**, 1 (1993).
- [48] B.-A. Li and C. Ko, *Excitation functions of stopping power and flow in relativistic heavy-ion collisions*, *Nuclear Physics A* **630**, 556 (1998), presented at 6th International Conference on Nucleus-Nucleus Collisions (NN 97), Gatlinburg, TN, 2-6 Jun 1997.
- [49] B.-A. Li and C. Ko, *Probing the softest region of nuclear equation of state*, *Physical Review C* **58**, 1382R (1998).
- [50] H. Sorge *et al.*, *Energy density, stopping and flow in 10-A/GeV - 20-A/GeV heavy ion collisions*, *Physics Letters B* **243**, 7 (1990).
- [51] H. Sorge, *How soft is baryon-dense matter?*, in proceedings of 3rd Conference on Heavy Ion Physics at the AGS (HIPAGS 96), Detroit, MI, 22-24 Aug 1996, edited by C. Pruneau *et al.* (Wayne State University, 1996), pp. 184-192.
- [52] W. Schmidt *et al.*, *Viscosity and the equation of state in high energy heavy-ion reactions*, *Physical Review C* **47**, 2782 (1993).
- [53] D. H. Rischke, S. Bernard, and J. A. Maruhn, *Relativistic hydrodynamics for heavy ion collisions. 1. General aspects and expansion into vacuum*, *Nuclear Physics A* **595**, 346 (1995).

- [54] D. H. Rischke, Y. Pursun, and J. A. Maruhn, *Relativistic hydrodynamics for heavy ion collisions. 2. Compression of nuclear matter and the phase transition to the quark - gluon plasma*, Nuclear Physics A **595**, 383 (1995), erratum-ibid. **A596**, 717 (1996).
- [55] J. Molitoris *et al.*, *Intranuclear cascade models lack dynamic flow*. Physical Review C **33**, 867 (1986).
- [56] K. Doss *et al.*, *Fragment flow in nuclear collisions*, Physical Review Letters **59**, 2720 (1987).
- [57] P. Braun-Munzinger and J. Stachel, *Dynamics of ultrarelativistic nuclear collisions with heavy beams: An experimental overview*, Nuclear Physics A **638**, 3 (1998), presented at 13th International Conference on Ultrarelativistic Nucleus-Nucleus Collisions (Quark Matter 97), Tsukuba, Japan, 1-5 Dec 1997.
- [58] J. M. Zhang, S. D. Gupta, and C. Gale, *Momentum dependent nuclear mean fields and collective flow in heavy ion collisions*, Physical Review C **50**, 1617 (1994).
- [59] P. Crochet *et al.*, *Azimuthal anisotropies as stringent test for nuclear transport models*, Nuclear Physics A **627**, 522 (1997).
- [60] S. A. Voloshin, *Transverse radial expansion and directed flow*, Physical Review C **55**, 1630 (1997).
- [61] D. H. Rischke, *Hydrodynamics and collective behavior in relativistic nuclear collisions*, Nuclear Physics A **610**, 88 (1996).
- [62] J. C. Kintner *et al.*, *Pion flow and antiflow in 1.15A GeV Au+Au*, Physical Review Letters **78**, 4165 (1997).

- [63] G. Li, C. Ko, and B.-A. Li, *Kaon flow as a probe of the kaon potential in nuclear medium*, Physical Review Letters **74**, 235 (1995).
- [64] M. Justice *et al.*, *Observation of collective effects in Lambda production at 2-GeV/nucleon*, Nuclear Physics A **590**, 549 (1995), contributed to 11th International Conference on Ultra-Relativistic Nucleus-Nucleus Collisions (Quark Matter 95), Monterey, CA, 9-13 Jan 1995.
- [65] M. Justice *et al.*, *Lambda flow in 2A-GeV Ni + Cu collisions*, e-print: nucl-ex/9708005, submitted to Physics Letters B.
- [66] J.L. Ritman *et al.*, *On the transverse momentum distribution of strange hadrons produced in relativistic heavy ion collisions*, Zeitschrift Für Physik A **352**, 355 (1995).
- [67] Y. Qi, *Lambda production in Au+Au collisions at 11.5 A·GeV/c*, Ph.D. thesis, McGill University, in preparation.
- [68] K. Filimonov, *Anisotropic azimuthal distributions of identified particles in Au+Au collisions at 11.5 A·GeV/c*, in proceedings of UIC Summer Workshop on Particle Distributions in Hadronic and Nuclear Collisions, Chicago, IL, 11-13 June 1998, (World Scientific, Singapore, 1998).
- [69] A. Jahns *et al.*, *'Antiflow' of anti-protons in heavy ion collisions*, Physical Review Letters **72**, 3464 (1994).
- [70] Y. Dai, *Directed flow in Au+Au collisions at 11.5 A·GeV/c*, Ph.D. thesis, McGill University, 1998.
- [71] H. H. Gutbrod *et al.*, *Squeezeout of nuclear matter as a function of projectile energy and mass*, Physical Review C **42**, 640 (1990).

- [72] M. Demoulin *et al.*, *Measurement of a baryon azimuthal emission pattern in Ne + (NaF, Nb, Pb) collisions at 800-MeV per nucleon*, Physics Letters B **241**, 476 (1990).
- [73] H. Gutbrod *et al.*, *A new component of the collective flow in relativistic heavy ion collisions*, Physics Letters B **216**, 267 (1989).
- [74] J.-Y. Ollitrault, *Anisotropy as a signature of transverse collective flow*, Physical Review D **46**, 229 (1992).
- [75] J.-Y. Ollitrault, *Determination of the reaction plane in ultrarelativistic nuclear collisions*, Physical Review D **48**, 1132 (1993).
- [76] S. Nishimura *et al.*, *Collective flow in 158 A GeV Pb+Pb collisions*, Nuclear Physics A **638**, 459 (1998), presented at 13th International Conference on Ultrarelativistic Nucleus-Nucleus Collisions (Quark Matter 97), Tsukuba, Japan, 1-5 Dec 1997.
- [77] D. Lambrecht *et al.*, *Energy dependence of collective flow of neutrons and protons in Au-197 + Au-197 collisions*, Zeitschrift Für Physik A **350**, 115 (1994).
- [78] D. Brill *et al.*, *Study of the out of plane emission of protons and light fragments in symmetric heavy ion collisions*, Zeitschrift Für Physik A **355**, 61 (1996).
- [79] H. Sorge, *Elliptical flow: A signature for early pressure in ultrarelativistic nucleus-nucleus collisions*, Physical Review Letters **78**, 2309 (1997).
- [80] P. Danielewicz *et al.*, *Disappearance of elliptic flow: A new probe for the nuclear equation of state*, Physical Review Letters **81**, 2438 (1998).
- [81] D. Brill *et al.*, *Azimuthally anisotropic emission of pions in symmetric heavy ion collisions*, Physical Review Letters **71**, 336 (1993).

- [82] Y. Shin *et al.*, *Enhanced out-of-plane emission of  $K^+$  mesons observed in Au + Au collisions at 1-A/GeV*, Physical Review Letters **81**, 1576 (1998).
- [83] G. Li and C. Ko, *Kaon azimuthal distributions in heavy ion collisions*, Physics Letters B **381**, 17 (1996).
- [84] R. Lacasse *et al.*, *A time-of-flight hodoscope for the E877 spectrometer*, Nuclear Instruments and Methods in Physics Research A **408**, 408 (1998).
- [85] L. S. Waters, *Energy flow in relativistic heavy ion collision at AGS experiment 814*, Ph.D. thesis, SUNY, Stony Brook, 1990.
- [86] Z. Zhang *et al.*, *Response matrix approach to the analysis of calorimetry data*, Nuclear Instruments and Methods in Physics Research A **343**, 610 (1994).
- [87] J. E. Simon-Gillo, *The construction, testing and performance of a Pb/scintillator calorimeter with fiber optic readout built for relativistic heavy ion studies*, Ph.D. thesis, Texas A&M University, 1991.
- [88] W. J. Llope, *The dissociation of relativistic nuclei*, Ph.D. thesis, SUNY, Stony Brook, 1992.
- [89] S. Greene *et al.*, *A high resolution tracking system for the investigation of relativistic heavy ion collisions*, Nuclear Physics A **525**, 609 (1991).
- [90] B. Hong, *Kaon production near zero transverse momentum in relativistic heavy ion collisions*, Ph.D. thesis, SUNY, Stony Brook, 1995.
- [91] R. Lacasse, *Hadron production in 10.8 A-GeV/c Au+Au collisions*, Ph.D. thesis, McGill University, 1998.

- [92] R. Bersch, *Design, implementation, and results from a position sensitive multi-wire proportional chamber with pad readout*, M.Sc. thesis, SUNY, Stony Brook, 1995.
- [93] W.-C. Chang, *The azimuthally anisotropic flow of transverse energy and identified protons and charged pions in 10.8 A·GeV/c Au+Au collisions at AGS*. Ph.D. thesis, SUNY, Stony Brook, 1997.
- [94] T. Vongpaseuth, *Two particle Bose-Einstein correlations in Au+Au collisions at 11.5 GeV/c per nucleon*, Ph.D. thesis, SUNY, Stony Brook, 1998.
- [95] J. Barrette *et al.*, *Centrality dependence of longitudinal and transverse baryon distributions in ultrarelativistic nuclear collisions*, *Physical Review C* **50**, 3047 (1994).
- [96] D. Miskowiec, *Momentum resolution of the E877 spectrometer - calculation*, 1996, E877 note.
- [97] J.-Y. Ollitrault, *Reconstructing azimuthal distributions in nucleus-nucleus collisions*, e-print nucl-ex/9711003.
- [98] M. Pollack, *Transverse momentum distributions and azimuthally anisotropic flow of protons, charged pions and kaons from Au+Au collisions at 11.5 A·GeV/c*, Ph.D. thesis, SUNY, Stony Brook, 1997.
- [99] S. Johnson, *Light fragment formation in 11.5 GeV per nucleon Au+Au collisions*, Ph.D. thesis, SUNY, Stony Brook, 1997.
- [100] R. Mattiello *et al.*, *Deuteron flow in ultrarelativistic heavy ion reactions*, *Physical Review Letters* **74**, 2180 (1995).

- [101] R. Mattiello, H. Sorge, H. Stoecker, and W. Greiner, *Nuclear clusters as a probe for expansion flow in heavy ion reactions at 10-A/GeV - 15-A/GeV*, Physical Review C **55**, 1443 (1997).
- [102] S. Wang *et al.*, *In-plane retardation of collective expansion in Au+Au collisions*, Physical Review Letters **76**, 3911 (1996).
- [103] D. Miskowiec, *Separation between sources of pions and protons in central Au + Au collisions at the AGS (E877)*, in proceedings of *2nd Catania Relativistic Ion Studies: Measuring the Size of Things in the Universe: HBT Interferometry and Heavy Ion Physics (CRIS 98)*, Acicastello, Italy, June 8-12, 1998, (World Scientific, Singapore, 1998), e-print Archive: nucl-ex/9808003.
- [104] L. Venema *et al.*, *Azimuthal asymmetry of neutral pion emission in Au + Au reactions at 1-GeV/nucleon*, Physical Review Letters **71**, 835 (1993).
- [105] D. Brill *et al.*, *Studies of the out-of-plane emission of pions in symmetric heavy ion collisions*, Zeitschrift Für Physik A **357**, 207 (1997).
- [106] B. Li, *Nuclear shadowing effect in relativistic heavy ion collisions*, Nuclear Physics A **570**, 797 (1994).
- [107] S. Bass, C. Hartnack, H. Stoecker, and W. Greiner, *Azimuthal correlations of pions in relativistic heavy ion collisions at 1-GeV/nucleon*, Physical Review C **51**, 3343 (1995).
- [108] S. Bass, C. Hartnack, H. Stoecker, and W. Greiner, *Out-of-plane pion emission in relativistic heavy-ion collisions: Spectroscopy of Delta resonance matter*, Physical Review Letters **71**, 1144 (1993).

- [109] S. Voloshin, R. Lednicky, S. Panitkin, and N. Xu, *Relative space-time asymmetries in pion and nucleon production in noncentral nucleus-nucleus collisions at high-energies*, Physical Review Letters **79**, 4766 (1997).
- [110] B.-A. Li and C. Ko, *Kaon dispersion relation and flow in relativistic heavy ion collisions*, Physical Review C **54**, 3283 (1996).
- [111] B.-A. Li and C. Ko, *Anti-kaon flow in heavy ion collisions: Effects of absorption and mean field potential*, Physical Review C **54**, 2159 (1996).